University of Warsaw
Faculty of Physics

Aleksandra Anna Ciemny

Exotic decay modes of medium-mass proton drip-line nuclei

Dissertation for the degree of Doctor of Philosophy

Doctoral advisor: dr hab. Chiara Mazzocchi, prof. ucz.

Warsaw, July 2023

Contents

Abstract

The high energy available in the β^+/EC decay of nuclei lying far to the left of the stability path leads to the population of highly excited states in the daughter nuclei. This, combined with decreasing charged-particle separation energies in the daughter nuclei, opens windows for a variety of decay modes with β-delayed (multi-) particle emission. The study of these decay channels provides a unique tool for gaining insight and understanding the nuclear structure of (multi-) particle unbound states, given their competitiveness against de-excitation via gamma radiation. Moreover, decay data of these nuclei provide input for the astrophysical rp-process modeling and thus understanding the abundance of elements in the Universe.

The measurements forming the basis of this thesis were conducted during two experimental campaigns aiming at investigating exotic phenomena in the structure of medium-mass nuclei in the vicinity of the proton drip line. Neutron-deficient silicon isotopes were produced and investigated at the Cyclotron Institute at Texas A&M University, while neutron-deficient germanium and zinc isotopes were produced and studied at the National Superconducting Cyclotron Laboratory at Michigan State University. In each of these experiments, the ions of interest were produced in the fragmentation reaction of a heavier projectile and electromagnetically separated from the other reaction products and from the primary beam. They were then implanted into and their decays were studied by means of the optical time projection chamber (OTPC) detector. Within this work the complete analysis of the data collected was performed, from Monte Carlo simulations to reconstruction of the momenta of decay products and interpretation of the results in the context of literature, when available, and theoretical modeling.

Among the results of the first experiment are the confirmation of the previously known β-delayed one and two-proton emission (βp and β2p) from ^{22}Si and ^{23}Si. Moreover, two new decay modes were observed in ^{23}Si: β-delayed 3p- and pα emission. The branching ratios for the two latter are discussed in the context of the properties of other known emitters of these exotic decay channels with T_z from $-3/2$ to $-7/2$. In the second experiment, the new isotope ^{59}Ge was observed for the first time. Its production rate, as well as the production rates of less exotic germanium isotopes ($^{60-62}$Ge), yielded cross-section values that are discussed in the context of previously measured values. The limited prediction capabilities of models when looking at the production of nuclei so far from stability make in fact the measurement of production cross-sections of vital importance for planning future experiments. The β decay of ^{60}Ge was measured for the first time and found to proceed via βp emission with a branching ratio of $\approx$100%. The β-delayed proton emission channel of ^{58}Zn was also observed for the first time and the energy spectrum of the detected protons allowed to investigate the B(GT) distribution above the proton-separation energy in the daughter nucleus ^{58}Cu. Despite the small branching ratio, the Gamow-Teller strength for the main observed proton group was comparable in intensity to the values known for proton-bound states, emphasizing the importance of taking into account the channels involving the emission of the particles while investigating the B(GT) distribution. The obtained distribution is discussed in the framework of QRPA calculations. The impact of the obtained branching ratio on the rp-process and in particular on the abundance of A = 57 nuclei was investigated, yet found to be of the order of a few percent.

Streszczenie (Abstract in Polish)

Wysokie energie dostępne w rozpadzie β^+/EC jąder leżących daleko na lewo od ścieżki stabilności prowadzą do populowania wysoko wzbudzonych stanów w jądrach-córkach. W połączeniu ze zmniejszającymi się energiami separacji naładowanych cząstek w jądrach-córkach, umożliwia to występowanie rozmaitych kanałów rozpadu z emisją (wielu) cząstek opóźnionych po rozpadzie β. Badanie tych kanałów jest niezbędne do zrozumienia struktury jądrowej stanów niezwiązanych ze względu na emisję (wielu) cząstek, jako że im dalej od ścieżki stabilności, tym mocniej kanały te wygrywają z deekscytacją przez emisję promieniowania γ. Co więcej, badania dotyczące rozpadów tych jąder dostarczają danych potrzebnych do modelowania astrofizycznego procesu rp, a tym samym występowania pierwiastków we Wszechświecie.

Pomiary będące podstawą niniejszej pracy przeprowadzono podczas dwóch eksperymentów. Ich celem było zbadanie egzotycznych zjawisk w leżących w pobliżu linii odpadania protonu średnio masywnych jądrach. Neutrono-deficytowe izotopy krzemu zostały wyprodukowane i zbadane w Cyclotron Institute, Texas A&M University, podczas gdy neutrono-deficytowe izotopy germanu i cynku zostały wyprodukowane i zbadane w National Superconducting Cyclotron Laboratory, Michigan State University. W każdym z tych eksperymentów jony będące przedmiotem badań były wytwarzane w reakcji fragmentacji cięższego pocisku i elektromagnetycznie oddzielane od innych produktów reakcji i od wiązki pierwotnej. Następnie implantowano je i badano ich rozpady za pomocą komory dryfowej z projekcją czasu i odczytem optycznym (*optical time projection chamber*, OTPC). W ramach niniejszej pracy przeprowadzono pełną analizę zebranych danych, począwszy od symulacji Monte Carlo, po rekonstrukcję pędów produktów rozpadu i interpretację wyników w kontekście dostępnych danych eksperymentalnych oraz wyników teoretycznych.

Wśród wyników pierwszego eksperymentu znajduje się potwierdzenie obserwowanej wcześniej emisji jednego i dwóch protonów opóźnionych po rozpadzie β (βp i β2p) z ^{22}Si i ^{23}Si. Ponadto w ^{23}Si zaobserwowano dwa nowe kanały rozpadu: emisję 3p i pα opóźnionych po rozpadzie β. Stosunki rozgałęzień dla dwóch ostatnich omówiono w kontekście właściwości innych znanych emiterów o rzucie izospinu T_z od $-3/2$ do $-7/2$. W drugim eksperymencie po raz pierwszy zaobserwowano nowy izotop ^{59}Ge. Obliczone dla niego, oraz dla mniej egzotycznych izotopów germanu ($^{60-62}$Ge), przekroje czynne na produkcję zostały omówione w kontekście wcześniej zmierzonych wartości. Ograniczona zdolność predykcyjna modeli w zakresie przewidywania produkcji jąder tak dalekich od stabilności sprawia, że pomiary przekrojów czynnych mają kluczowe znaczenie dla planowania przyszłych eksperymentów. Rozpad β ^{60}Ge został zmierzony po raz pierwszy i stwierdzono, że zachodzi poprzez emisję βp z prawdopodobieństwem $\approx 100\%$. Ten sam kanał rozpadu został zaobserwowany po raz pierwszy również w ^{58}Zn, a widmo energetyczne wykrytych protonów pozwoliło zbadać rozkład B(GT) powyżej energii separacji protonu w jądrze-córce, ^{58}Cu. Pomimo małego współczynnika rozgałęzienia siła przejść Gamowa-Tellera dla głównej zaobserwowanej grupy protonów była porównywalna pod względem intensywności do wartości znanych dla stanów protonowo-związanych, co podkreśla znaczenie uwzględnienia kanałów z emisją cząstek podczas badania rozkładu B(GT). Otrzymany rozkład porównano z wynikami obliczeń QRPA. Zbadano wpływ uzyskanego stosunku rozgałęzień na proces rp, a w szczególności na występowanie jąder z A = 57, jednak stwierdzono, że nie przekracza on kilku procent.

Acknowledgements

The first huge thank you goes to Chiara, who has supported me throughout my entire academic career, from the second year of my studies until now. Not only did she take me to my first experiment in the summer of 2012 (I still remember telling her, "I can't believe it is happening!"), but she also taught me how to make tiramisu and always remembered to apply "Ola's correction" to all my enthusiastic plans to ensure I could fit everything into the 24 hours of a day. I am really glad to have had you as my supervisor!

To Prof. Dominik, who once came to the student lab and told me to follow him because he had something more interesting to show me - that's how it all started. To Prof. Janas, for providing patient and accessible answers to all my questions during the experiments, so that I never had to hesitate to ask him. To Prof. Pfützner, who not only led our group, but was also a great travel companion when we got stuck in Shanghai. We managed to visit all the most important places, even in just one extra day. And to Agnieszka, who was the first person to hire me as a student to analyze the gamma spectra, giving me the impression that I could "really" contribute to physics.

To colleagues who accompanied me during experiments, shifts, and visits to different places, and engaged in nightly discussions - especially to Magda and Marcin, with whom I went to my first experiments and thanks to whom I had the first IPA in my life. I am grateful to you to this day! To all the other people I met, not only in the Nuclear Physics Division but in all the places I had the chance to visit since I started my studies until now, thank you for giving me so many great memories. And in particular, to Natalia - the person with whom I have experienced the most varied adventures during these last years. She is the one who listened to most of my complaints while I was writing this thesis, and she still talks to me. Thank you! Without you, it wouldn't have been such fun.

Thanks also to my parents for encouraging my interest in math and physics since I was three, for never pushing too much, and always supporting my educational choices. And to my parents-in-law, for standing by me in all aspects of life since we met, and for enthusiastically celebrating all my scientific achievements. Additionally, to my grandfather for being the person who most frequently asked the "what about your Ph.D?" question.

Finally, I would like to thank my favorite flatmate (and husband), M.C., whom I met just before the first lectures at the University, at the very beginning of our studies, and who has been in my life ever since. Thank you for skipping lectures together to go for pizza, studying for exams throughout the night, getting excited about algebra, and engaging in countless conversations about physics, life, the universe, and everything. And to my two wonderful daughters, Agnieszka and Małgorzata - without you, this adventure would probably be shorter, but it would certainly be less joyful and satisfying. Keep asking questions and seeking fair answers!

Chapter 1

Introduction

1.1 Physical processes at the edge of stability

Our universe is composed almost exclusively by less than 300 isotopes of around 100 elements. These are the stable, or very long-lived, combinations of protons and neutrons held together by strong nuclear forces. The number of all known nuclei is over 10 times higher and it grows each year thanks to the development of new cutting-edge laboratories. The development of new experimental methods, such as radioactive beams, led to an even more rapid progress in this field over the last 30-50 years. Only in the last decade, between 2012 and 2021, 226 new nuclides were discovered [1].

1.1.1 β-stability valley and β decay

For a given mass number A, there is a combination (or combinations) of protons and neutrons that is characterized by a maximum binding energy. The isotopes corresponding to such combination are, with very few exceptions, stable against β decay and constitute the β-stability path or valley on the chart of nuclei. In Figure 1.1 the chart of nuclei showing all known[1] isotopes is shown, with the β-stability valley marked by black squares. All isotopes outside this path will decay spontaneously back towards stability mostly by α and β decay, but also by more rare processes such as one- and two-proton radioactivity. This work will focus on the study of rare decay modes at the proton-rich edge of the chart of nuclei.

The binding energy for isobars of given mass A as a function of the atomic number Z has a parabolic shape and is described by the Bethe-Weizsäcker semi-empirical mass formula based on liquid-drop model of a nucleus:

$$B(Z,A) = a_V A - a_S A^{2/3} - a_C \frac{Z(Z-1)}{A^{1/3}} - a_A \frac{(A-2z)^2}{A} + \delta(A,Z) \tag{1.1}$$

with a_V – coefficient for the volume term, a_S – coefficient for the surface term, a_C – coefficient for Coulomb term and a_A – coefficient for the asymmetry term, while $\delta(A,Z)$ stands for the pairing interaction and is $= +/-\delta_0$ for even Z and A / odd Z and A, and $= 0$ for odd A. The binding energy has therefore larger value close to the stability path. Figure 1.2 shows the binding energy per nucleon for A=58 with two stable isobars present: ^{58}Ni and ^{58}Fe. Nuclei that are on the right scope of the parabola (proton-rich nuclei) will change their configuration by transforming protons into neutrons in order to increase the binding energy. They will undergo β^+ and/or electron capture (EC) process. In the nuclei on the left scope of the parabola (neutron-rich) the opposite transformation will take place: neutrons into protons via β^- decay. By defining the mass of a nuclide $^A Z$ as the sum of Z hydrogen atom masses and N neutron masses, decreased by the binding energy, one obtains for a given A the mass parabola known from nuclear physics textbooks [3].

[1] cut-off date 01.12.2022

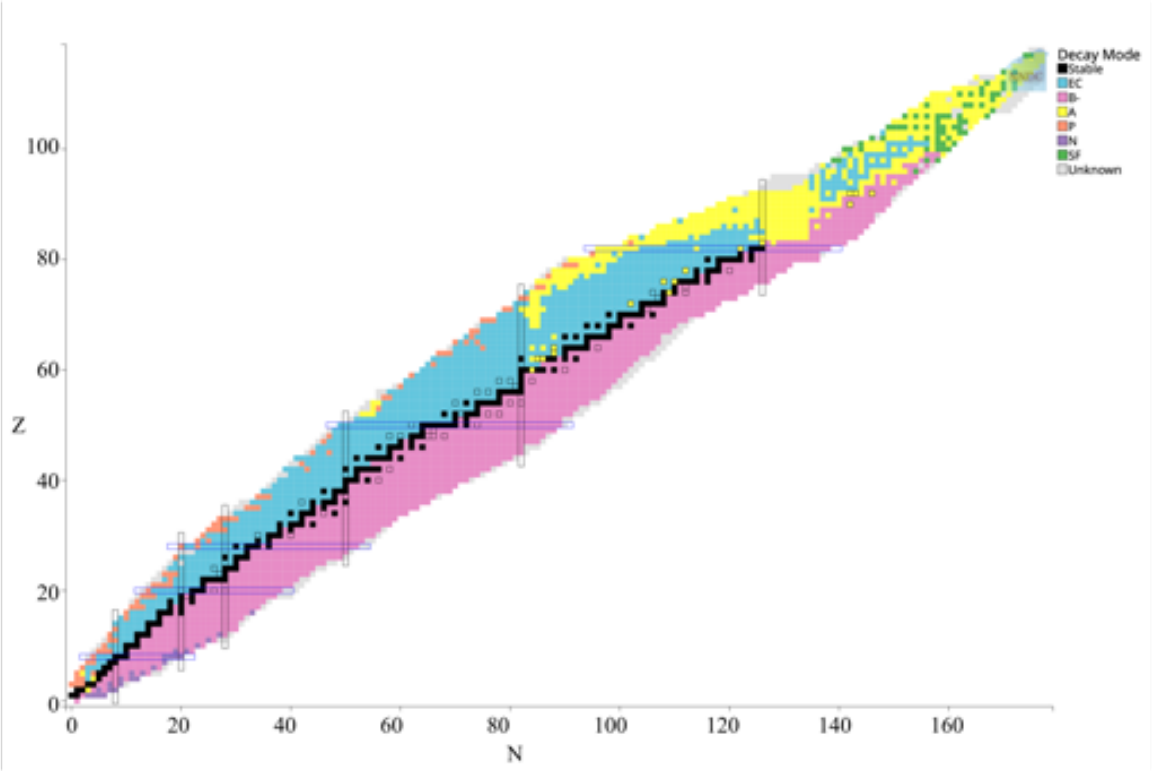

Figure 1.1: Nuclide chart showing decay modes of all isotopes known to date[1]. Stable nuclei are marked in black. Nuclei undergoing β^+/electron capture (EC) and β^- process (β^-) are marked in blue and pink, respectively, those undergoing α and proton decays and fission are highlighted in yellow, orange and green, respectively. Picture from Ref. [2].

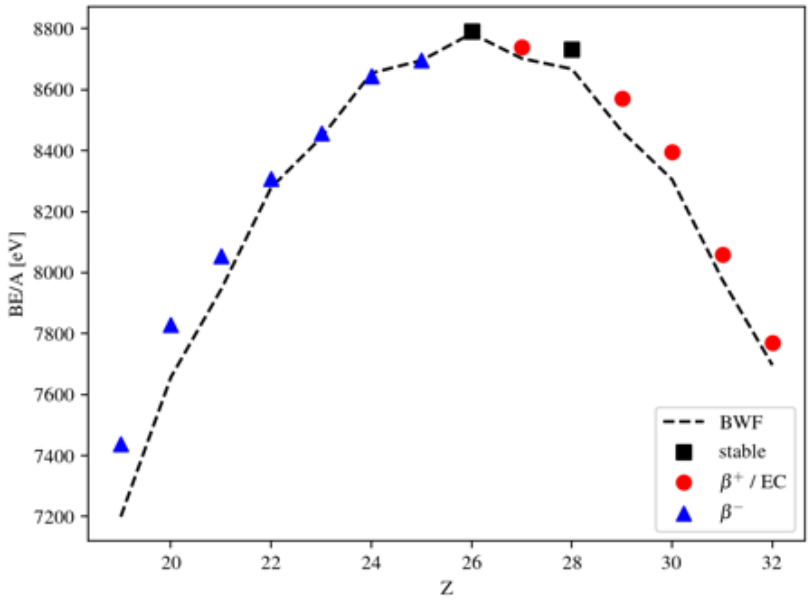

Figure 1.2: Binding energy per nucleon (BE/A) as function of Z for isobars with A=58. Stable nuclei are marked with black squares. Nuclei undergoing β^+/EC and β^- processes are marked with red circles and blue triangles, respectively. All values are taken from Ref. [4]. The dashed black line shows the corresponding values obtained with equation 1.1 using coefficients from Ref. [5].

β decays, which are weak interaction processes, can be described schematically as follows. In β^+ decay, a nucleus ${}^{A}Z$ changes into a nucleus ${}^{A}(Z-1)$, a positron and an electron neutrino:

$$ {}^{A}Z \rightarrow {}^{A}(Z-1) + e^{+} + \nu_e, \tag{1.2}$$

while in the electron-capture process (EC), a nucleus ${}^{A}Z$ captures one of the bound electrons and changes into nucleus ${}^{A}(Z-1)$ and an electron neutrino.

$$ {}^{A}Z + e_b^{-} \rightarrow {}^{A}(Z-1) + \nu_e \tag{1.3}$$

In β^- decay, a nucleus ${}^{A}Z$ changes into a nucleus ${}^{A}(Z+1)$, an electron and an electron anti-neutrino:

$$ {}^{A}Z \rightarrow {}^{A}(Z+1) + e^{-} + \overline{\nu_e} \tag{1.4}$$

β decay itself is possible if the energy available for this process, or Q-value, is positive, i.e. the daughter nucleus is more bound than the mother. Q-value for EC is therefore

$$ Q_{EC} = M(A,Z)c^2 - M(A,Z-1)c^2 \tag{1.5}$$

where M(A, Z) and M(A, Z-1) are the masses of the atoms ^{A}Z and ^{A}(Z-1), respectively. The energy available to be released in β^+ process is equal to

$$ Q_{\beta^+} = M(A,Z)c^2 - M(A,Z-1)c^2 - 2m_e c^2 = Q_{EC} - 2m_e c^2 \tag{1.6}$$

where M(A, Z) and M(A, Z-1) are the masses of atoms of ^{A}Z and ^{A}(Z-1) isotopes, respectively, and m_e is an electron mass. Neutrino masses are neglected in both expressions. $Q_{\beta+}$ values for nuclei up to Z=45 are shown in Figure 1.3.

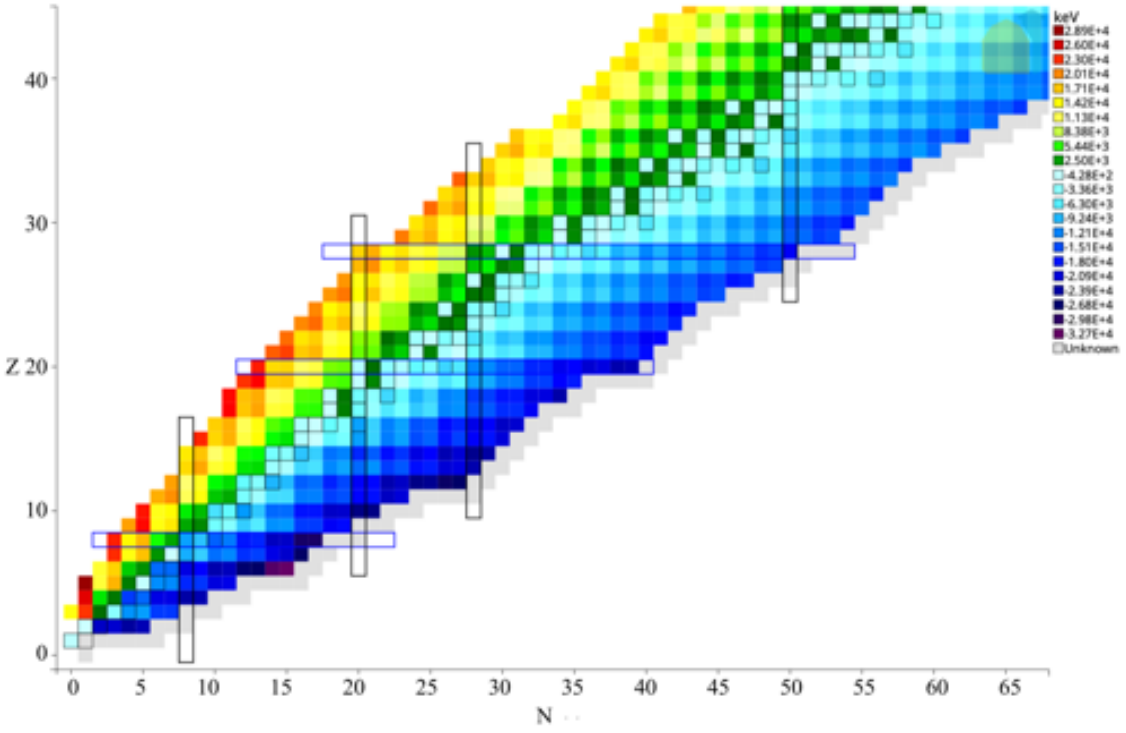

Figure 1.3: Q_{EC} energies for all isotopes up to Z = 45 [2]. The values are positive/negative on the left/right side of the stability path.

The energy available in β^- decay is

$$Q_{\beta^-} = M(A,Z)c^2 - M(A,Z+1)c^2 \tag{1.7}$$

where M(A, Z) and M(A, Z+1) are masses of atoms of ${}^{A}Z$ and ${}^{A}(Z+1)$ isotopes, respectively.

The proton separation energy is the minimum energy that is needed for a proton to be removed from the nucleus. It is defined as

$$S_p = M(A-1,Z-1)c^2 + M_H c^2 - M(A,Z)c^2 = B(A,Z) - B(A-1,Z-1) \tag{1.8}$$

where M(A, Z) and M(A-1, Z-1) are masses of the atoms of the ${}^{A}Z$ and ${}^{A-1}(Z-1)$ isotopes, respectively, and M_H is the hydrogen atom mass. It might also be expressed as the difference between the binding energies of these two nuclides (B(A, Z) and B(A-1, Z-1)). Separation energies of x protons (S_{xp}) can be obtained by changing in the above equation M(A-1, Z-1) to M(A-x, Z-x), and M_H to $x \cdot M_H$. Separation energies of other particles can be defined analogously.

For extremely proton-rich nuclei S_p can become negative and spontaneous proton emission becomes possible. The boundary beyond which this process takes place is called a proton drip line. The Figure 1.4 shows the S_p values throughout the nuclide chart up to Z = 45 and the proton drip line.

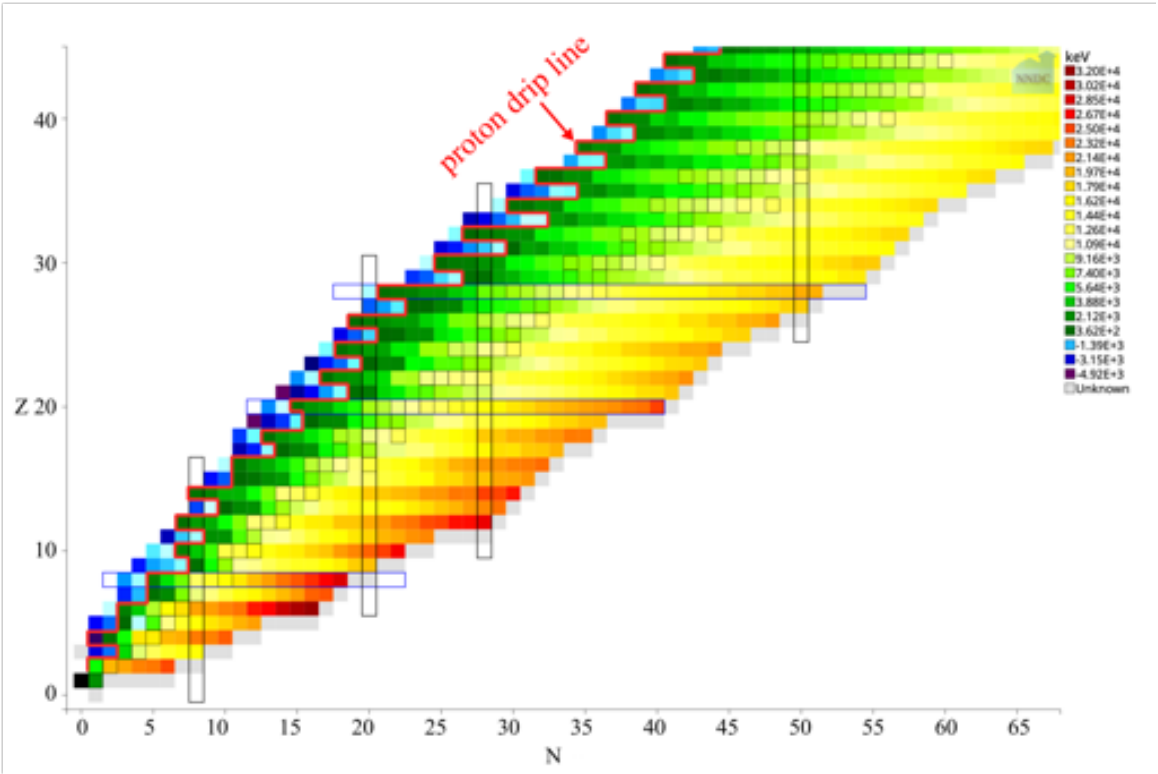

Figure 1.4: Proton separation energy for all isotopes up to Z = 45 [2]. The proton drip line is marked in red. For isotopes of even Z elements it is placed further away from the stability path than for odd Z values due to the effect of pairing forces .

1.1.2 β transitions and β strength

The intensity of a β transition can be given in terms of the reduced transition probability, the so called ft-value, where t is the partial half-life of the state and f is the phase-space factor, i.e. a dimensionless integral over the spectrum of the β particles, depending on the leptons kinematics and the Z of the daughter nucleus:

$$ft = \frac{C}{B_F + \frac{g_A^2}{g_V^2} B_{GT}} \tag{1.9}$$

B_F and B_{GT} are reduced matrix elements squared of the Fermi- (F) and Gamow-Teller (GT) interaction, into which the nuclear transition between initial and final state can be decomposed:

$$B_F = |M_F|^2, B_{GT} = |M_{GT}|^2 \tag{1.10}$$

often referred to as the strengths of the respective interactions. g_V and g_A are vector and axial-vector coupling constants of the weak interactions, connected with F and GT part of it, respectively. Constant C

$$C = \frac{2\pi^3 \hbar^7 \ln 2}{m_e^5 c^4 g_V^2} \tag{1.11}$$

and g_A/g_V can be calculated by fitting to the experimental data from $0^+ \rightarrow 0^+$ superallowed β decays studies. Recent best-fit values are $C = 6144.2(16)s$ and $|g_A/g_V| = 1.2694(28)$ [6]. The ft value spanns over many orders of magnitude, hence its logarithm $\log ft = \log_{10}(ft[s])$ is usually given.

While discussing β transitions, one must keep in mind the presence of the leptons, (anti)-neutrino and (anti)electron, in the final state. Their free particles wave function can be expanded in series and if only the first term (≈ 1) of the expansion is taken into account, one refers to it as an "allowed" transition approximation. This corresponds to the situation, when the leptons in the final state carry no orbital angular momentum, and the only change of nuclear total angular momentum results from the spin of the leptons ($s = \frac{1}{2}$ each, coupling to 0 or 1). Such decays are called "allowed". In allowed Fermi decay, the total spin of the emitted leptons equals 0, which implies no change in the angular momentum $\Delta J = 0$ nor in total isospin $\Delta T = 0$. In allowed Gamow-Teller transitions, the total spin carried by leptons equals 1, leading to the possible change of angular momentum $\Delta J = 0, \pm 1$ and of total isospin $\Delta T = 0, \pm 1$. Both types of decays conserve the parity π. Pure Fermi-type decays only take place between J=0 states with no change in angular momentum nor parity, e.g. between states in the same shell model orbital. Such decays (both Fermi- and Gamow-Teller) are called allowed, while the term "superallowed" is used for $0^+ \rightarrow 0^+$ Fermi transitions. Forbidden transitions are those requiring bigger change in total angular momentum and/or parity change, and are characterised by longer lifetimes. The selection rules for several transition types, up to third forbidden, are summarised in Table 1.1.

Table 1.1: Selection rules for allowed and forbidden β decays, detailing the allowed Fermi and Gamow-Teller transitions, as well as superallowed Fermi transitions.

decay	ΔJ	ΔT	$\Delta\pi$
superallowed (F)	$0^+ \rightarrow 0^+$	0	no
allowed (F)	0	0	no
allowed (GT)	0, 1 (except $J_i = J_f = 0$)	0, 1	no
first forbidden	0, 1, 2	0, 1	yes
second forbidden	1, 2, 3	0, 1	no
third forbidden	2, 3, 4	0, 1	yes

As follows from the selection rules, $B_F \neq 0$ only for $\Delta J = \Delta T = 0$, whereas B_{GT} can be $\neq 0$ whenever angular momentum and total isospin does not change or changes by one unit (except $J_i = J_f = 0$). It can be obtained experimentally from the measured $T_{1/2}$ and the branching ratio.

The strong interaction responsible for holding the nucleons together is charge-independent, therefore, if we neglect Coulomb interactions between protons, isospin is a good quantum number for describing the nucleus. A pure Fermi transition conserves isospin, i.e. the initial and final states belong to the same isospin multiplet. The state in the daughter nucleus populated by Fermi decay of the

mother nucleus ground state is called Isobaric Analogue State (IAS). In reality, the charge-dependent interactions can not be neglected, with the consequence that there is a difference in masses of the initial (g. s.) and final (IAS) states. This results from the difference in Coulomb energy of the states (Coulomb displacement energy, ΔE_C) and the difference between proton and neutron mass. ΔE_C can be expressed as

$$\Delta E_C = M_{g.s.}(A, Z)c^2 - M_{IAS}(A, Z-1)c^2 - (M_{^1H} - m_n)c^2 \tag{1.12}$$

with mass of the "missing" electron included into the hydrogen mass [7]. Therefore, there is always a small portion of the Fermi decay that populates states other than IAS.

1.1.3 β-delayed (multi-) particle emission

β-delayed charged particle emission is a phenomenon that arises while departing from the β-stability line towards the proton drip line. It is driven by the fact that the Q_{EC} values get larger and, at the same time, particle(s) separation energies in the respective daughter nuclei become lower due to the increasing influence of the Coulomb force.

The high Q_{EC} values available near the proton drip line allow to populate excited states (including the IAS) in the daughter nucleus and, if the excitation energy E_{ex} exceeds S_p, it can lead to the prompt emission of protons following β decay, the so-called β-delayed proton emission (βp). Once energetically possible, this process becomes increasingly competitive to de-excitation via γ emission, with increasing excitation energy of the state populated. The shape of the spectrum of β-delayed particles depends on the density of the states which are populated in β decay, and from which the particles are emitted, and on the β strength distribution. If β decay feeds a region with low state density, or even mainly one excited state (e.g. IAS), and the density of states in the granddaughter/final nucleus is low, the proton spectrum consists of discrete lines. In the opposite case, it displays a broad, continuous "bump" and individual proton transitions can not be disentangled. Examples of nuclei with these two types of βp energy spectra are ^{57}Zn [8] and ^{60}Ga [9], respectively.

If E_{ex} is larger than S_{2p}, β-delayed two-proton emission (β2p) may occur. Similarly, more exotic decay modes with β-delayed (multi-) particle emission, such as $\beta 3p$, β^3He or $\beta\alpha p/\beta p\alpha$, can occur when the respective particle separation energies fall within the Q_{EC} window. In Figure 1.5 the exotic decay modes considered in this work are summarised schematically.

βp emission was first observed in 1963 from ^{25}Si and, tentatively, from several isotopes nearby [10]. 20 years later, ^{22}Al was identified as the first known β2p emitter [11]. Until recently about 200 βp emitters have been identified, among which some present also decay by β-delayed emission of multiple particles. Prior to this work, β-delayed three proton emission (β3p) had only been observed in ^{45}Fe, ^{43}Cr and ^{31}Ar. A similar situation holds for isotopes emitting β-delayed proton + α particle ($\beta\alpha$p / $\beta p\alpha$), which has been observed only in ^{9}C, ^{17}Ne and ^{21}Mg [12].

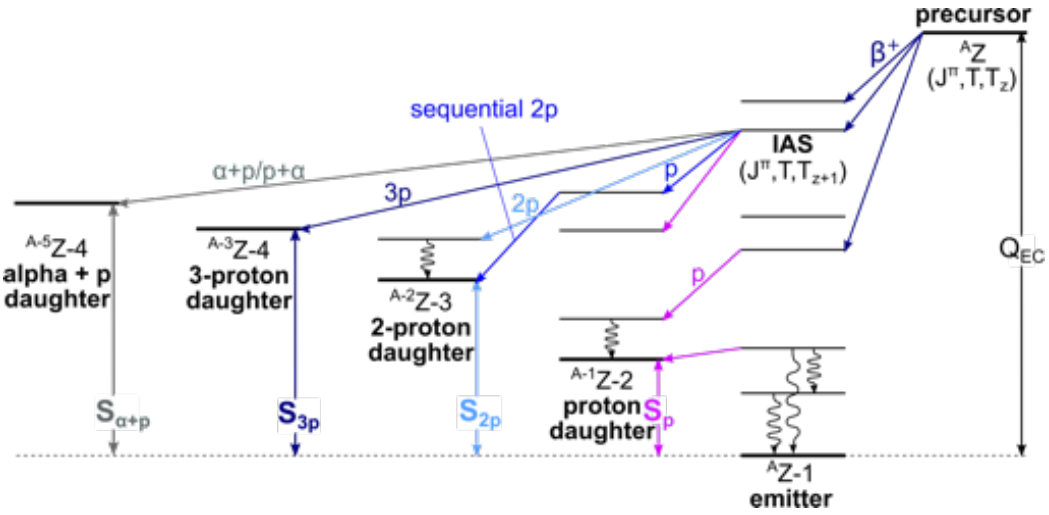

Figure 1.5: Scheme of β-delayed (multi-) charged particle emission. The mother nucleus ^{A}Z decays by β^+/EC. The Q_{EC} value available in the process is sufficiently large to allow populating highly excited, particle-unbound states in the daughter nucleus ^{A}(Z-1). Thus, particle emission from ^{A}(Z-1) occurs and ^{A}Z and ^{A}(Z-1) are the precursor and emitter, respectively. Depending on the energy available, one, two, or more protons (and other particles) can be emitted. Deexcitation via γ emission in the daughter nucleus competes with charged-particle emission from unbound states typically only at the lower energies, just above the particle-separation energy. For bound states, only γ deexcitation is possible. If the daughter nucleus is populated in an excited state, it might also de-excite via γ emission.

1.2 Exotic medium-mass proton-rich isotopes - state of the art

The investigation of exotic nuclei around and beyond the proton drip line remains one of the modern low-energy nuclear-physics frontiers. The strong imbalance between the proton and neutron numbers creates an ideal opportunity for testing nuclear forces and structure models in such exotic nuclear environments. The interplay of the low particle-separation energies, large β-decay Q-values, and the Coulomb barrier results in a variety of interesting phenomena, as described in Section 1.1, and provides the playground for studying nuclear properties, not available in nuclei closer to stability.

This section summarizes the state of knowledge on the isotopes being subject of this dissertation at the time they were investigated, namely the lightest silicon isotopes and the region around ^{59}Ge. The corresponding regions of the chart of nuclei are shown in Figure 1.6.

1.2.1 Silicon isotopes

^{22,23}Si are most neutron-deficient silicon isotopes known to date. Due to the large energy available in β^+/EC decay, they are both characterized by a variety of energetically possible rare decay modes among those discussed in Section 1.1.3, as shown in Figure 1.7.

^{22}Si

^{22}Si is the lightest silicon isotope and the lightest $T_z = -3$ nucleus observed to date. It was first identified at GANIL, Caen, France, in an experiment using the fragmentation reaction of a ^{36}Ar primary beam (85 A·MeV) on a ^{nat}Ni target [13]. 161 ions were identified directly by using a telescope consisting of two ΔE and one E silicon detectors. A decade later, its decay was investigated in the same laboratory [14,15] with an ^{36}Ar beam impinging on a Ni target at 95 A·MeV. The ions of interest were separated from the remaining reaction products by means of the LISE3 separator, identified on the basis of standard energy loss (ΔE) vs time-of-flight (ToF) measurements, and implanted in a silicon detector. β-delayed proton emission from ^{22}Si was measured for the first time and 4 proton transitions between 1.6 and 2.2 MeV, as well as one broad proton distribution around 1 MeV, were

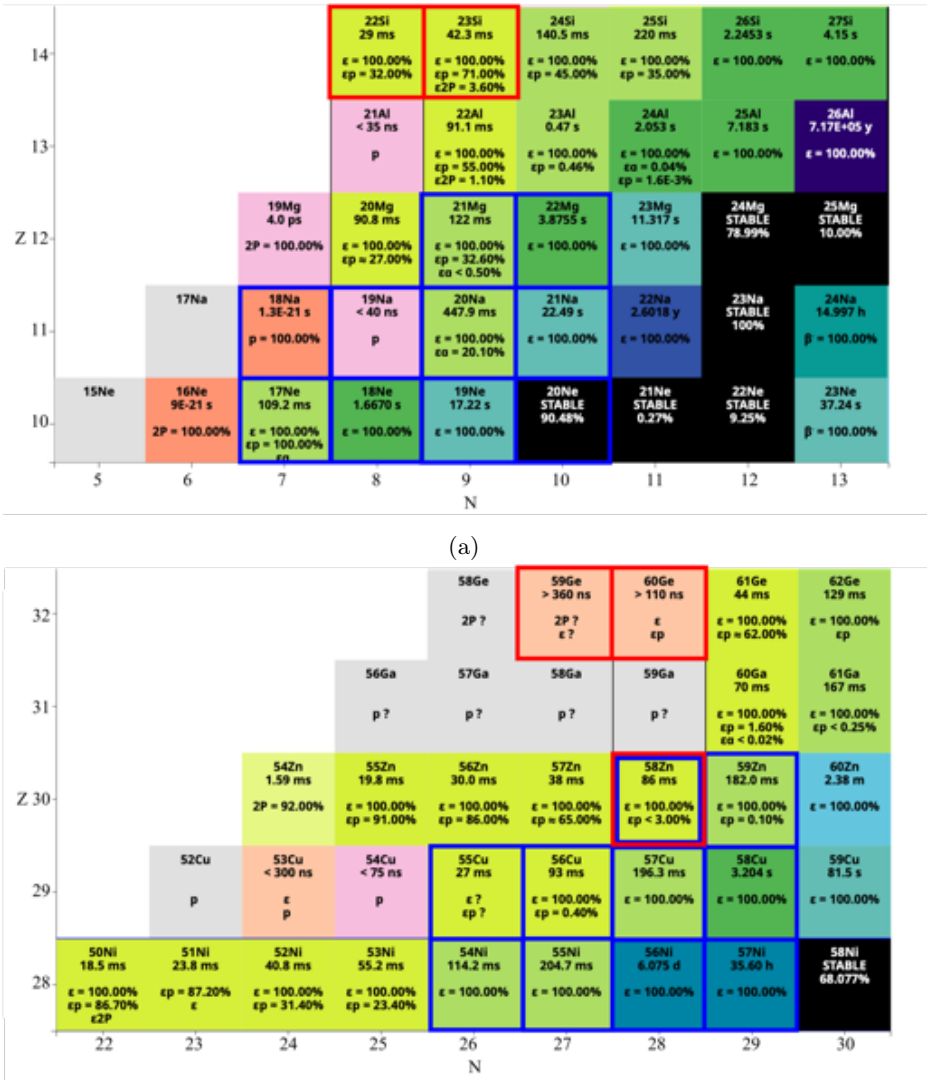

(b)

Figure 1.6: Nuclide chart fragments around (a) ^{22,23}Si and (b) ^{59,60}Ge and ^{58}Zn, showing the half-lifes and the most probable decay-modes for the ions of interest (marked with red squares) and the surrounding isotopes (source: NNDC [2]). All possible granddaughter nuclei for the open decay channels for β-delayed particle emission of the ions of interest (as listed in Sections 1.2.1 and 1.2.2) are marked with blue squares.

found. The branching ratio for βp above 500 keV was found to be around 100% and it was reported, that no protons with energy below 500 keV are present in the measured spectra. The half-life of ^{22}Si was determined to be $t_{1/2} = 29 \pm 2$ ms.

During recent studies performed at RIBLL1, Lanzhou, China, ^{22}Si ions were produced and their decay investigated with a detection system consisting of an array of silicon detectors and HPGe clovers. A new decay channel with β2p emission from the IAS in ^{22}Al was discovered [16], as well as a new, low-energy peak in the βp spectrum. The value of half-life resulting from the collected data was 27.8(35) ms. ^{22}Si was also reported to show a large mirror asymmetry compared to the mirror ^{22}O β^- decay in its decay to low-lying states, although with large uncertainties [17].

Energies of all proton transitions as determined in the previous studies are listed in Table 1.2. In this work, β-delayed charged particle emission from ^{22}Si was reinvestigated.

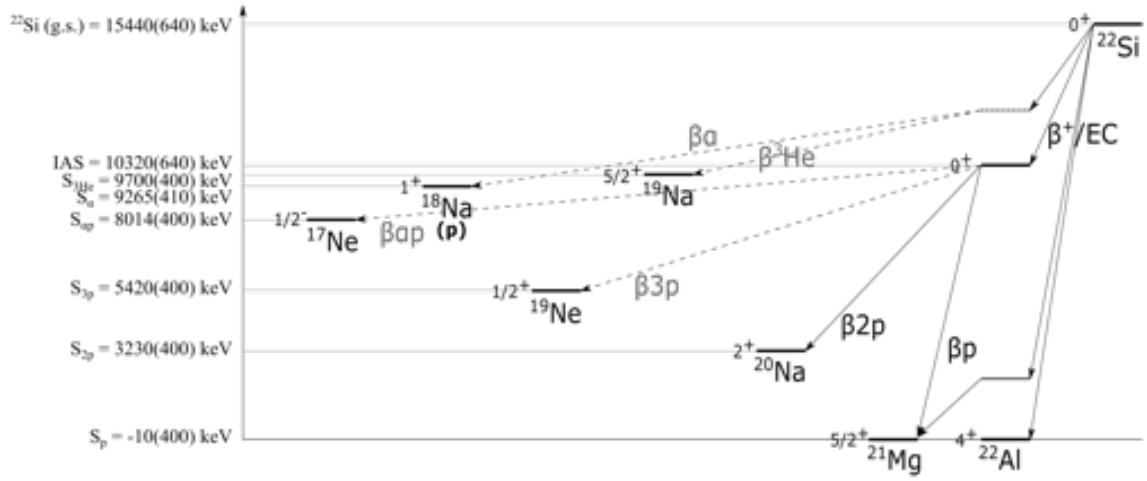

(a)

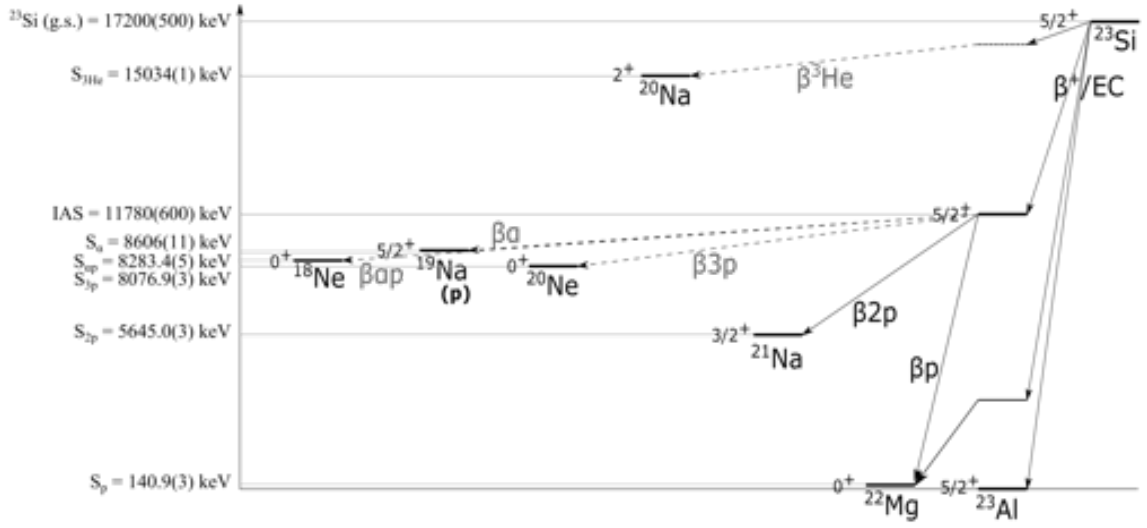

(b)

Figure 1.7: Decay schemes showing the possible decay modes of (a) ^{22}Si and (b) ^{23}Si. In each subfigure, the Q_{EC} value as well as IAS energy and separation energies in the β^+/EC-daughter nucleus are marked. Solid arrows show decay channels known prior to this work, whereas dashed lines indicate other available decay modes. Example levels beside the IAS are marked to show the possible decay through excited states. All energies are with respect to the β^+/EC-daughter ground state and stem from the most recent atomic mass evaluation (AME2020) [4].

^{23}Si

^{23}Si is the lightest $T_z = -\frac{5}{2}$ isotope discovered so far. It was first observed in 1985 at GANIL [18] as a product of the fragmentation reaction of 77 A·MeV ^{40}Ca beam on a ^{nat}Ni target. 74 ^{23}Si ions were identified among the electromagnetically separated reaction products using LISE spectrometer. Unfortunately, their spectroscopic studies were not possible at this time due to a strong contamination from the produced β-delayed proton and α emitting nuclei.

A decade later, the upgrade of the LISE spectrometer to LISE3 made it possible to perform the decay studies [15, 19]. The ions of interest were produced in the fragmentation reaction of ^{36}Ar primary beam at 95 A·MeV on a ^{nat}Ni target and separated from the rest of the fragments by means of the LISE3 separator. They were then implanted into a detection setup consisting of Micro-Strip Gas Counter (MSGC) and silicon detector. β-delayed one- and two-proton emission channels were identified for the first time. Both the low- (below 1 MeV) as well as the high-energy (up to around 12 MeV) part of the proton spectrum were measured. 14 peaks identified as βp transitions

Table 1.2: Proton transitions known in ^{22}Si decay data prior to this work. For each experiment, the proton energy E_p and branching ratio br are summarized, as well as the decay channel to which the transition was assigned.

Blank *et al.* [14]		Xu *et al.* [16,17]		Lee *et al.* [17]		
E_p [keV]	br [%]	E_p [keV]	br [%]	E_p [keV]	br [%]	decay channel
		680		710(50)	5.3(10)	βp
1000						βp
1630(50)	6(2)					βp
1990(50)	20(2)	1950(70)		1950(50)	43.0(46)	βp
2100(50)	4(2)					βp
2170(50)	2(1)			2150(50)	13.5(21)	βp
		5600(70)	0.7(3)			β2p

were detected, as well as two β2p transitions from the IAS to the ground state and to the first excited state in the 2p daughter ^{21}Na, see Table 1.3. The β^+/EC decay of ^{23}Si was found to be dominated by transitions to the IAS in ^{23}Al, thus the energy of its state was inferred, with part of the strength feeding lower-lying states in Gamow-Teller decay. The ^{23}Si half-life was determined to be $t_{1/2} = 42.3 \pm 0.4$ ms.

More recently, a new study of ^{23}Si was performed at the RIBBL1 facility [20]. A ^{28}Si beam impinged on a Be target at an energy of 76 A·MeV. An array of silicon detectors and clover-type HPGe detectors were used to detect β electrons and both protons and γ rays emitted after its β^+/EC decay. Coincidences between the signals allowed for confirmation of previously discovered β2p channel as well as adding new transitions and studying the low-energy structure of ^{23}Al. The half-life of ^{23}Si was found to be $t_{1/2} = 40.2 \pm 1.9$ ms, which is consistent with the previous value. More exotic decay modes as β3p and $\beta\alpha$p/pα were not identified, although being energetically possible, see Figure 1.7b. All identified proton transitions are listed in Table 1.3.

The low-energy structure of ^{23}Si β-decay daughter, ^{23}Al, was investigated over the years also by means of nuclear reactions [21–23] in the context of astrophysical calculations for nucleosynthesis in novae. Its lowest lying excited state has $I^\pi = (\frac{1}{2})^+$ and is therefore not easily populated/observed in β decay. It was identified in a transfer reaction study and placed at the energy of 550(20) keV [21].

In this work β-delayed charged-particle emission was reinvestigated to gain an insight into the structure of ^{23}Al and look for the most exotic decay channels.

1.2.2 Germanium and zinc isotopes

The second group of isotopes investigated within this thesis contains neutron-deficient germanium and zinc isotopes. In Table 1.4 β-decay energies of ^{59,60}Ge as well as separation energies of several particles in their daughter nuclei ^{59,60}Ga are listed.

^{59}Ge

^{59}Ge is an extremely neutron-deficient germanium isotope that had not been identified before this study, the lightest germanium isotope known prior to this research being ^{60}Ge. However, predictions existed for its properties. On the basis of nuclear masses obtained with the Skyrme Hartree-Fock model for the displacement energies, S_p and S_{2p} were calculated to be 0.19(14) MeV and -1.16(14) MeV [24], respectively, making ^{59}Ge to be listed as one of "the most promising candidates for the illusive diproton emission" [24].

Table 1.3: Proton transitions known in ^{23}Si decay prior to this work. Data published in Blank *et al.* [19] and Wang *et al.* [20]. For each work, the proton energy E_p and branching ratio br are summarized, as well as the decay channel.

Blank *et al.* [19]		Wang *et al.* [20]		
E_p [keV]	br [%]	E_p [keV]	br [%]	decay channel
600(60)	< 3	673(36)	2.4(1)	βp
1320(40)	10(1)	1346(39)	5.1(4)	βp
1700(60)	< 5	1631(46	4.6(6)	βp
2400(40)	32(2)	2309(41)	21(2)	βp
2830(60)	14(1)	2730(43)	9.6(1)	βp
3040(60)	7.8(6)	3015(45)	8.9(5)	βp
3650(60)	7.2(6)	3524(65)	8.0(5)	βp
		3811(51)	6.2(1)	βp
4370(60)	2.0(2)	4134(52)	5.0(1)	βp
4760(60)	2.7(2)	4799(56)	2(1)	βp
5860(100)	1.9(2)	5857(66)	0.9(9)	β2p
6180(100)	1.7(2)	6000(64)	0.6(6)	β2p
8680(70)	0.4(1)			βp
9670(70)	0.11(4)			βp
10410(70)	0.07(3)			βp
10930(80)	0.09(3)			βp
11620(100	0.03(2)	.		βp

Table 1.4: β-decay energies (Q_{EC}) of ^{59,60}Ge and separation energies of p, 2p, 3p, ^{3}He and α+p in their respective daughter nuclei ^{59,60}Ga. All the separation energies listed are all within the Q_{EC} window of respective mother nuclei. All energies stem from Ref. [4].

^{59}Ge	^{59}Ga		^{60}Ge	^{60}Ga	
Q_{EC} [keV]	separation energy [keV]		Q_{EC} [keV]	separation energy [keV]	
17390(430)	S_p	-1250(170)	12060(360)	S_p	-340(200)
	S_{2p}	1030(170)		S_{2p}	2500(200)
	S_{3p}	1720(170)		S_α	3380(210)
	$S_{\alpha p/p\alpha}$	4190(170)		$S_{\alpha p/p\alpha}$	3970(200)
	S_α	4550(230)		S_{3p}	5370(200)
	$S_{^3He}$	10060(170)		$S_{^3He}$	7210(200)

In this work, an attempt at identifying the new isotope ^{59}Ge and looking for its decay by 2p emission was performed. After the experiment, another investigation of the same isotopes was performed by Blank et al. [25]. Their results will be presented in Section 5.2.

^{60}Ge

^{60}Ge was discovered in 2005 at NSCL by Stolz *et al.* [26]. It was produced in the fragmentation of a ^{78}Kr 140 A·MeV beam on a Be target. Reaction products were separated by means of the A1900 separator and identified directly on the basis of ToF and ΔE. A total of 3 ions of ^{60}Ge was identified. As the decay of none of them was observed, only a lower limit on the half-life of 110 ns was determined on basis of the time of flight through the separator. The measured cross-section for the production of ^{60}Ge, $\sigma = 0.38^{+0.27}_{-0.31}$ pb, was 3 times smaller than predicted by the abrasion-ablation model [27] and a factor of 300 smaller than EPAX V2 predictions available at the time [28]. A reason for this could be the very short half-life (of about 0.25 μs), due to in-flight decaying via 2p emission. Such interpretation is, however, not compatible with ^{60}Ge being predicted to be stable against both p and 2p decay [24]. Cross sections for less exotic germanium isotopes were measured as well and found to be lower than predictions, but with smaller discrepancy. Shortly after, ^{60}Ge was investigated again at GANIL [29]. This time, a ^{70}Ge beam impinged on ^{nat}Ni target at 72 A·MeV. Identification of 4 ^{60}Ge ions yielded a cross-section 10 times larger than previously measured, suggesting that a Ni target combined with lower beam energy are a better choice when producing the most exotic proton-rich germanium isotopes, but still lower than EPAX V2 predictions for the beam and target combination used. Also in this case, no decay data were obtained. Due to the high β-decay energy and the low separation energies in ^{60}Ga one can expect that ^{60}Ge decay is dominated by β-delayed proton emission as well as that more exotic decay channels are present (see Table 1.4).

In this work, the production cross section for ^{60}Ge was reinvestigated and the first spectroscopic study for this isotope performed.

^{58}Zn

The neutron-deficient zinc isotope ^{58}Zn was produced and identified for the first time by means of the pion double-charge exchange reaction ^{58}Ni(π^+, π^-)^{58}Zn at the Los Alamos Meson Physics Faculty in the late '80s [30]. At the same time, its mass was measured. It was at the time the heaviest T_z = -1 nucleus studied. More than 10 years later its β decay was investigated at ISOLDE [31]. The isotopes of interest were produced in the spallation reaction induced by a pulsed beam of 1 GeV protons on a Nb target and separated from the other reaction products in a chemically-selective laser ion source. Their detection setup included an HPGe detector for γ ray measurement, a β telescope and a charged particle detector consisting of a silicon detector and a gaseous ΔE detector. On the basis of a strong γ transition from the IAS in ^{58}Cu at 203 keV, the half-life of ^{58}Zn was measured to be $t_{1/2}$ = 86(16) ms. One more β transition - GT to an excited state at 1052 keV - was found. On the basis of the non-observation of βp in the decay of ^{58}Zn an upper limit of 3% was set for the respective branching ratio. The half-life was re-measured in 2002 in an experiment dedicated to half-life measurements of ^{78}Kr fragmentation products, $t_{1/2}$ = 83(10) ms [32], and found to be consistent with the previous value. Further studies performed recently at GANIL [33], where the ions of interest were produced in the fragmentation reaction of a ^{64}Zn beam at 79 A·MeV on a ^{nat}Ni target, separated by the LISE3 separator and implanted into a Double Sided Silicon Strip Detector (DSSSD), resulted in neither the observation of new γ transitions, nor βp identification. However, the half-life was measured with much better accuracy, $t_{1/2}$ = 86(2) ms.

Figure 1.8 summarizes the experimental data available on ^{58}Zn prior to this work. In these studies, the decay of ^{58}Zn was reinvestigated to search for its βp branch and measure the corresponding B_{GT} strength.

Exotic decays data for nuclear astrophysical processes

The study of proton-rich nuclei in this region of the chart of nuclei can provide a significant input for astrophysical simulations of the thermonuclear runaway on the surface of accreting neutron starts

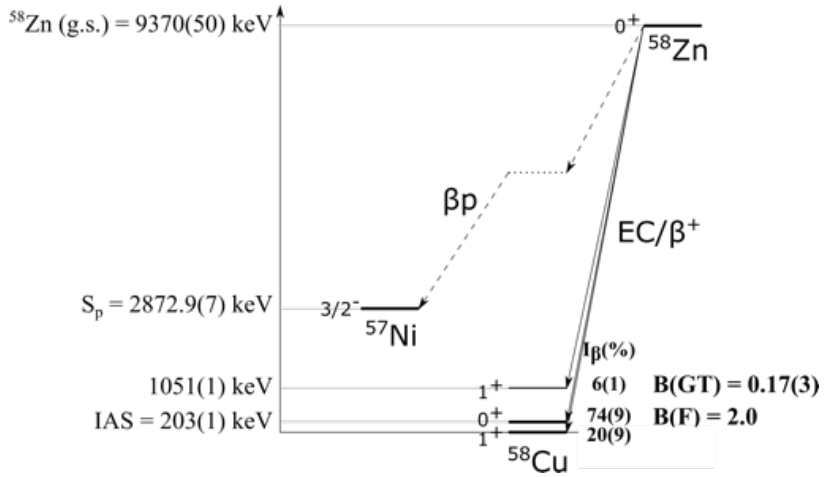

Figure 1.8: Decay scheme of ^{58}Zn as known to date [31, 33]. Information about the energy levels in ^{58}Cu, β feedings I_β, Fermi B(F) and Gamow-Teller B(GT) transition strengths to the levels in ^{58}Cu as well as the half-life stem from [33]. S_p in ^{58}Cu and Q_{EC} value for ^{58}Zn are taken from [4].

driven by the rapid proton capture process (rp), the so-called x-ray bursts [34]. It was shown that βp emission affects the rp process [35]. Both ^{58}Zn and its neighbour ^{57}Zn are placed on the path of the rp process, therefore details on their β decay may provide an additional building block in understanding the creation of heavy elements in the universe.

1.3 Thesis layout

This dissertation presents the results obtained in two experiments aiming at investigating exotic phenomena in nuclear structure at the limits of stability, beyond N=Z line, while climbing from proton-rich silicon nuclei to proton-rich zinc and germanium nuclei along the proton drip line. Chapter 1 provides a description of the physical processes involved and the state of knowledge on the isotopes of interest. It is followed by an explanation of methodologies applied for both production of such nuclei and detection of rare decay modes, involving charged-particle emission (Chapter 2). The experiments at the core of this work are described in Chapter 3 and the results of both of them are presented and discussed in Chapters 4 and 5. A summary closes the work (Chapter 6).

Publications stemming from this work are reported in the following.

1. ^{59}Ge: Ciemny A. A., Dominik W., Ginter T., Grzywacz R., Janas Z., Kuich M., Mazzocchi C., Pfützner M., Pomorski M., Zarzyński F., Bazin D., Baumann T., Bezbakh A., Crider B. P., Ćwiok M., Go S., Kamiński G., Kolos K., Korgul A., Kwan E., Liddick S., Miernik K., Paulauskas S. V., Pereira J., Rykaczewski K., Sumithrarachchi C. and Xiao Y. *First observation of ^{59}Ge* Phys. Rev. C **92** 014622, 2015.

2. ^{60}Ge: Ciemny A. A., Dominik W., Ginter T., Grzywacz R., Janas Z., Kuich M., Mazzocchi C., Miernik K., Pfützner M., Pomorski M., Bazin D., Baumann T., Bezbakh A., Crider B. P., Ćwiok M., Go S., Kamiński G., Kolos K., Korgul A., Kwan E., Liddick S. N., Paulauskas S. V., Pereira J., Rykaczewski K. P., Sumithrarachchi C. and Xiao Y. *First measurement of ^{60}Ge β-decay* European Phys. J. A **52** 89, 2016.

3. ^{58}Zn: Ciemny A. A., Dominik W., Ginter T., Grzywacz R., Janas Z., Kuich M., Mazzocchi C., Pfützner M., Pomorski M., Bazin D., Baumann T., Bezbakh A., Crider B. P., Ćwiok M., Go S., Kamiński G., Kolos K., Korgul A., Kwan E., Liddick S., Miernik K., Paulauskas S. V., Pereira J., Rogiński T., Rykaczewski K., Sumithrarachchi C., Xiao Y., Schatz H. and Sarriguren P. *First identification of ^{58}Zn β-delayed proton emission* Phys. Rev. C **101** 034305, 2020.

4. ^{22,23}Si: Ciemny A. A., Mazzocchi C., Dominik W., Fijałkowska A., Hooker J., Hunt C., Jayatissa H., Janiak Ł., Kamiński G., Koshchiy E., Pfützner M., Pomorski M., Roeder B., Rogachev G. V., Saastamoinen A., Sharma S., Sokołowska N., Satuła W. and Singh J. *Beta-delayed charged-particle decay of ^{22,23}Si* Phys. Rev. C **106** 014317, 2022.

Chapter 2

Methodology

2.1 Production and selection of exotic isotopes

2.1.1 Nuclear reactions

Nuclei at the edges of stability are produced almost exclusively in nuclear reactions of stable projectile and target. However, if the nucleus has a half-life that is long enough, a radioactive target may be used in particular cases (like in the search for new elements), and/or a radioactive projectile can be used (so-called radioactive beams) [36].

There are few main reaction types that can occur when a nucleus interacts with another. When the available energy is low (close to the Coulomb barrier, typically 2 to 6 MeV/nucleon), two nuclei that collide centrally can fuse together to form a single heavier nucleus, which later de-excites by emission of particles and γ-rays (*fusion-evaporation* reaction). Instead of fusing together, projectile and target can exchange part of their nucleons. After such *transfer*, projectile-like and target-like nuclei appear in the final state. When two nuclei collide peripherally at higher energies (50 MeV/nucleon to 1 GeV/nucleon), a *fragmentation* reaction occurs - this is the breakup of nucleus into fragments (usually projectile fragmentation is used). At higher energies when the projectile is a light ion (e.g. proton, deuteron etc.) and the target a heavier nucleus, the target does not fragment, but part of its nucleons are removed - such process is called *spallation*. Neutron-rich targets can also be the source of neutron-rich medium mass nuclei via *fission* reactions. The latter can also occur as a decay channel of excited heavy nuclei produced via other reactions [12].

Fragmentation

A fragmentation reaction, shown schematically in Figure 2.1, consists of two phases. In the first, *abrasion* phase, rapid interactions appear in the overlapping zone of the nuclei, between the so-called participants. As a result, a part of the projectile nucleus is removed and a highly excited projectile-like pre-fragment is formed. Spectators (target-like nucleus and projectile-like pre-fragment) continue their relative motion in the center-of-mass frame. In the *ablation* phase, the pre-fragment de-excitates by particle and γ emission, fission etc. Due to the high energies involved and momentum conservation, the final fragment has nearly the same direction and kinetic energy as the projectile [36, 37]. For the energies of interest in this work, the fragments leave the target totally ionised (with charge $q = Z \cdot e$, e being the elementary charge), a feature that becomes important when it comes to their separation and identification.

For projectile energies above 100 A·MeV (limiting fragmentation regime) the total reaction cross section depends weakly on the projectile energy and becomes a geometric dependence of mass numbers of target A_T and projectile A_P:

$$\sigma_R = \pi r_0^2 \left(A_T^{1/3} + A_P^{1/3} + a \frac{A_T^{1/3} A_P^{1/3}}{A_T^{1/3} + A_P^{1/3}} - c \right)^2 \tag{2.1}$$

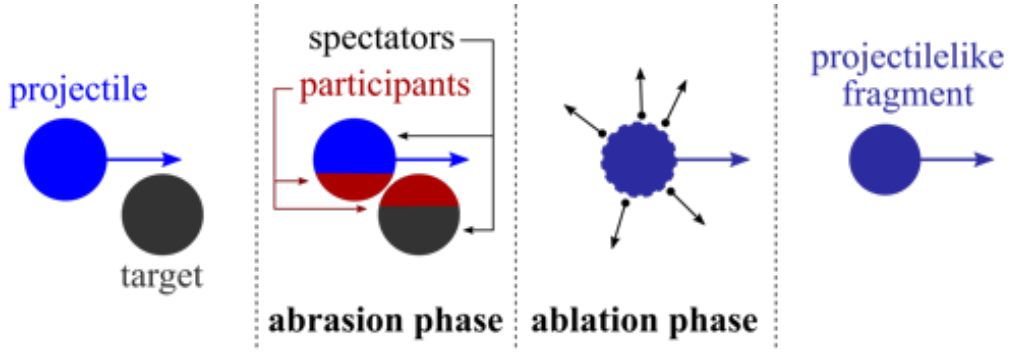

Figure 2.1: Scheme of a fragmentation reaction. See text for details.

where $r_0 = 1.1$ fm is the radius parameter, $a = 1.85$ is the mass asymmetry coefficient, and the parameter $c \approx 2$ introduces a correction for nuclear transparency [38].

For calculating cross sections for production of specific ions in a high-energy heavy-ion fragmentation reaction, a semi-empirical parametrizations like EPAX3 [39] can be used. Several theoretical models describing fragmentation reactions also exist. One of the most sophisticated is ABRABLA, which includes a geometrical abrasion model and a macroscopic evaporation model to describe both steps of the reaction [27].

Fragmentation is a very fast and universal way of producing practically any nucleus with N and Z smaller (or equal) than those of the projectile. Thus, it is the most frequently used reaction for production of isotopes in the in-flight method [37] (see section 2.1.2) and a key reaction mechanism for radioactive beam facilities [36].

2.1.2 Production and separation methods

The two most often used (and complementary) methods of production and separation of rare nuclei are the ISOL (Isotope Separation On Line) method and the so-called in-flight method. The first one requires a target of a thickness that is at least comparable to the range of the projectile in it. The nuclei produced leave the target by diffusion or effusion into an ion source, from where they have to be extracted. They are ionised (e.g. using high temperatures and/or a laser beam) and accelerated to low energies (few tens of keV). After separation in mass separator, the ions of interest are sent to the detection setup directly or after post-acceleration.

In the in-flight method the target has to be thin compared to the projectile range. The nuclei produced (e.g. in a fragmentation reaction) leave the target with velocity close to that of the incoming beam. Separation of the fragments of interest from the others and from the primary beam is performed in a fragment separator. Afterwards, the nuclei can be transported directly to the detection setup, post-accelerated or stored in a storage ring. Both methods are shown schematically in Figure 2.2.

Advantage of the ISOL method is the high production rate (because of the target thickness), but it is rather slow: it takes tens of ms to transport the reaction products to the detection setup. Thus it is suited for studies of nuclei with at least as long halflifes, where high intensity and purity are required [37].

On the other hand, the in-flight method offers much lower production rate, but it is very fast - the separation and transporting time can be of order of magnitude of μs or less. It also allows for the direct determination of the decay branching ratios, since it is possible to determine ion-by-ion the beam intensity, and for the measurement of the properties of several nuclei at the same time. The in-flight method is ideally suited for the study of the shortest-lived exotic nuclei and search for the most exotic decay modes [37].

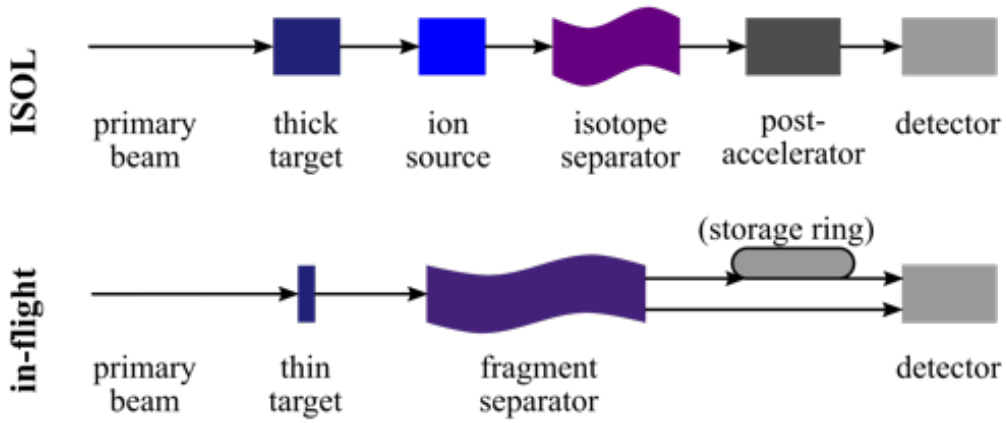

Figure 2.2: General principle of ISOL and in-flight separation. See text for details.

Selection of ions of interest with a fragment separator

A "cocktail" beam after the target contains the fragments of interest but also of other reaction products and the un-reacted primary beam that need to be separated one from another. A fragment separator consists of a set of electromagnetic elements to select and separate the fragments. The main elements use dipole magnetic fields to separate different fragments according to:

$$B\rho = \frac{p}{q} = \frac{\gamma m v}{q} \tag{2.2}$$

where B is magnetic induction of the field in which a particle of mass m and charge q moves with velocity v and momentum p on its path with radius ρ. γ is the Lorentz factor of the particle. As $m \approx A \cdot u$, we get

$$B\rho = \frac{uc\gamma\beta}{e} \cdot \frac{A}{q} = 3.107[Tm]\gamma\beta\frac{A}{q} \tag{2.3}$$

An appropriately set field B bends the beam in such a away that ions of desired $\frac{A}{q}$ are on the trajectory with known (central) ρ. At various stages of the spectrometer, in particular just after a dipole magnet, slits can be mounted to stop fragments traveling on trajectories with different ρ and thus different $\frac{A}{q}$. To improve the separation of the ions, a degrader can be used. The energy losses of an ion in a material depend on its charge (which is equal to Z in case of fully ionized reaction products) according to the Bethe-Bloch formula:

$$-\frac{dE}{dx} = f_C(\beta) \cdot Z \tag{2.4}$$

where

$$f_C(\beta) = C_1 \cdot \frac{1}{\beta^2} \cdot \left(ln\left(\frac{C_2\beta^2}{1-\beta^2}\right) - \beta^2 \right) \tag{2.5}$$

The two constants are $C_1 = \frac{4\pi e^4 z^2 N}{m_e c^2}$ and $C_2 = \frac{2m_e c^2}{I}$, with z being the charge of the moving particle, N being the number of the atoms of the material in one unit of volume and I being the ionisation potential. After the degrader velocities of various fragments will therefore differ. Thus, the next dipole section allows for selecting the A and Z of interest, according to eq. 2.3. A simplified scheme of an in-flight setup is shown in Figure 2.3.

Beside the dipole magnets and the degrader, typical fragment separator contain also higher-order (quadrupole and octupole) magnets for fine-tuning the beam position and its focus and more degraders can be used for obtaining higher beam purity. Usually the higher the purity, the lower the

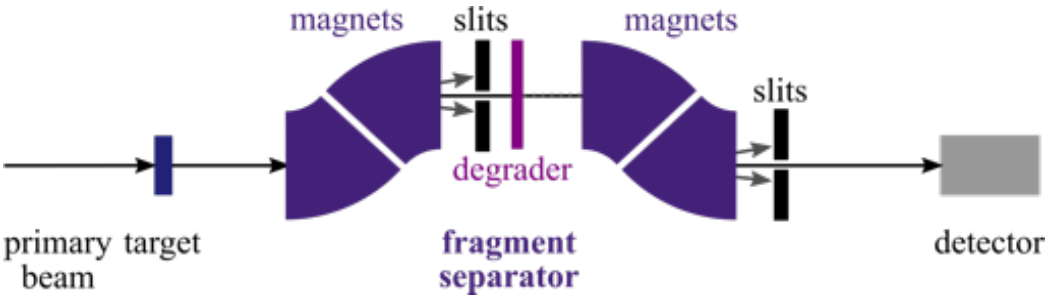

Figure 2.3: Scheme of ions separation with the in-flight method. See text for details.

transmission (intensity) of the beam through a separator. Therefore, a proper configuration has to be determined for a given detector and experiment. Electrostatic ion-optical elements, like e.g. Wien filters, can also be used to further improve the beam purity.

2.1.3 Identification of ions

One of the main advantages of the in-flight technique is the possibility to obtain ion-by-ion identification for the beam components. One of the observables used for ion identification is the time-of-flight (ToF) between two locations positioned on the path through separator, typically intermediary and final focal planes, measured through fast detectors (e.g. scintillators). For fragments of the same velocity this time depends on the distance traveled and thus on the ρ (see eq. 2.2). Time-of-flight is therefore a function of $\frac{A}{q}$. The additional measurement of the energy loss (ΔE) in a detector (e.g. gas or thin silicon detector) allows for identifying each ion's Z. In Figure 2.4 a typical identification plot (id-plot) based on the ToF – ΔE measurement is presented.

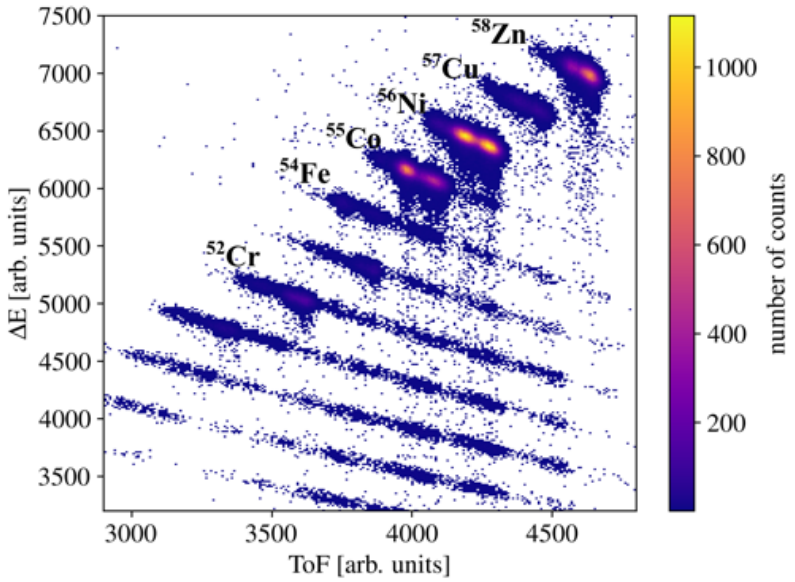

Figure 2.4: Partial identification plot showing ions produced during the experiment performed at NSCL, MSU with ^{60}Ge ion-optics setting - see also Section 3.2. The exotic ions identified are labelled accordingly.

As can be seen in Figure 2.4, the secondary beam contains a mixture (cocktail) of contaminants, since the velocities of the fragments have a distribution. Ion-by-ion identification ensures that only the ions of interest will be chosen for the analysis through proper gating.

Using ions range for identifying fragments

Not all fragment separators have the possibility to have both ΔE and ToF as observable. For example, in the experiment performed at TAMU (see section 3.1), the ToF measurement was not available. Hence, an alternative approach was used for uniquely identifying the ions: in addition to ΔE in a silicon detector, the range of the ion implanted in the active volume of the detector (see section 2.2) was used. This is possible because the energy loss of an ion in a material depends not only on Z of the ion, but also on its mass and velocity. Therefore, the combination of ΔE in a layer of active material and the total range in the detector medium allows also for disentanglement of A and Z. This is shown in Figure 2.5a, where the range of the isotopes studied in the TAMU experiment are plotted as function of the energy with which they entered the detector. The ranges differ visibly between isobars while the difference among isotopes of the same elements are smaller. Nevertheless, the ions can be identified, as shown in Figure 2.5b, where a simulated id-plot based on range and stopping power ($\frac{dE}{dx}$) of the same set of ions is shown for two different ion energies. The energies were calculated to be such that the ions stop around 60% and 70% of the detector length.

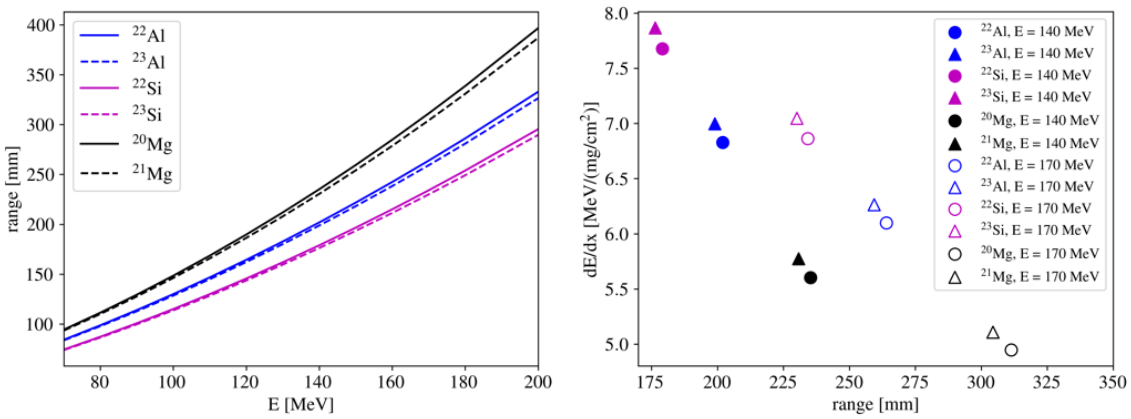

(a) (b)

Figure 2.5: (a) Range-energy dependence for neutron-deficient Mg, Al and Si isotopes. (b) $\frac{dE}{dx}$ versus range of the same isotopes, for two different ion energies (140 MeV and 170 MeV). Energy losses were calculated using the SRIM software [40]. See text for details.

2.2 Detection of charged decay products: Optical Time Projection Chamber

2.2.1 Detector design

The Optical Time Projection Chamber (OTPC) is a type of gaseous detector with optical readout. It was developed in late 2000s at the Faculty of Physics, University of Warsaw, for studying angular distributions in 2-proton radioactivity [41]. Its current version contains an active volume 33 cm deep (x), 20 cm wide (y) and 21 cm high (z) filled with a gas mixture that remains at atmospheric pressure under constant flow and thus constant exchange, therefore maintaining the gas purity and composition. The detector principle is shown schematically in Figure 2.6a. The chamber and whole detector are visible in Figure 2.6b and 2.6c, respectively.

The active volume of the OTPC detector is immersed in a uniform vertical electric field ($\approx 100 - 150$ V/cm). Its homogeneity is assured by the electrodes on the upper (cathode), bottom (anode) and electrodes on the side walls of the chamber. The ions of interest enter the detector horizontally, perpendicular to the field lines through a 50 μm kapton window. The electrodes formed by 7 mm-high strips consisting of 5 μm of Cu and 2 μm of Au, with 3 mm spacing between adjacent strips, are pasted to the side-walls of the detector, including the kapton window. Electrons are generated in the ionisation process by the interaction of the heavy ions and their charged-particle decay

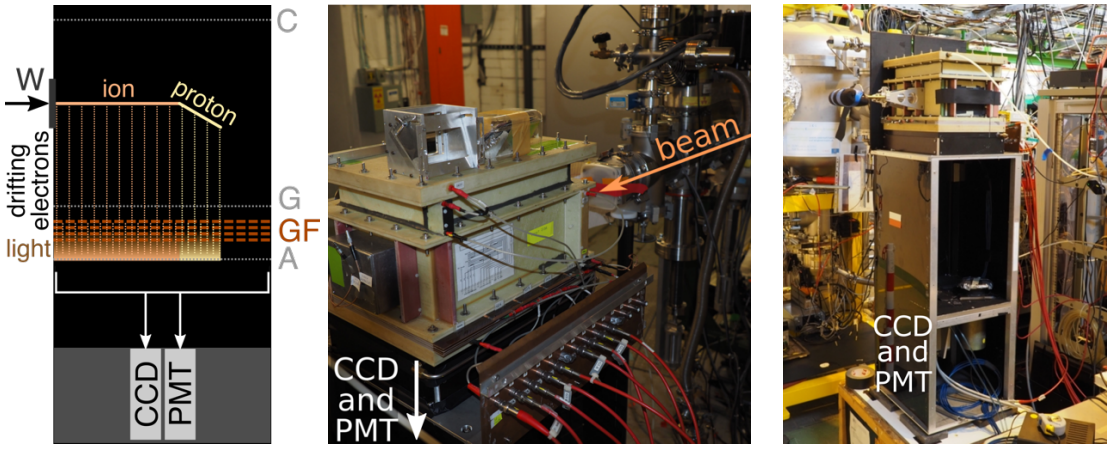

(a) (b) (c)

Figure 2.6: (a) Scheme of the OTPC detector principles. An ion enters the chamber through a window (W). The active volume is immersed in a uniform electric field generated between the cathode (C) and the anode (A). Electrons emitted along the trajectory of the ion and its subsequent decay product (e.g. proton) drift towards the anode and they get multiplied by a stack of GEM foils (GF) before reaching the anode. Light is then emitted and recorded by a CCD camera and a photomultiplier tube (PMT). Before the GEM foils, an additional gating electrode (G) is placed to allow the use of a dual sensitivity mode. (b) Drift chamber of the OTPC detector installed at the National Superconducting Cyclotron Laboratory. Beam from the A1900 separator enters the chamber from the right side of the picture. CCD camera and PMT are installed underneath and not visible in the figure. In front, cables for applying high voltages to the electrodes are visible. (c) OTPC detector. The drift chamber and place of mounting CCD camera and PMT are visible in the upper and lower part of the picture, respectively. The photos in (b) and (c) show the OTPC before the external-light shielding structure is installed. See text for details.

products (protons and α particles; β electrons do not deposit enough energy to be detected) with the gaseous medium. They are produced along the trajectories of ions/particles and drift downwards at a constant velocity (v_{drift}) in the electric field, towards an amplification structure based on a set of four Gas-Electron Multiplier (GEM) foils [42] and the anode. Each GEM foil consists of two copper foils and a kapton layer between them, perforated with numerous tiny holes with diameter 50 μm and a spacing of 150 μm between them. A potential difference of 200-350 V (the value depending on the gas mixture used) is applied between the two Cu layers, generating a very strong electric field inside the holes. Electrons drifting through the holes are amplified by the strong electric field and cause secondary ionisation. Each GEM foil provides a multiplication of the emitted charge by a factor slightly larger than 10.

Between the last GEM foil and the anode another potential difference of a few hundreds V is applied. The multiplied electrons drift in the electric field and excite the gas molecules that de-excite and emit photons of a specific wavelengths. The intensity of the light emitted in this last stage is strong enough to be detected by a camera and a PMT. The chemical composition of the gas mixture in the detector is selected to optimize the light emission in the visible range [43, 44], the number of ions implanted inside the chamber in an interplay with the ions energy, and the range of the stopped decay products.

It is important to mention, that the values of the voltages applied to the detector depend strongly on experimental conditions and therefore are chosen individually for each experiment.

The drift chamber is closed from the bottom by a polycarbonate window. Underneath it, the CCD camera and the PMT are mounted. They are visible in Figure 2.6c. The whole detector is closed by an additional lightproof cover. While the CCD camera records the distribution of light projected on the horizontal (x-y) plane, integrated over the whole camera exposition time, the PMT records the total light as a function of time. Taking into account the constant v_{drift} of the electrons in the active volume of the detector and using $z = v_{drift} \cdot t$, one gets a projection of the particle trajectory

on the z axis, i. e. along the field lines. Thus, the reconstruction of trajectories in three dimensions is possible, see Figure 2.7.

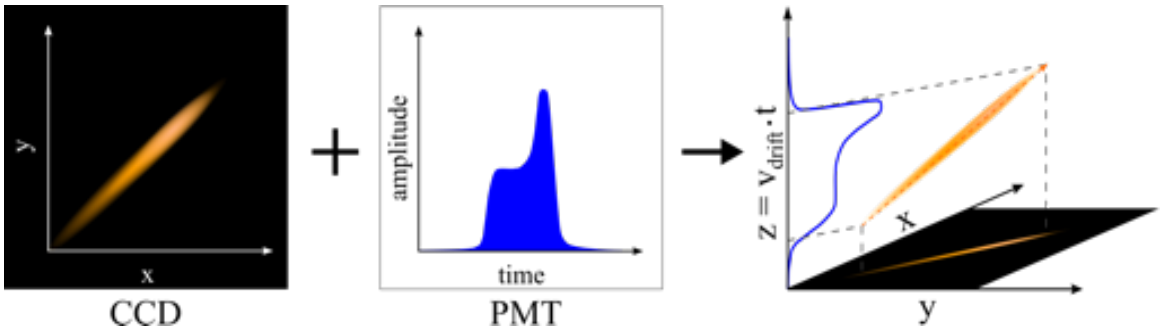

Figure 2.7: Principle of three-dimensional reconstruction of a track recorded by the CCD (x-y projection) and PMT (time distribution). With known v_{drift} of the electrons in the gas, a 3D reconstruction of the trajectory, hence of the momentum, is possible. See text for details.

2.2.2 Data acquisition

Data from the CCD camera are collected in the following way: after a given exposition time, a frame-grabber unit connected to the camera passes the camera frame to the data acquisition (DAQ) computer hard drive via PXI bus. During the data readout, the so-called "camera busy" signal is generated. The PMT signal is recorded by a fast oscilloscope (50 MHz sampling) and saved to the same hard drive via a PCI express card. Two main features characterize the typical operation of the OTPC DAQ, namely the so-called extended-exposure mode for the CCD camera and the dual-sensitivity mode for the whole detector. Both features require a trigger signal. The exact logic behind generating a trigger depends strongly on the experimental conditions, although, it is usually the logical AND of "good ion" signal and the negation (NOT) of the "camera busy" signal. The so-called "good-ion" signal is generated by hardware gates on the ID signals from the ΔE and/or ToF to select only ions that are candidates for the isotope of interest. In this way the system is not triggered by the vast majority of contaminant ions. The OTPC can infact accept only a rate of about 1 Hz.

Extended-exposure mode

There are various ways to stir the CCD camera and manage the time structure of the exposition. In the studies reported in this thesis the extended-exposure mode typical for OTPC experiments was used. In this mode, the CCD camera runs continuously frames of a given exposure time (implantation gate) while waiting for an external trigger. Upon the trigger, the current frame is extended by an observation-window time (decay gate) typically of the duration of a few half-lifes for the ion of interest. Other signals, like camera control and ion identification signals are also collected by fast oscilloscopes.

Dual-sensitivity mode

Ions implanted in the detector are characterised by much higher ionisation intensity than light decay products (mostly protons in these studies), as shown in Figure 2.8. If the electric field applied to the drift volume of the detector would stay constant during implantation and decay gates, either the trajectories of the decay products would be too faint or the charge generated by the ion trajectory would overload the amplification structure and thus overexpose the CCD camera and PMT, not to mention generate uncontrolled avalanches of charge (sparks). For this reason, a dual-sensitivity running mode is used in the OTPC. A gating electrode (G in Figure 2.6a) is installed at the anode-end of the drift region, just before the GEM amplification stage. It reduces the sensitivity of the detector by inverting the electric field just before the amplification stage, hence strongly suppressing the amount of electrons reaching the GEMs. Fine-tuning of the voltage applied to the G electrode

allows to regulate the intensity of the ion track from high intensity to full suppression. Typically, a few volts are sufficient to fully suppress the ion signal. A voltage change on the G electrode switches the mode the detector is in. Such change is managed by a custom-designed unit (gating pulser). While waiting for a good ion to trigger the DAQ, the detector stays in the low-sensitivity mode, which allows for observation of the ions entering the chamber. Within tens of μs from the accepted trigger the voltage is increased and the detector switches to the high-sensitivity mode, which allows to observe weaker-ionising particles. This mode lasts until the end of the observation window/decay gate, when the detector returns to low-sensitivity mode. An example of a typical event recorded by the OTPC detector is shown in Figure 2.9.

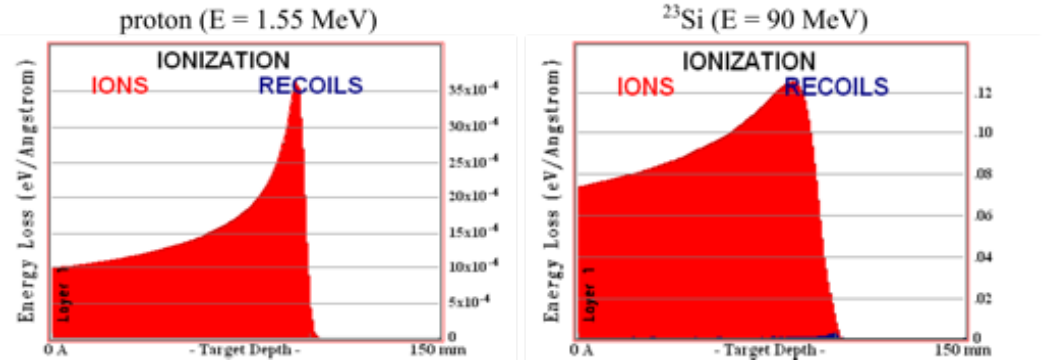

Figure 2.8: Energy losses of a proton (left) and a ^{23}Si ion (right), both having a range of 10 cm, in one of the gas mixtures used in OTPC detector (69% He + 29% Ar + 2% CF_4, see section 3.1). The ion's ionization intensity is around 30 times larger. Energy losses was simulated with the SRIM suite [40].

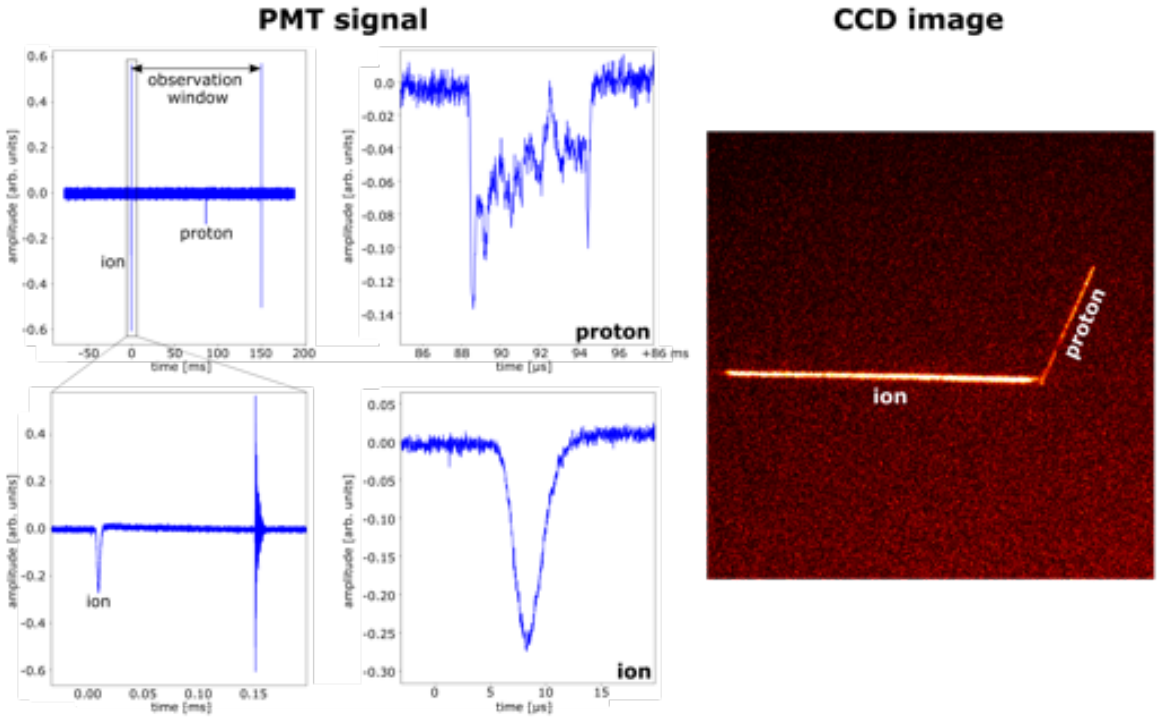

Figure 2.9: An example event recorded by PMT (left) and CCD camera (right). For the PMT signal, the total recorded signal (left top), zoom on the beginning of the decay gate (left bottom), zoom on ion (right bottom) and proton (right top) trajectory, are shown. Thanks to the dual sensitivity mode both ion and proton signals are of comparable amplitude and are well visible in both PMT data and CCD image. The two 0.6 V signals in the PMT data at 150 ms are oscillations happening at the edges of the decay gate (observation window) generated by the gating pulser returning to low-sensitivity mode.

The way in which OTPC collects events imposes certain constrains on the experiment. It needs well identified ions implanted on a one-by-one basis. Moreover, the beam has to be stopped after each trigger during the duration of the whole decay gate while waiting for the implanted ion to decay (however, if this is not possible, a different operating mode can be used in some cases, as it was done for example during search for exotic decay modes of ^{31}Ar [45]). This does not easily allow for experiments with high trigger rate, while it is well suited for studies of rare events. In most cases it allows for unequivocal determination of the number of particles emitted in the decay, their spatial and time correlation and thus to identify exotic decay modes on basis of single events. Moreover, it does not suffer from background from β electrons (because of the too weak ionisation density of the electrons) and thus often allows for completing the low-energy part of the decay product energy spectrum, where difficulties can be encountered in experiments performed with silicon detectors because of β-summing effects. Therefore, OTPC experiments are complementary to studies performed with more traditional silicon-detector arrays.

2.2.3 Drift velocity determination

The conversion of the PMT signal duration into length requires a good knowledge of the electron drift velocity in the given gas mixture and electric field. It can be determined by computer simulations with the Magboltz suite [46] and/or by direct measurement with a drift velocity detector. Such detector consists of a drift volume immersed in a homogenic electric field and filled with the gas mixture of interest, and three single-wire detectors: *pickup* (p), *close* (c) and *far* (f). Two radioactive sources emitting α particles are placed in front of detectors c and f. After applying the appropriate drift voltage, it is possible to measure the time in which the electrons generated as a result of ionization of the gas by the α particle move between pairs of detectors c-p (Δt_{cp}) and f-p (Δt_{fp}), which allows for the drift velocity calculation $v_{drift} = (\Delta t_{fp} - \Delta t_{cp})/d_{cf}$), with d_{cf} = 10cm being the distance between detectors c and f. A sketch of the drift velocity detector principles is shown in Figure 2.10.

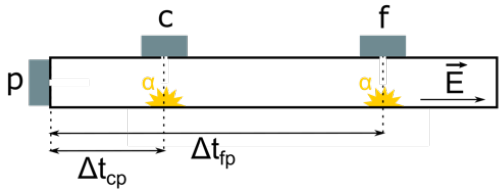

Figure 2.10: A sketch of a drift velocity detector used for measurements. See text for details.

Chapter 3

Experiments

The measurements that form the basis of this thesis were conducted during two experimental campaigns. Neutron deficient silicon isotopes were produced and investigated at the Cyclotron Institute at Texas A&M University, College Station (TX), USA (TAMU experiment). Neutron deficient germanium and zinc isotopes were produced and studied at the National Superconducting Cyclotron Laboratory (NSCL) at Michigan State University, East Lansing, USA (MSU experiment). In each of these experiments, the ions of interest were implanted into and their decays were studied by means of the OTPC detector (see section 2.2). In this chapter the characterizing features and details of each experiments are presented.

3.1 TAMU experiment - silicon isotopes

In the TAMU experiment, ^{22,23}Si ions were produced in the fragmentation reaction of a ^{28}Si beam accelerated to 45 A·MeV by the K500 superconducting cyclotron impinging on a 150 μm-thick nickel target. They were separated from the rest of the reaction products by the Momentum Achromat Recoil Spectrometer (MARS) separator [47]. A schematic representation of MARS is shown in Figure 3.1. Two ion-optics configurations were used for the separator, each optimised for transmission of one of the two isotopes. During the beam-tuning phase, a 300 μm-thick silicon detector, segmented along the vertical direction, was inserted at the focal plane. The ions reaching it were identified on an event-by-event basis by plotting ΔE in silicon detector versus vertical position (Y, corresponding to z in OTPC detector) of the ion - MARS is vertically dispersive (ions traveling on a trajectory with different radius ρ in the magnetic field leave the separator spread vertically) [47]. Slits were inserted to cut off most of the contaminants. The beam obtained was very pure, composed of the ions of interest, ^{22}Si or ^{23}Si, with small amount of other fragments. The ΔE-Y plot before and after use of slits in ^{23}Si setting, as well as ΔE spectra for both settings are shown in Figure 3.2.

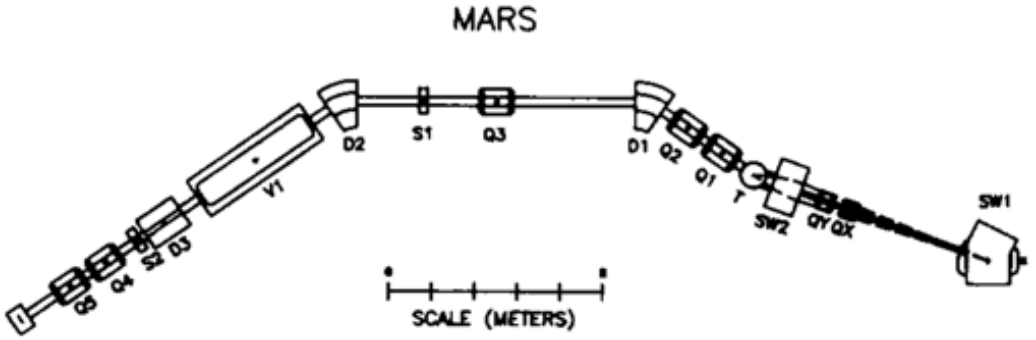

Figure 3.1: Scheme of the MARS separator, figure from Ref. [47].

After the spectrometer optimisation, the detector was removed. The beam reached the detection setup, where its energy was adjusted by use of the aluminium degrader and it was implanted into the

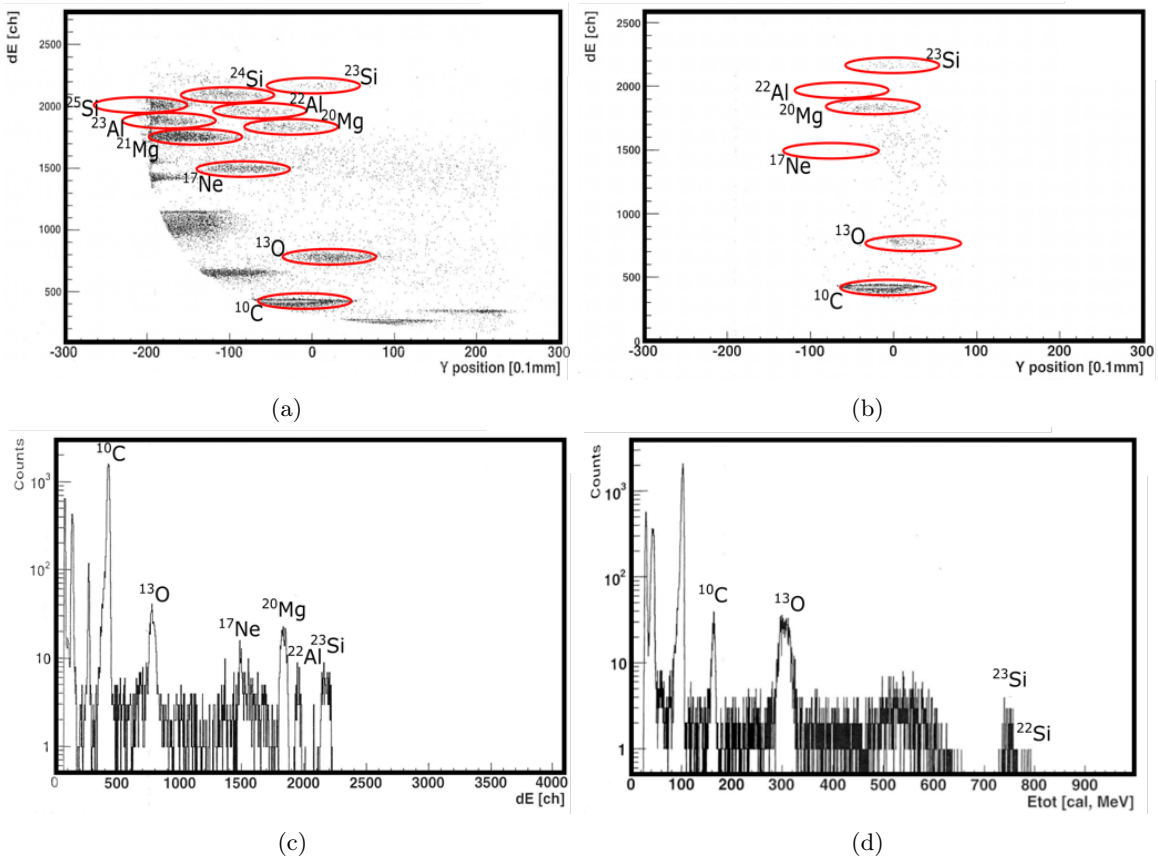

Figure 3.2: ΔE-Y plot before (a) and after (b) inserting the slits (^{23}Si setting). (c) ΔE spectrum of the beam, with slits inserted (^{23}Si setting). The final beam composition consists of the ions of interest, as well as some amount of ^{20}Mg and a tiny addition of ^{22}Al, and lighter ions that were not stopped inside the chamber. (d) Analogous ΔE spectrum for the ^{22}Si setting. Apart from ^{22}Si, some amount of ^{23}Si (and lighter ions) is present.

OTPC detector through a different 300 μm-thick silicon detector (see Figure 3.3a). The ions were stopped in the gas mixture composed of 69% He + 29% Ar + 2% CF_4 at atmospheric pressure. The range of the ions as a function of energy in this gas mixture, calculated using the SRIM software [40] is shown in Figure 2.5a. The average electron drift velocity during the experiment was measured to be v_{drift} = 1.17(2) cm/μs, see Section 4.1.4.

The trigger was constructed by a hardware gate using a single-channel analyzer (SCA) on the ΔE signal from the silicon detector placed just in front of the OTPC (see Figure 3.2a) in anti-coincidence with the camera-busy and computer-busy signals. The gate on the ΔE signal allowed to suppress most of the contaminants from the ions visible in Figures 3.2c and 3.2d and trigger mostly on "good ion" candidates. While waiting for the trigger, the CCD camera was running continuously 65 ms frames (implantation gate - see section 2.2). Upon the trigger, the current frame was extended by 150 ms (decay gate) and the detector was switched to the high-sensitivity mode within 20 μs. At the same time, the beam was switched off for 1.5 s. This time allowed not only to cover the duration of the observation window, but also for readout and saving the 1000 pixels x 1000 pixels image from the CCD camera and the data from the fast oscilloscopes that were recording the PMT signal, the signal from the silicon detector and camera control signals. After 1.5 s the beam was switched on again, see Figure 3.3b.

The ion-by-ion identification was performed off-line on the basis of energy loss in the silicon detector placed in front of the OTPC and the range of the ions in the OTPC itself. The resulting id-plots are presented in Figure 3.4. Details of the experiment settings are summarized in Table 3.1.

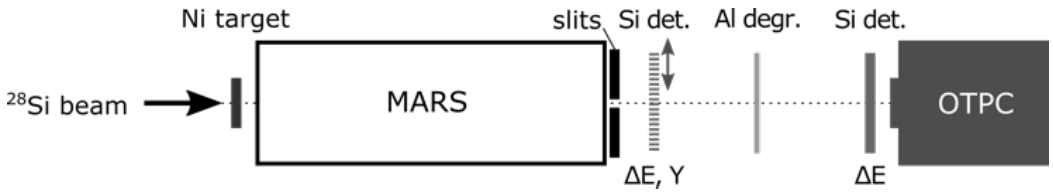

(a)

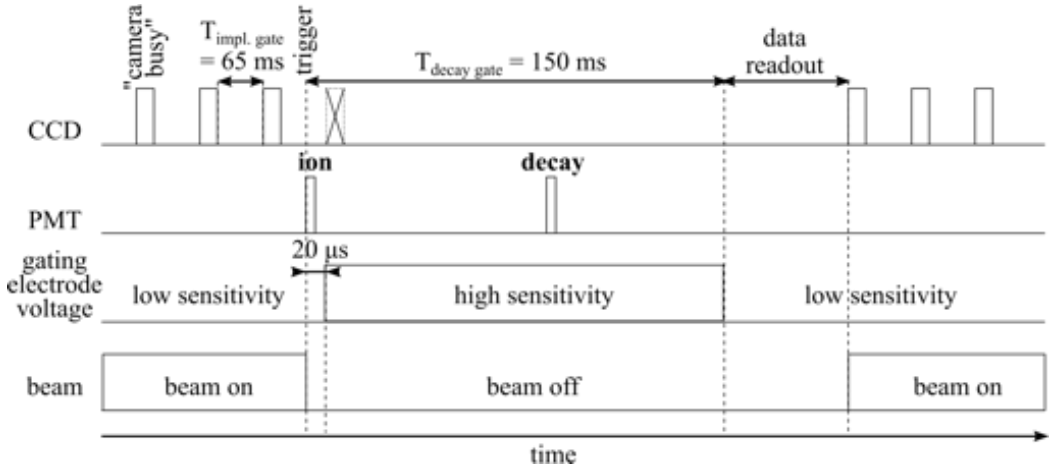

(b)

Figure 3.3: (a) Sketch of the experimental setup. The primary ^{28}Si beam reacts with the nickel target and the reaction products are separated by means of MARS separator. The secondary beam composition is determined via the diagnostic vertically stripped silicon detector (dashed line). The beam energy at the detector is adjusted by an Al degrader for optimum implantation profile. (b) Scheme of the timing of the OTPC DAQ, see text for details. Figures not to scale.

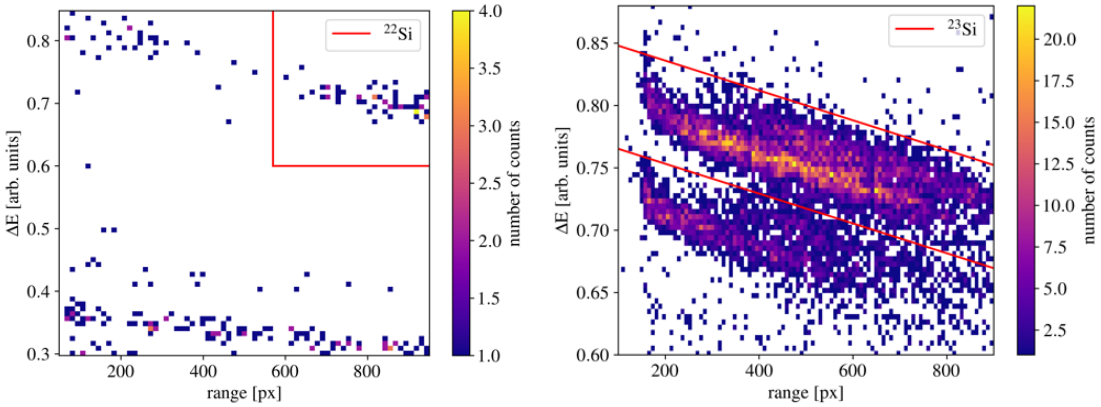

(a) (b)

Figure 3.4: (a) Id-plot with triggering ions in the ^{22}Si setting. The upper part of the plot contains ^{22}Si (right group, within the red box) and ^{23}Si ions (left group, above $\Delta E = 0.6$). The lower part contains events corresponding to lighter contaminant ions not emitting protons. (b) Id-plot with triggering ions in the ^{23}Si setting. The upper part (within the red lines) contains events corresponding to ^{23}Si ions, whereas the lower one is a mixture of mostly ^{23}Si and ^{20}Mg. Both id-plots are based on ΔE in the silicon detector placed in front of the OTPC and the range in the OTPC, given in pixels in the CCD image along the beam axis. The range coordinate in the id-plots is between 50 and 950 or 100 and 900 pixels (for ^{22}Si and ^{23}Si, respectively), since ions implanted outside these limits, i.e. closer to the edge were not taken into account during the analysis. The group of ^{23}Si ions in panel (b) shows an additional structure: it is divided into two sub-groups having different ranges due to the electrode strips on the OTPC entrance window (Section 2.2.1). The vertical spread of the beam was in fact wider than the width of the strip as well as of the interspacing between adjacent strips, hence some of the ions faced a thicker entrance window than the others, resulting in larger energy losses. The same applies to all ion groups, but it is less visible elsewhere. The id-plots contents were verified by observing the decay of the ions and measuring their half-life. Details on this analysis are given in Section 4.1.

3.2 MSU experiment - germanium and zinc isotopes

In the MSU experiment, neutron deficient germanium and zinc isotopes were produced in the fragmentation reaction of a $^{78}Kr^{34+}$ beam with energy 150 MeV/nucleon and a 200 mg/cm^2 beryllium target. The ions of interest were separated from the rest of the reaction products by means of the A1900 separator. Its scheme is shown in Figure 3.5. Ion-optics of the A1900 was set individually for each of the germanium isotopes of interest, i.e. $^{59-62}$Ge.

The beam was implanted into the OTPC detector placed at the end of a transmission line (in the experimental S2 vault). The active volume of the detector was filled with the gas mixture consisting of 49.5% He + 49.5% Ar + 1% CO_2 at atmospheric pressure. The average electron drift velocity during the experiment was measured to be v_{drift} = 1.05(1) cm/μs. The scheme of the experimental setup is presented in Figure 3.6.

Ion-by-ion identification of the fragments was performed on the basis of the energy loss in a silicon detector in front of the detection setup and ToF measurements. Two (redundant) ToF measurements were performed (ToF1 and ToF2) using TACs, see Figure 3.6.

Two data acquisition systems were running independently. The first one (DAQ1), based on PIXIE16 digitizers [49], was recording ΔE, ToF1, and ToF2 for all ions reaching the silicon detector. The second data acquisition system (DAQ2) is the OTPC data acquisition. Hardware gates were applied on ΔE and ToF1 with SCAs to allow triggering DAQ2 only by germanium ions and a limited amount of respective zinc ion contaminants (see id-plots in Figure 3.7).

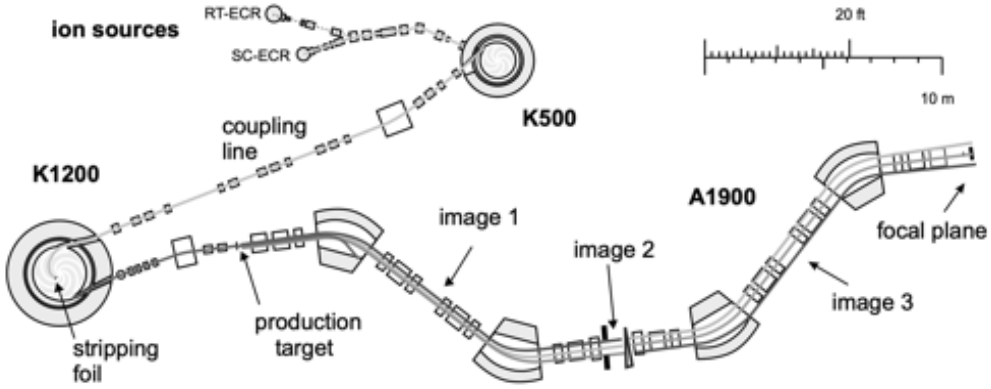

Figure 3.5: Scheme of the NSCL cyclotron facility and A1900 separator, figure from Ref. [48].

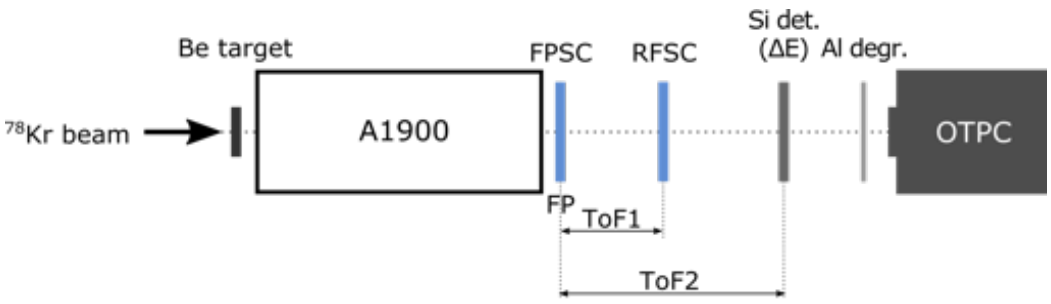

Figure 3.6: Sketch of the experimental setup. The primary ^{78}Kr beam reacts with the beryllium target and the reaction products are separated by means of A1900 separator. Two time-of-flight measurements were performed: between a scintillator (FPSC) at the focal plane of the spectrometer (FP) and a scintillator (RFSC) positioned downstream from it (ToF1), and the ToF between the FPSC and the silicon detector (ToF2). The energy loss of the ions was measured by a silicon detector upstream from the OTPC. The energy of the secondary beam was optimized by means of an aluminium degrader installed before the entrance window of the OTPC detector to maximize the implantation rate.

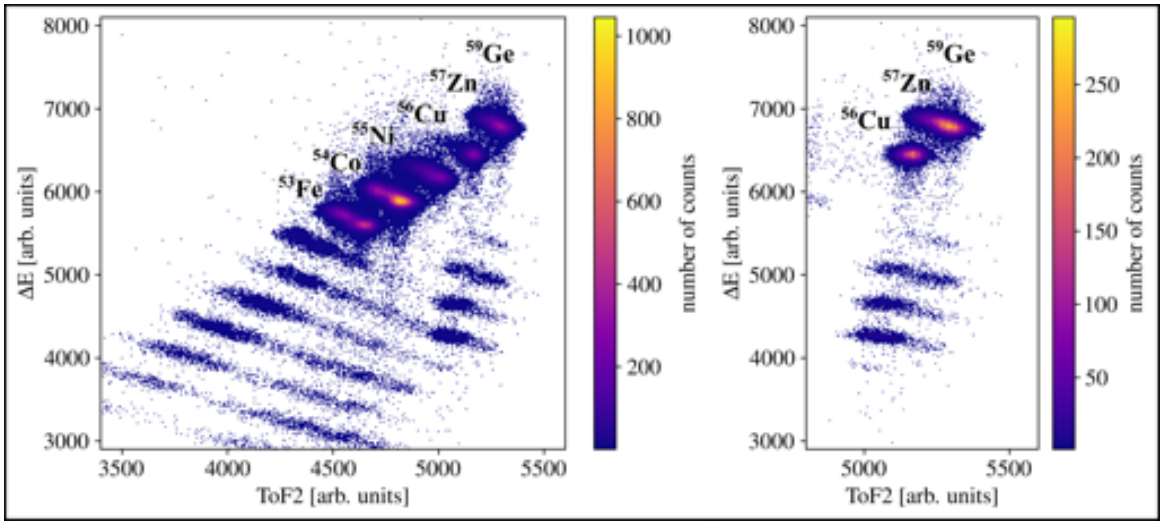

(a)

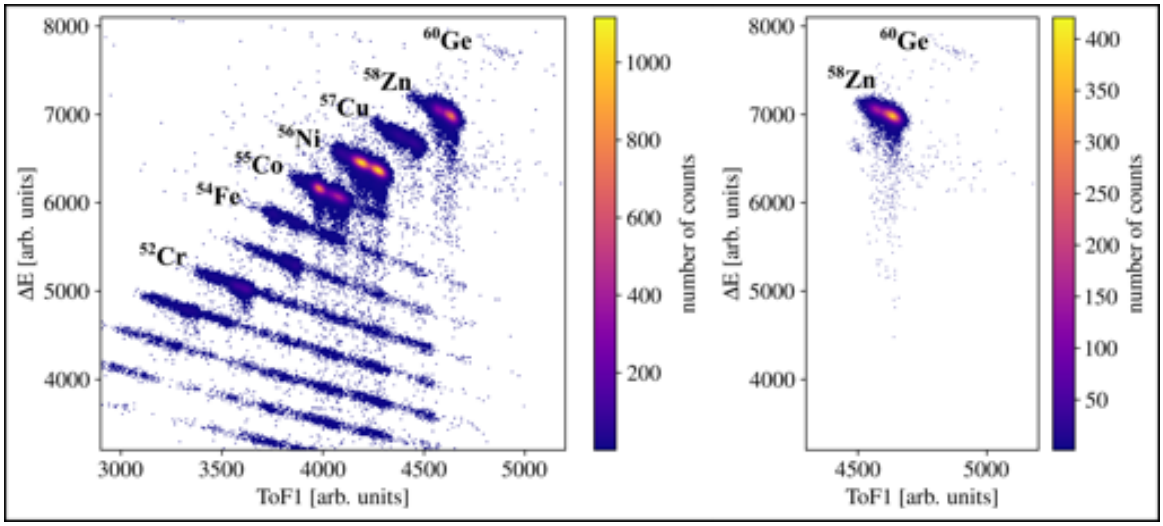

(b)

Figure 3.7: Identification plots for (a) ^{59}Ge and (b) ^{60}Ge settings. In the plots on the left-hand side, all ions reaching the detection setup in the last implantation gate before each trigger are shown. On the right-hand side, only the triggering ions are shown. All the data in these plots stem from DAQ2. For each of the settings, the ToF resulting in better resolution was chosen: ToF2 and ToF1 for ^{59}Ge and ^{60}Ge setting, respectively.

While waiting for a triggering ion, the OTPC was kept in low-sensitivity mode, with CCD camera running continuously 32 ms frames. After the trigger, the CCD frame was extended by 100 ms and the detector changed to high-sensitivity mode within 100 μs. At the same time, the beam was switched off for the whole decay observation window to prevent additional ions from entering the system while waiting for the decay of the implanted ion. DAQ2 recorded the PMT waveform acquired by a digital oscilloscope from the beginning of the last implantation gate, before the trigger, until the end of the decay gate, the image from the CCD camera, ΔE from the silicon detector and the waveforms of the ToF1 and ToF2 signals. All events recorded by both DAQ1 and DAQ2 were time-stamped to ensure the synchronicity between them. The identification redundancy was of great importance to ensure correct identification of the new isotope ^{59}Ge. The trigger scheme is shown in Figure 3.8. Details of the experiment settings are summarized in Table 3.1.

Table 3.1: Details of the experiments settings and configuration. Energies are calculated with LISE++ [50] and the maxima of the distributions are given. In the case of ^{59}Ge, no ion was implanted. Since the aim of ^{61,62}Ge measurement was the cross-section determination and the OTPC was not used, some of the parameters (energies, degrader thickness) are not given for these isotopes.

	TAMU	MSU
date	February – March 2017	June, September 2014
separator	MARS [47]	A1900 [48]
beam (isotope, energy)	^{28}Si @ 45 A·MeV	$^{78}Kr^{34+}$ @ 150 A·MeV
target (isotope, thickness)	150 μ m-thick nickel (= 134 mg/cm^2)	200 mg/cm^2 beryllium (= 1080 μm)
reaction	projectile fragmentation	projectile fragmentation
gas mixture	69% He + 29% Ar + 2% CF_4	49.5% He + 49.5% Ar + 1% CO_2
electric field in the active volume	143 V/cm	125 V/cm
drift velocity	1.17(2) cm/μs	1.05(1) cm/μs
trigger	hardware gates + ΔE from silicon detector (cut in Y, SCA)	hardware gate on ToF1 and ΔE (DAQ1) (SCA)
implantation gate	65 ms	32 ms
decay gate	150 ms	101.25 ms (part of ^{60}Ge setting) 102 ms (^{59}Ge, part of ^{60}Ge setting)
time of switching to high-sensitivity mode	20 μs	100 μs
energy of ions before the Al degrader	^{22}Si setting: 31 A·MeV ^{23}Si setting: 32 A·MeV	^{59}Ge setting: 77 A·MeV ^{60}Ge setting: ^{60}Ge: 74 A·MeV ^{58}Zn: 70 A·MeV
energy of ions entering the OTPC active volume	^{22}Si setting: 1.2 (or: 1-5) A·MeV ^{23}Si setting: 10 A·MeV	^{59}Ge setting: 12 A·MeV (no ion impl.) ^{60}Ge setting: ^{60}Ge: 13 A·MeV ^{58}Zn: 10 A·MeV
thickness of Al degrader in front of the OTPC	^{22}Si setting: 132 μm ^{23}Si setting: 150 μm	^{59}Ge setting: 1.34 mm ^{60}Ge setting: 1.24 mm
time of data taking	^{22}Si setting: 2.5 d ^{23}Si setting: 3.5 d	^{59}Ge setting: 6.2 d ^{60}Ge setting: 2 d ^{61,62}Ge setting: 2 h
identification	ΔE – range	ΔE – ToF
CCD camera model	Texas Instruments MC285SPD-L0B0	Hamamatsu EM-CCD C9100-13
PMT diameter	3.5"	5"

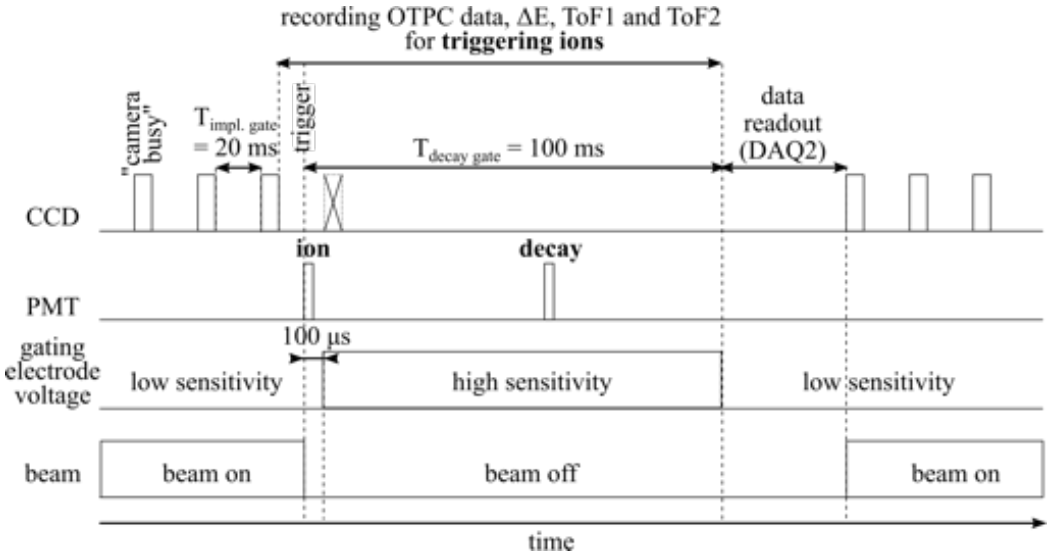

Figure 3.8: Sketch of the timing for the OTPC DAQ2 for the MSU experiment, see text for details.

Chapter 4

Neutron-deficient Si isotopes

4.1 Data analysis

4.1.1 Selection of the ions of interest

The first step in the data analysis consisted in selecting the ions of interest. In Section 3.1 the online identification of ions is described: Figures 3.4(a) and 3.4(b) show the id-plots with triggering ions in the ^{22}Si and ^{23}Si settings, respectively, together with the gates on basis of which the ions were chosen. The way in which the gate limits were established is described in the following. As the ions were identified on the basis of ΔE and range in the detector, Figures 3.4(a) and 3.4(b) were prepared offline and show only ions that entered the OTPC detector.

In order to maximise the detection efficiency for the emitted charged decay products, it was important to make sure that each ion of interest was implanted not only within the active part of the OTPC detector, but also at some distance from the walls. This was necessary to avoid the situation in which a proton will be emitted very close to the chamber wall, towards it, and therefore will not be recorded. It was checked that the ions entered the chamber close to its middle in y-direction (width), as shown in Figure 4.1. The beam was with good approximation parallel to the chamber length, i.e. the x-direction. This was concluded from the fact that the difference in y-direction between the implantation point of an ion and the end of its trajectory (corresponding to the point from which a decay was observed) was negligible with respect to the chamber size (see Figure 4.2).

As for the z-direction, the beam spot was at $\frac{1}{3}$ of the chamber height, $z = 7.0 \pm 1.0$ cm (see Section 2.2.1). The direction with largest spread was along the length of the chamber, corresponding to the beam axis, the x-direction. Implantation profiles along this direction are shown in Figure 4.3.

Gate in ^{22}Si setting

In the ^{22}Si setting, ions were stopped close to the back wall of the detector. Considering also the limited statistics, an ion was considered as implanted if it stopped not further than in 95% of the chamber length. A lower limit of the range gate was set to 57% because of the ^{23}Si admixture that has similar ΔE and that was implanted closer to the entrance of the detector. As the length of the chamber was exactly the size of the CCD picture (1000 pixels), the $> 57\%$ gate correspond to pixels 570-950. The group of ^{22}Si is well separated from the other ions with lower ΔE, which is why a lower boundary of the gate in this dimension was chosen to be a constant ΔE = 0.6 (in arbitrary units), as visible in Figure 3.4(a). During the experiment, 63 ^{22}Si ions implanted correctly were identified and hence considered in further steps of the analysis.

Gate in ^{23}Si setting

Ions in ^{23}Si setting were considered as correctly implanted within 10% and 90% of the chamber length, which corresponds to pixels 100-900. Since there was a significant component of ^{20}Mg ions

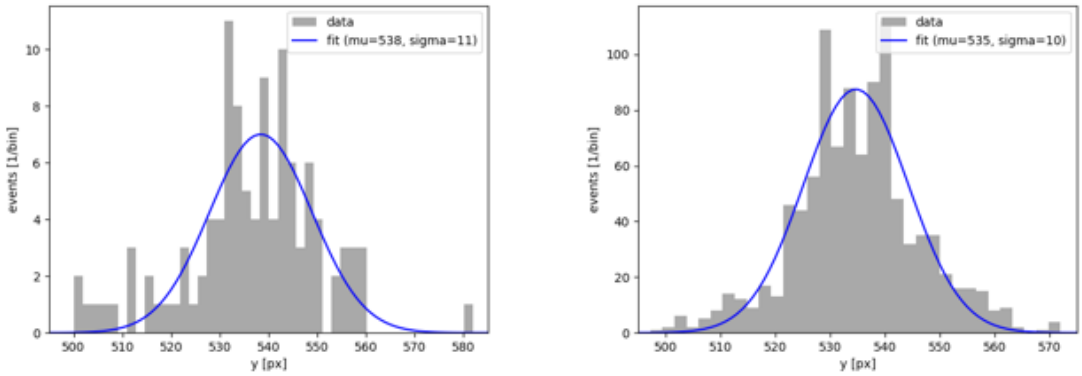

(a) (b)

Figure 4.1: Distribution in y-direction of the implantation points of (a) ^{22}Si and (b) ^{23}Si ions. To each distribution a Gaussian function was fit. The parameters resulting from fitting are given on the plots. During data analysis, first the events with proton emission were selected, and secondly, the ion and proton trajectories within these events were analysed in more detail. For this reason both these and the distributions in Figures 4.2 and 4.3 are based on a data subset in which only events containing proton emission are. As the μ value of two fits equals to pixels 538 and 535 in ^{22}Si and ^{23}Si setting, respectively, and the middle of the chamber corresponds to pixel 517.5, the distance between the centroid of the distribution and the center of the chamber along x, was around 6 mm in both settings.

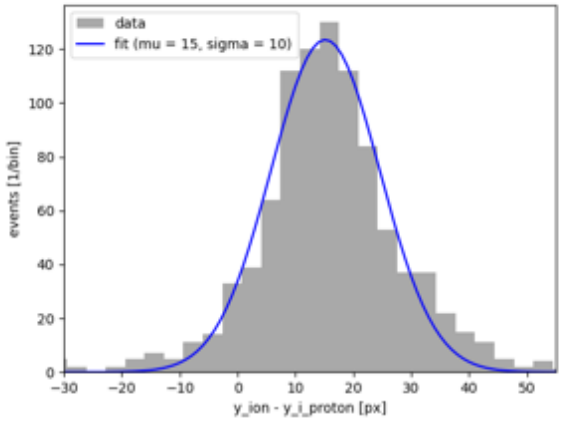

Figure 4.2: Distribution of the difference between y of the implantation point of an ion and y_i of the proton trajectory corresponding to the y_f of the ion trajectory for the ^{23}Si ions trajectories. A Gaussian function was fit to the distribution. $\mu = 15$ px corresponds to less than 5 mm with the mean length of the ion trajectory of ≈ 16 cm. The beam was therefore considered to be parallel to the x-axis.

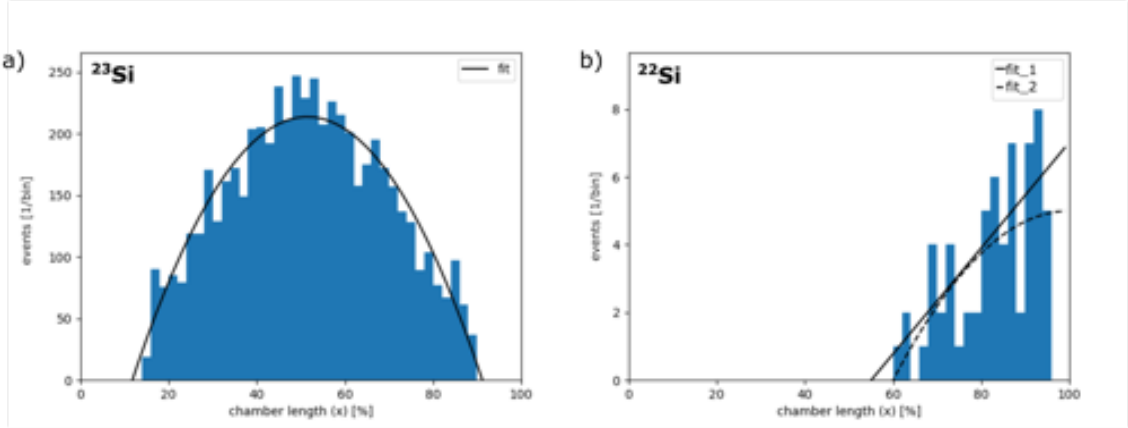

Figure 4.3: Implantation profiles of ^{23}Si (left) and ^{22}Si (right) along the x-axis (beam axis). A 2$^{\text{nd}}$ order polynomial was fit to the distributions and used for the proton stopping efficiency simulations, see text for details. To the ^{22}Si distribution two polynomial functions were fit. First (fit 1) was a quadratic function with all coefficients being fit parameters. Second (fit 2) was of the same shape as the function fit to the ^{23}Si distribution, with position in x being the only fit parameter.

with similar y-position and slightly lower ΔE (as visible in Figure 3.2(b)), no cut in constant ΔE was possible. Instead, a linear dependence of ΔE from the range marks the limits of the gate. Figure 4.4 shows the projection of the ions distribution on the axis perpendicular to the gate edges. It can be seen that the selected boundaries delimit the chosen ^{23}Si ion group well. In further steps of the analysis, the half-lifes of the ion groups were calculated to verify their composition (see Section 4.3). A total of 7497 ^{23}Si ions met the requirements set by the gate and were considered for further analysis.

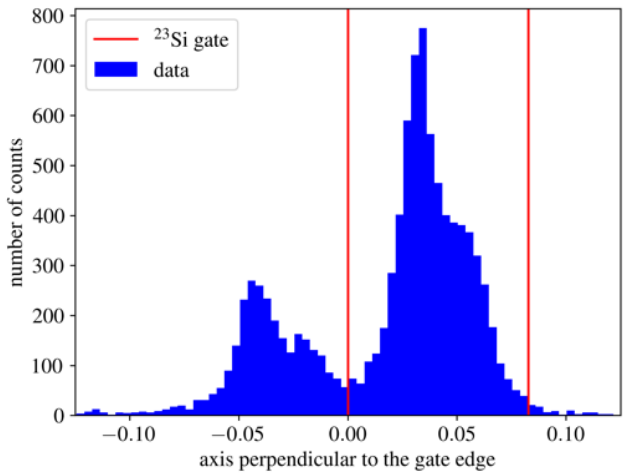

Figure 4.4: Projection of the ions distribution on the axis perpendicular to the gate edges in the ^{23}Si setting. The group on the right corresponds to the ^{23}Si ions (upper group in the id-plot in Figure 3.4(b)). The group on the left corresponds to the lower group in the id-plot consisting of a mixture of ^{20}Mg and ^{23}Si (see text for details). In both groups, a sub-structure caused by the electrode strips on OTPC detector entrance window is visible (see caption of Figure 3.4).

4.1.2 Stopping efficiency simulation

The distribution of the implantation points of the ions shown in Figure 4.3 served as input to the Monte Carlo simulations of proton stopping efficiency in the detector under the conditions of this experiment. This simulation was needed to determine how many of the emitted protons of a given

energy will be fully stopped inside the OTPC, and therefore its energy will be determined correctly, as well as to determine the energy deposit in the chamber of the protons that escaped.

The simulation of a single proton consisted of the following steps:

- An ion entered the chamber through the front window at position (y, z). The distribution of position in y was obtained from the Gaussian fits results shown in Figures 4.1(a) and 4.1(b) for ^{22}Si and ^{23}Si, respectively. The distribution in z was a Gaussian with $\mu = 7.0$ cm and $\sigma = 1.0$ cm, see Section 4.1.1.
- The ion was assumed to move parallel to the x-axis. Its range was taken from the polynomial distribution fit to the data (Figure 4.3). In case of ^{22}Si, fit 2 was used for the final simulation. It was verified that the choice between fit 1 and 2 in Figure 4.3 does not change the shape of the obtained efficiency function.
- A proton with a fixed energy E_p was emitted from the point in which the ion stopped, the angles of the proton emission were assumed to follow an isotropic distribution. The range of the proton was calculated based on the energy-range dependence obtained with SRIM software [40] for the gas mixture used in experiment.
- The proton was considered as stopped within the detector if its trajectory ended inside the detector, and the distance between its endpoint and the side/front/back wall was not smaller than 5% of the chamber size in respective dimensions. The 5% boundary was chosen on the basis of the distribution of the real protons stopping points in the CCD $(x - y)$ plane, which is shown in Figure 4.5.

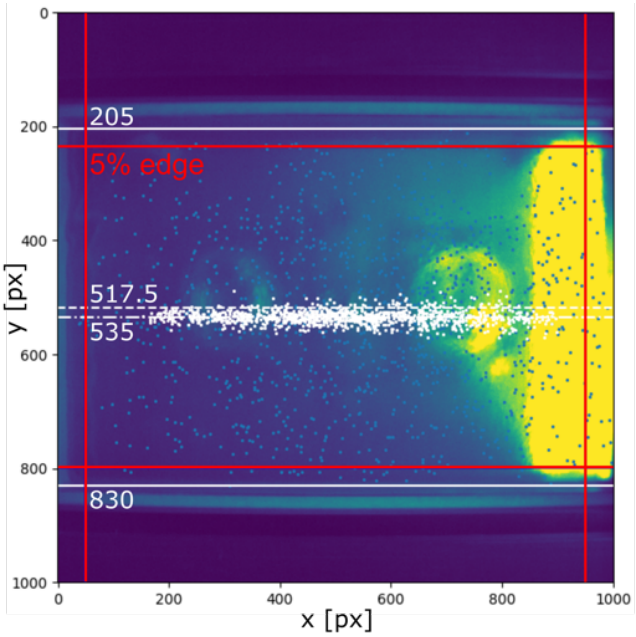

Figure 4.5: OTPC chamber as seen by the CCD camera. The CCD camera was adjusted in such a way that the x-edges of the chamber corresponded exactly to the edges of the picture. The white vertical lines are the walls of the chamber in y. $y = 517.5$ px is the middle axis of the chamber, while $y = 535$ px is the middle of the ^{23}Si ions stopping points (white dots) distribution. Blue dots are trajectory endpoints of protons preliminarily considered as stopped due to the visible Bragg peak. For the final analysis 5% edge (red lines) was chosen to assure that protons have stopped within the detector and to avoid events in which the end of the trajectory of the proton hitting the detector wall might look similar to the Bragg peak.

The simulation covered all values of E_p from 0 to 3.5 MeV, in 25 keV steps. For each E_p, 1M protons were considered. The efficiency for each step was the ratio of stopped protons to all protons. The efficiencies obtained in this way for both Si isotopes are shown in Figure 4.6.

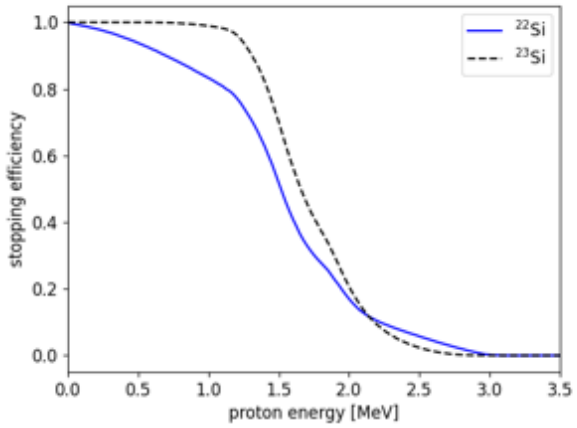

Figure 4.6: Stopping efficiency as a function of proton energy simulated for ^{22}Si (solid blue line) and ^{23}Si (dashed black line). The efficiency for ^{23}Si is nearly 100% for protons with energies below 1.3 MeV, after which it sharply drops and gets close to zero around 2.5 MeV. The high efficiency at low energies is thanks the implantation profile of ^{23}Si ions, being well centered in the chamber, see Figure 4.3. In the case of ^{22}Si, the efficiency does not have a plateau at low energies. Instead, the decrease in efficiency starts immediately and is more gradual. The efficiency drops to zero only at approximately 3 MeV. This is to be attributed to the fact that the center of the ^{22}Si implantation distribution was located outside the detector. Consequently, most of the ^{22}Si ions were stopped in the back part of the OTPC. As a result, low-energy protons emitted in the forward direction (relative to the beam direction) could escape from the detector, while high-energy protons emitted in the opposite direction could be stopped.

For calculating the energy deposit spectrum, the steps followed for a single proton were similar, but all the protons were assumed to have range larger than the dimensions of the chamber. For each proton, the distance between the emission point and the point in which it hit the top/bottom wall or the boundary distant by 5% from the other walls was converted to energy deposited in the detector on basis of SRIM tables. The spectra were simulated for 1M protons for both ^{22}Si and ^{23}Si and are shown in Figures 4.7a and 4.7b.

4.1.3 Observation probability

Due to the finite-time observation window, there is a non-zero probability that a decay event occurs after the recording of the event has been completed. The probability of observing a β-delayed particle emission within the observation window was therefore determined by the integral $\frac{1}{\tau}\int_{t_i}^{t_f} e^{-t/\tau}\,dt$, where t_i and t_f are the beginning and the end of the observation window with respect to the production time of an ion, respectively, and $\tau = t_{1/2}/\ln 2$ is the lifetime of the decaying isotope. The half-lifes taken into account were uncertainty-weighted averages of literature values for each isotope (see Section 1.2.1) and the observation window spanned from 100 μs (begin of the observation window) to 150 ms (see Section 3.1). The values of observation probability were calculated to be $P_{obs}(^{22}Si) = 97.2(6)\%$ and $P_{obs}(^{23}Si) = 92.1(2)\%$. Once $t_{1/2}$ values for both isotopes were determined from the analysis of the experimental data, the observation probabilities were recalculated taking into account the additional half-life value in the weighted average. In this way, it was verified that the branching ratios were not affected beyond the uncertainties, and the probabilities derived from literature data (having smaller uncertainty) were used for the final values.

4.1.4 Drift velocity

In order to convert the duration of the PMT signal into the z-component of the particle range, the drift velocity of the electrons in the given gas mixture and electric field is needed. For technical reasons it was not possible to measure it directly during the experiment, and it had to be determined

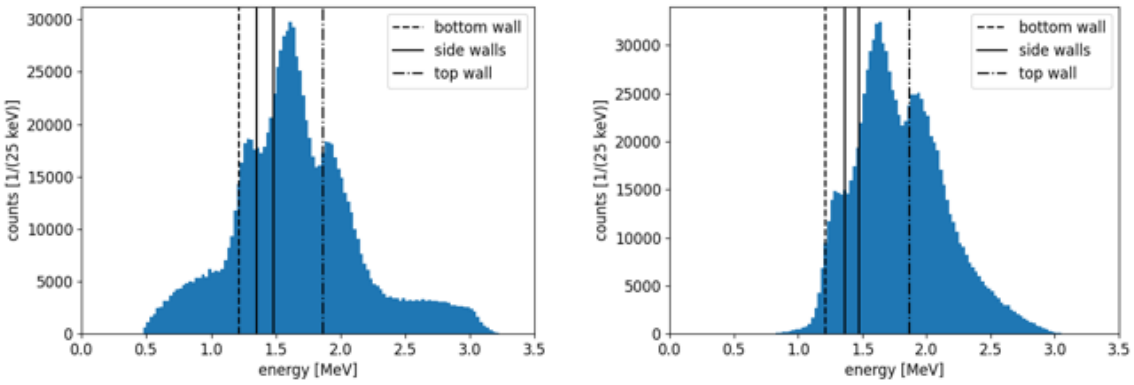

(a) (b)

Figure 4.7: Energy deposit spectra obtained in the simulation for (a) ^{22}Si and (b) ^{23}Si. They both exhibit three peaks in the central region. The left slopes of these peaks correspond to the energies of protons emitted directly towards and exiting the detector through the lower- (left peak), side- (middle peak), and upper (right peak) walls. These peaks are similar for both ^{22}Si and ^{23}Si case due to the similar distribution of ions in y and z directions, with only a slightly different position relative to the side walls, see Figure 4.1. However, the components of the spectra resulting from the distribution along the x-axis are different. The energy deposit distribution of ^{22}Si has two broad tails spanning from 0.5 to over 3 MeV. This broad range is caused by the emission of protons mostly in close proximity to the back wall of the detector, resulting in the possibility of depositing both low- (when emitted towards the back wall) and high- (when emitted towards the detector entrance) energy inside the chamber. In contrast, the energy deposit distribution for ^{23}Si is narrower. This is because the protons were mostly emitted from the central region of the chamber, where the distances to the front and back walls and, consequently, the amount of energy deposited in the detector, were similar to the distance to the top wall. This explains the higher intensity of the third, highest-energy peak.

a posteriori. The values of v_{drift} for the used gas mixture and electric field in different meteorological conditions were obtained by simulation with the Magboltz software [46]. 77 simulations were performed for pressures from $P = 990$ hPa to $P = 1040$ hPa in 5 hPa steps and temperature from $T = 18°$C to $T = 30°$C with 2°C steps.

Additionally, v_{drift} was measured with the drift velocity detector (see Section 2.2.3) in the laboratory in Warsaw for the same gas mixture and electric field for two sets of conditions ($P = 1000$ hPa and temperatures $T_1 = 25$ °C and $T_2 = 27$ °C). The values acquired from the drift velocity detector measurements for these two sets of P and T were $v_{drift1} = 12.10(17)\ mm/\mu$s and $v_{drift2} = 12.17(17)\ mm/\mu$s. The results of these measurements were extrapolated using the trends obtained from the simulations to the conditions during the experiment. The temperature and pressure during the whole experimental run were found to be $P = 1030(5)$ hPa and $T = 21(1)$ °C (the stability of the temperature was due to air conditioning in the experimental hall). The resulting v_{drift} was found to be $v_{drift} = 11.7(2)\ mm/\mu$s, with the uncertainty resulting from the uncertainties of the two measurements and the meteorological conditions during the experimental run.

4.1.5 Energy calculation

The energy and the angle θ between the trajectory and the $x - y$-plane were calculated in two ways. The first and main method of determining them was based on the length measurement of the trajectory components:

- The length of the $x - y$ component was calculated on basis of the (x_i, y_i) and (x_f, y_f) points in pixels and the relation $px/mm = 3.2(1)$ known from calibration measurements.
- The vertical component of the trajectory was calculated using duration of the PMT signal and the established drift velocity value.

The ratio of these two components allowed for calculation of θ and the resulting total range was directly related to the energy of the proton via SRIM range tables.

The second way of calculating the energy and θ was to fit the Bragg curve shape to the PMT signal with length of the CCD component (calculated as in the first approach) being given as a constant with the possibility to vary it within the uncertainty limits, and energy and θ being the fit parameters. This approach resulted in a good reconstruction of the shape of the signal and thus accurate energy values, but its use was limited to only part of the statistics for several reasons.

- The GEM foils used in the OTPC consist of 4 parts with breaks between them, which resulted in the deformation of the signal if the proton trajectory runs across such break.
- Protons that are not stopped inside the chamber are characterized by a shape of the PMT signal that differs from Bragg curve. Furthermore, for stopped-yet-high-energy protons the energy losses along the track are low and the noise-to-signal ratio can prevent the proper fitting.
- A significant part of events contained a signal component resulting from the ion recoil, which was not negligible and increased the number of fitting parameters.
- Fitting of more than one trajectory was not always possible with the given data quality due to the increased number of fit parameters and the broad minimum in the $r^2 = \sum(x_{fit} - x_{data})^2$ value landscape.

It is worth mentioning that even more accurate results could have been obtained by simultaneously fitting the Bragg curve shape to both PMT and CCD signals, provided that the noise level in the CCD camera would allow for it. However, it should be noted that the manual readout of the trajectory edges from the CCD was accurate enough to reasonably assume that the potential gain in accuracy would not have been significant.

Even though it was not possible to use the second approach for the whole dataset, it was used to estimate the systematic error of the first method, which could then be applied to all events. From the difference between results of two methods it was found that the width of the PMT signal in the first

was underestimated by around 0.5 μs in average, due to the blur of the signal edges caused by the diffusion of electrons drifting in the gas mixture. As a consequence, the following uncertainties were taken into account while performing the energy calculations using the first approach: for the $x-y$ component, $x_{i,f}$ and $y_{i,f}$ were taken with uncertainty of $(\pm 2px)$ and t_{PMT} was taken with uncertainty of $(\pm 0.5(statistical)\mu s - 0.5\mu s(systematic))$. The uncertainties of the v_{drift} value and px/mm ratio were also taken into account. Due to the limitations listed above, the second approach was used for calculating proton energies from βp events in which the protons stopped inside the chamber (fit quality was verified by means of r^2 value), whereas the first approach was used for calculating partial energies of protons that left the chamber as well as energies in events with emission of more particles. The uncertainties of the reconstructed proton energies spanned from $80-100$ keV at 200 keV to $40-60$ keV at $1000-1500$ keV.

4.2 β-delayed charged-particle decay of ^{22}Si

4.2.1 β-delayed p and 2p emission

63 events correlated with ions that met the requirements described in Section 4.1.1 were further examined for occurence of β-delayed particle emission. The analysis allowed for confirmation of both previously known decay channels of ^{22}Si, namely βp and β2p. Data recorded by CCD and PMT for example events are shown in Figures 4.8(a) and 4.8(b) (βp), and 4.8(c) (β2p). The number of observed events and the calculated branching ratios are summarized in Table 4.1. The obtained values take into account the finite observation window, as described in Section 4.1.3.

Table 4.1: The total branching ratio for the observed ^{22}Si decay channels from this and previous work.

decay channel	number of events	branching ratio (this work)	branching ratio (lit.)
βp	58	$95(^{+14}_{-12})\%$	$\approx 100\%$ [14]
β2p	2	$3(^{+4}_{-2})\%$	0.7(3)% (IAS) [17]

Among the 58 β-delayed protons identified, 24 stopped within the active volume of the detector, within 5% boundaries from the chamber walls (see Figure 4.5). Their energies were reconstructed and their energy spectrum is shown in Figure 4.9. Two groups of low-energy protons can be identified at energies of 0.6(1) MeV and 1.7(1) MeV. The corresponding total branching ratios for them are $10(^{+6}_{-4})\%$ and $77(^{+27}_{-22})\%$, respectively. The lower-energy group corresponds to the proton group identified at 680(50) keV [16] or 710(50) keV [17]. The higher-energy group of protons is located on the slope of the stopping efficiency function and might therefore correspond to the low-energy tail of the two protons transitions known at 1950(50) and 2150(50) keV [17]. Among the two events with β2p emission, none allowed for the total energy reconstruction, as in each case one of protons escaped the chamber.

4.2.2 Half-life calculations

A maximum likelihood fit of the decay time distribution of the events with respect to the time of ion implantation, shown in Figure 4.10(a), yielded a half-life of $25(^{+4}_{-3})$ ms. This result is in agreement with the previously measured values: 29(2) ms [14], 27.8(35) ms [16] and 28.6(14) ms [17] and indicates that the selected ion group consisted exclusively of ^{22}Si ions. Moreover, for 5 events the decay of the daughter nucleus ^{21}Mg by βp emission was observed within the observation window. The times of these decays with respect to the time of βp emission from ^{22}Si are in compliance with the expected distribution, as shown in Figure 4.10(b).

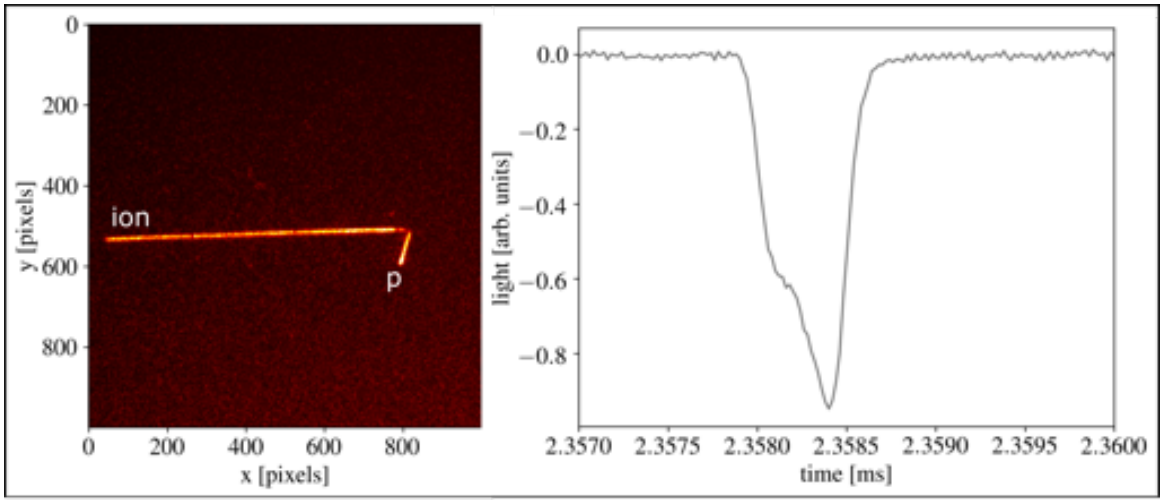

(a)

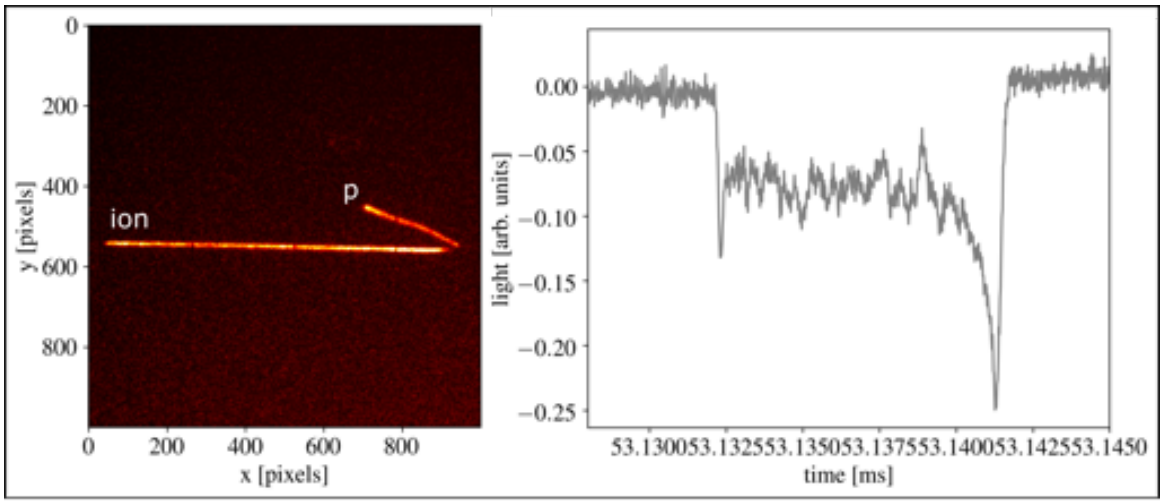

(b)

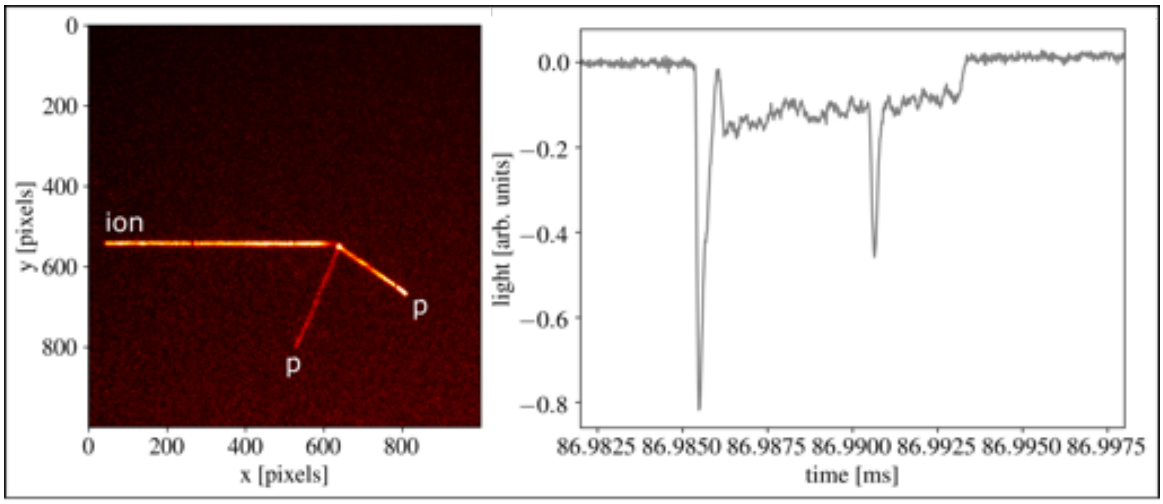

(c)

Figure 4.8: Example data from CCD (left) and PMT (right) for events with βp emission ((a) and (b)), and β2p emission (c) from ^{22}Si. The PMT data are shown around the time of the proton signal. Subfigure (a) depicts a proton belonging to the lower-energy group (see Figure 4.9 below), with $E_p = 0.55(6)$ MeV, whereas the proton visible in (b) belongs to the higher-energy group ($E_p = 1.74(4)$ MeV). Among the two protons visible in subfigure (c), one was stopped inside the chamber (brighter trajectory with visible Bragg peak in the CCD picture corresponding to the more intense peak in PMT signal), and the second one escaped (faint trajectory).

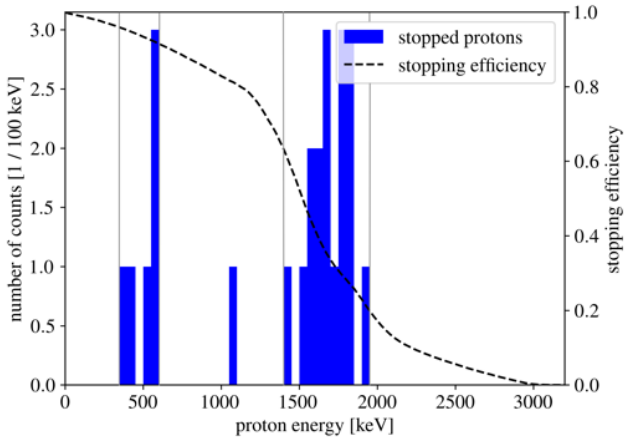

Figure 4.9: Energy spectrum of ^{22}Si β-delayed protons stopped inside the OTPC detector. The dashed black line shows the proton stopping efficiency as a function of energy (see Section 4.1). The vertical gray lines show the limit for the two groups of protons described in the text.

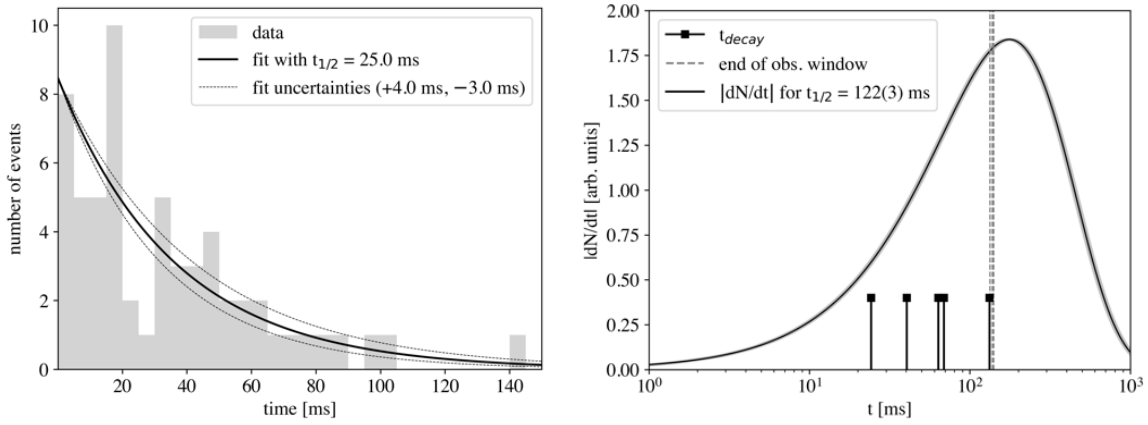

(a) ^{22}Si (b) ^{21}Mg

Figure 4.10: (a) Distribution of decay times for ^{22}Si events (histogram) and the exponential decay curve with half-life $t_{1/2} = 25(^{+4}_{-3})$ ms, which was determined by the maximum likelihood method using an exponential decay distribution with a finite-time decay observation window [51]. (b) Logarithmic distribution of decay times of 5 identified ^{21}Mg decays (black vertical bars). The bell-shaped curve corresponds to the distribution calculated for the known ^{21}Mg half-life value $t_{1/2} = 122(3)$ ms [2]. The dashed lines show the end of the observation window with respect to each of the five decays.

4.3 β-delayed charged-particle decay of ^{23}Si

The gate applied to triggering ions in the ^{23}Si setting allowed for identification of 7497 well-implanted events which were considered for further analysis. The study of the collected PMT and CCD data resulted in the confirmation of the two already known decay channels, βp and β2p, as well as identification of two new decay modes: β3p and βpα. The branching ratios for all the four decay channels are summarised in Table 4.2. The total branching ratio $b_{total} = 90(1)\%$ determined in this study is in good agreement with the previously obtained $\approx 92\%$ [19]. The missing 10% is most likely caused by feeding of the grund state of the ^{23}Al daughter in the β decay of ^{23}Si. Shell-model calculations support such interpretation by giving 6% direct decay to the ^{23}Al g.s. [19].

Table 4.2: The total branching ratios for the observed ^{23}Si decay channels. Observation probability in the finite time window is taken into account. See text for details.

decay channel	number of events	branching ratio (this work)
βp	5643	81.8(11)%
β2p	533	7.73(35)%
β3p	2	$2.9(^{+38}_{-19}) \times 10^{-2}$%
$\beta p\alpha$	1	$1.4(^{+33}_{-12}) \times 10^{-2}$%

4.3.1 Half-life and cocktail beam composition

A maximum likelihood fit of the decay time distribution of all observed decay events with respect to the time of ion implantation yielded a ^{23}Si half-life of 47(1) ms, slightly larger than previously reported [19, 20]. The half-life values were established also for sub-groups of ^{23}Si ions to verify the homogeneous isotopic composition of the ions within the chosen gate as well as among event groups with different decay modes identified. Additionally, the composition of the ion group below the chosen gate was verified by determining the half-life. The results of the fits are presented in Figure 4.11. All the values obtained for events sub-groups are consistent with the result for total statistics. Half-lifes calculated for βp and $\beta 2p$ branches are 46(1) ms and 51(4) ms, respectively. Fit to decay times distribution of events in the upper and lower of sub-groups generated by the passing of the beam through the electrode strips yielded values of 45(2) ms and 47(1) ms, respectively.

The analysis of decay events of the mixture of ^{23}Si and ^{20}Mg resulted in $t_{1/2,mix} = 55(4)$ ms, as visible in Figure 4.11(e). By taking $t_{1/2}(^{23}Si) = 47(1)$ ms (corresponding to an observation probability of 0.89(1)) and the calculated branching ratio for βp $b_{\beta p} = 82(1)\%$, as well as $t_{1/2}(^{20}Mg) = 91$ ms and βp $b_{\beta p} = 27\%$ [2], the amount of ^{23}Si and ^{20}Mg can be determined to be 0.3(1) and 0.7(1), respectively. The resulting expected number of βp emissions observed in this group of events equals 790(120) decays. 825 decays were observed among 2262 ions in the investigated group, which is compatible with the expected amount resulting from the measured $t_{1/2}(mix)$. Performing the same calculations assuming the literature value of $t_{1/2}(^{23}Si) = 42.3(4)$ ms [19] yields an expected number of βp emissions from this ion group of 930(130), also compatible with the observation.

4.3.2 β-delayed p and 2p emission

The analysis of the decay events yielded 5643 cases of βp emission from ^{23}Si, among which 585 were fully stopped in the active volume of the chamber. The rest of the protons escaped the detector. The detected protons' energy deposit spectrum, i.e. for both all protons and only those that left the chamber, is shown and compared with energy deposit simulation results (see Section 4.1) in Figure 4.12.

In Figure 4.13, the energy spectrum of the stopped βp in shown. The spectrum contains five groups of protons that can be identified at energies of about 300, 650, 1250, 1550 and 2050 keV. The

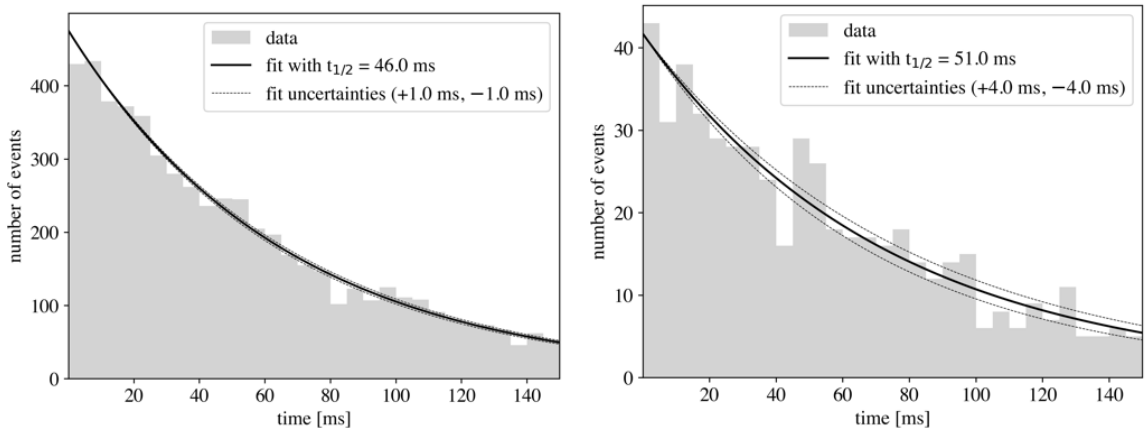

(a) ^{23}Si βp

(b) ^{23}Si β2p

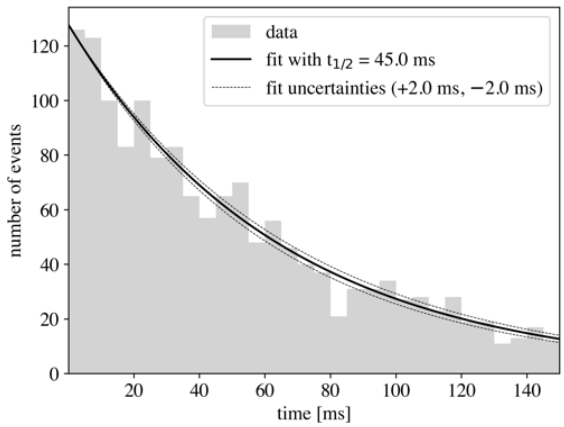

(c) ^{23}Si βp, upper subgroup

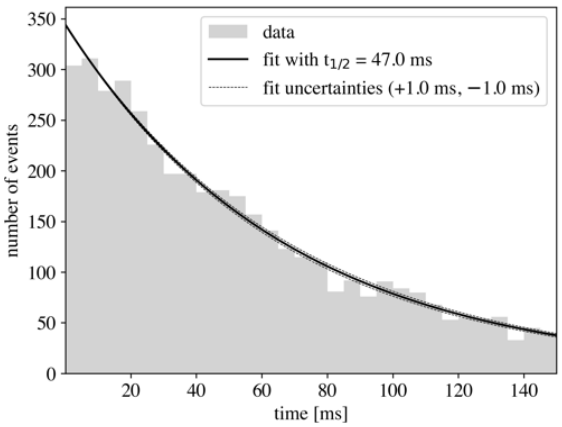

(d) ^{23}Si βp, lower subgroup

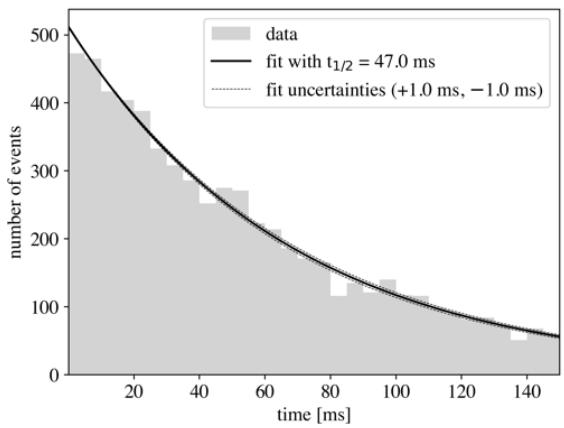

(e) ^{23}Si all

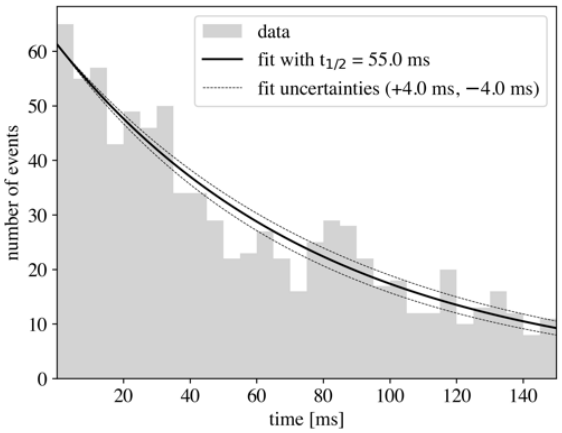

(f) ^{23}Si and ^{20}Mg

Figure 4.11: Distribution of decay times of sub-groups of ^{23}Si events (histograms) and the exponential decay curves, which were determined by the maximum likelihood method using an exponential decay distribution with a finite-time decay observation window for subgroups of events(βp (a); β2p (b); βp & upper subgroup in Figure 3.4(b) (c); βp & lower subgroup in Figure 3.4(b) (d)), for all ^{23}Si decay events (e) and for events with ions forming a group below the chosen ^{23}Si-gate in Figure 3.4(b), which is composed of a mixture of ^{23}Si and ^{20}Mg (f). See text for details.

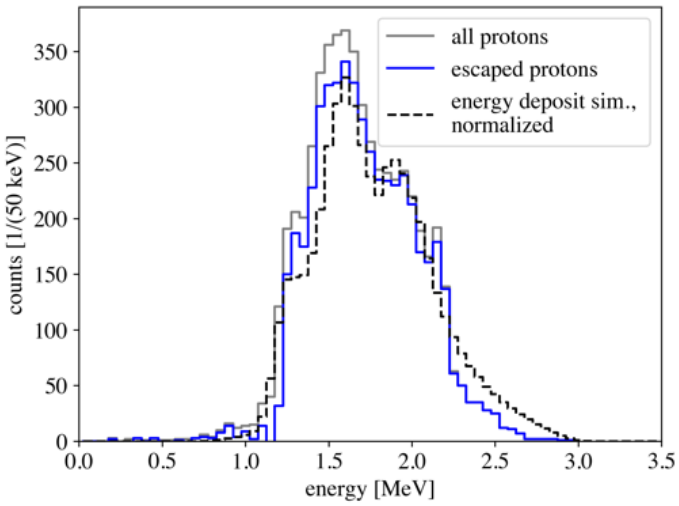

Figure 4.12: Spectrum of energy deposited inside the chamber by all protons (gray), by those protons that exit the detector (blue) and the spectrum obtained by means of the energy-deposit simulation (dashed black line). The results of the simulation accurately reproduce the experimental data. The only meaningul difference between the two occurs at high energies (above 2.2 MeV). This discrepancy might be due to the fact that high-energy protons exhibit faint trajectories, and the low light intensity at the end of the track may lead to underestimating the protons range.

energy intervals corresponding to each group are marked in both spectra. The branching ratios corresponding to the respective portions of spectrum (shown in Figure 4.13) are summarized in Table 4.3.

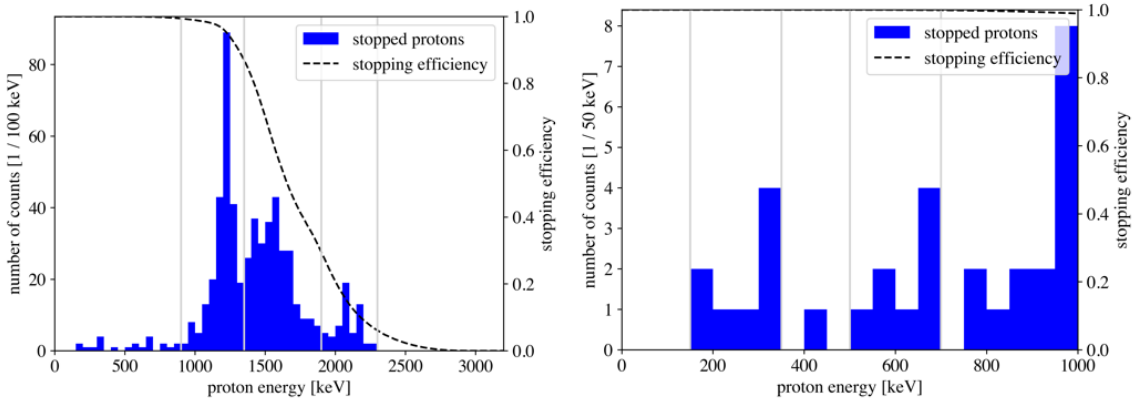

(a) (b)

Figure 4.13: Energy spectra for protons emitted following β decay of ^{23}Si, stopped within the active volume of the OTPC detector presented in (a) full energy range and for (b) energy below 1 MeV. Gray vertical lines mark the energy intervals described in text and summarized in Table 1.3. The dashed black line shows the proton-stopping efficiency as a function of energy.

The group of particles with $E_p \approx 650$ keV lies close to the previously reported proton peak at 600(60) keV [19] (or 673 keV [20]), however its partial branching ratio is much smaller than the values from literature. The group of protons may also be due to several weak transitions. The group around 1250 keV corresponds to the transition at 1320(40) keV [19] (1346(39) keV [20]), which links the 1475 keV $3/2^+$ level in ^{23}Al [53] to the g.s. of ^{22}Mg. The next group, with energy of about 1550 keV corresponds most likely to the peak at 1700(60) keV [19] (1631(46) keV [20]) and might be placed in the level scheme as a transition between the 3166 keV $3/2^+$ level in ^{23}Al [53] and the first excited state in ^{22}Mg with energy 1247 keV as well as to the transition from the 5134 keV $7/2^+$ level in ^{23}Al to the 3308 keV second excited state in ^{22}Mg. The group with the largest energy observed (at 2050 keV) might be due to the low-energy tail of the proton transition at 2400(40) keV [19]

Table 4.3: Observed groups of protons with corresponding number of events with uncertainties [52] and respective partial branching ratios, compared with previously reported values of peaks energies and branching ratios [19,20]. The number of events corresponds to the integral of the regions marked in Figure 4.13. The values include the bin-by-bin correction for the stopping efficiency.

This experiment			Previous studies			
E_p [keV]	events	b [%]	E_p [keV]		b [%]	
			[19]	[20]	[19]	[20]
300	8^{+4}_{-3}	$0.12^{+0.06}_{-0.04}$	–	–	–	–
650	8^{+4}_{-3}	$0.12^{+0.06}_{-0.04}$	600(60)	673(36)	< 3	2.4(1)
1250	230 ± 16	3.6 ± 0.2	1320(40)	1346(39)	10(1)	5.1(4)
1550	200 ± 15	4.6 ± 0.3	1700(60)	1631(46)	< 5	4.6(6)
2050	52 ± 8	4.4 ± 0.7	2400(40)	2309(41)	32(2)	21(2)

(2309(41) keV [20]), with a lower branching ratio than previously reported, as this proton transition lies at the edge of the detector's proton-stopping ability. The lowest energy proton group around 300 keV was observed in these studies for the first time. It might be due to several weak transitions, and, unfortunately, cannot be placed in the level scheme. Figure 4.14 shows the partial decay scheme of ^{23}Si with the observed and assigned transitions. Possible transitions involved in β2p emission from ^{23}Si, as described in the following, are also shown.

Examples of βp and β2p emission events are presented in Figure 4.15.

Among the correctly implanted ^{23}Si ions, 533 decayed via β2p emission (an example event containing two protons stopped inside the detector is shown in Figure 4.15c). In 22 of these decay events, both protons stopped inside the active volume of the detector, yielding the possibility to calculate their total energies. For 240 among the remaining events, the calculation of the partial energy deposited in the detector was possible, as the endpoints of the trajectories were clearly identified and the ratios $light_{CCD}$ and $light_{PMT}$ allowed for correlating the trajectories in the CCD picture and in the PMT data with each other. This was possible because the linear relationship between $light_{CCD}$ and $light_{PMT}$ was verified.

The spectrum of the sum energy of the two protons (E_{sum}) in events in which both protons were stopped inside the chamber as well as of the partial energy for those events in which one or two protons escaped are shown in Figure 4.16. Limited statistics and level density prevent observation of any peak structure. Nevertheless the shape of the spectrum indicates decay by emission of 2 protons from levels at excitation energies 6.5-9 MeV in ^{23}Al, providing new information on the structure of this nucleus above S_{2p}. The group of events above 2 MeV and centred around 2.7 MeV in Figure 4.16(a) could originate from feeding in β decay of a broad level or several ones at excitation energy around 8.6 MeV in ^{23}Al.

The energy seems to be shared between the two stopped protons rather equally, see Figure 4.17, hence the single protons energies in the group described are in range of 1-1.5 MeV. Assuming GT decay of the ^{23}Si $5/2^+$ ground state, one might expect feeding of $3/2^+$, $5/2^+$ and $7/2^+$ levels in ^{23}Al. This is followed by proton emission to low-spin states in ^{22}Mg at around $E_x = 7$ MeV and sequential emission of another proton to the $3/2^+$ ^{21}Na ground state, if emission of low-ℓ protons is considered. These possible transitions are shown in the partial scheme of ^{23}Si decay in Figure 4.14. It is important to note that the data presented in Figure 4.16(a) are biased due to the rapid decrease in the single-proton stopping efficiency at approximately 1.5 MeV energy, as illustrated in Figure 4.6.

The energy spectrum deposited inside the detector in events in which at least one proton escaped (Figure 4.16(b)) stretches between 2 and 4 MeV, with a maximum around 3 MeV, which corresponds

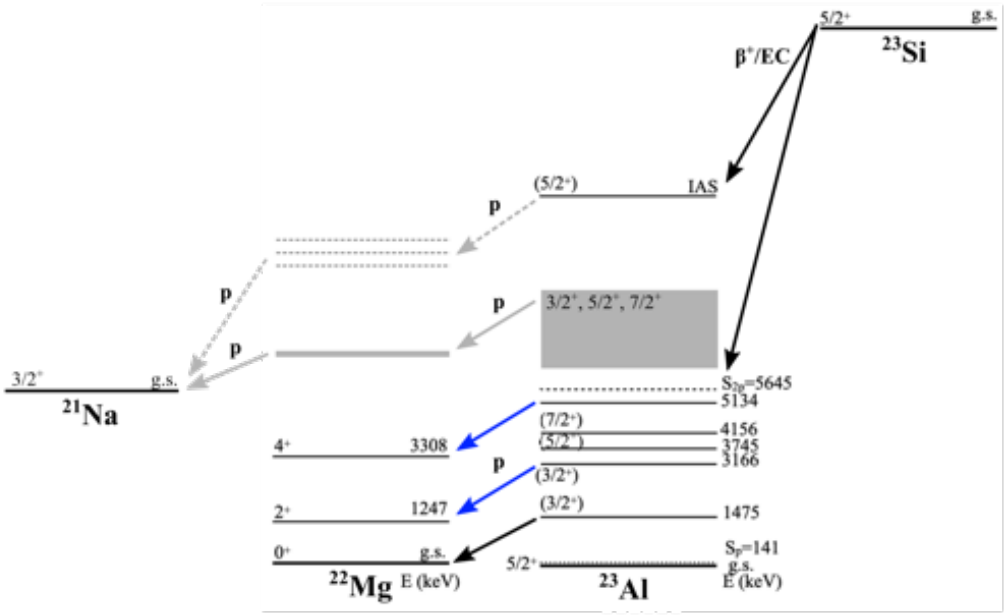

Figure 4.14: Partial decay scheme of ^{23}Si decay. All known levels in ^{23}Al fed in β decay [53] and levels in ^{22}Mg populated by ^{23}Si βp decay are marked with black lines. Arrows mark proton transitions that could be placed in the scheme. The black arrow marks the transition observed at 1250 keV, corresponding to 1320(40) keV [19] / 1346(39) keV [20]. Blue arrows mark two possible transitions corresponding to the peak observed around 1550 keV, reported at 1700(60) keV [19] / 1631(46) keV [20]. Gray arrows depict a possible approximate placement of transitions involved in β2p emission. Solid gray arrows correspond to the transition (or group of transitions) resulting from the spectrum of E_{sum} of β2p events where both protons were stopped (see Figure 4.16(a)), whereas dashed gray arrows show possible, yet not observed due to too high energy, decay via two sequential proton emissions after feeding the IAS in ^{23}Al. See text for details.

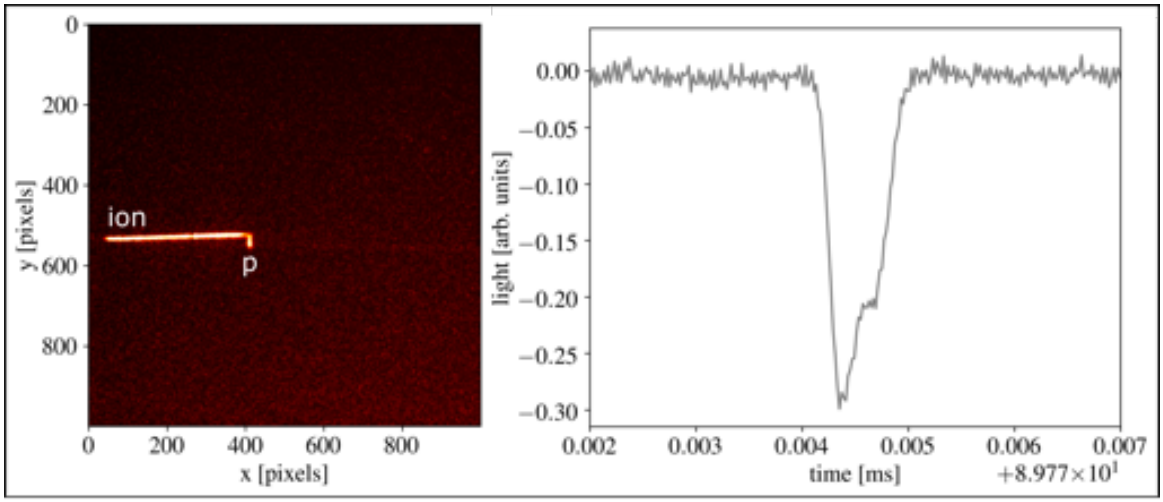

(a)

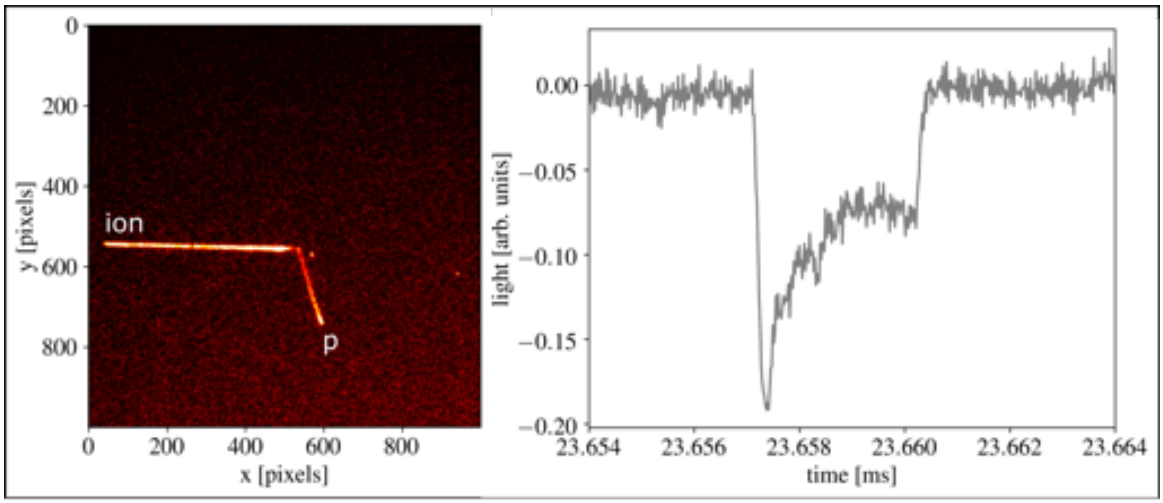

(b)

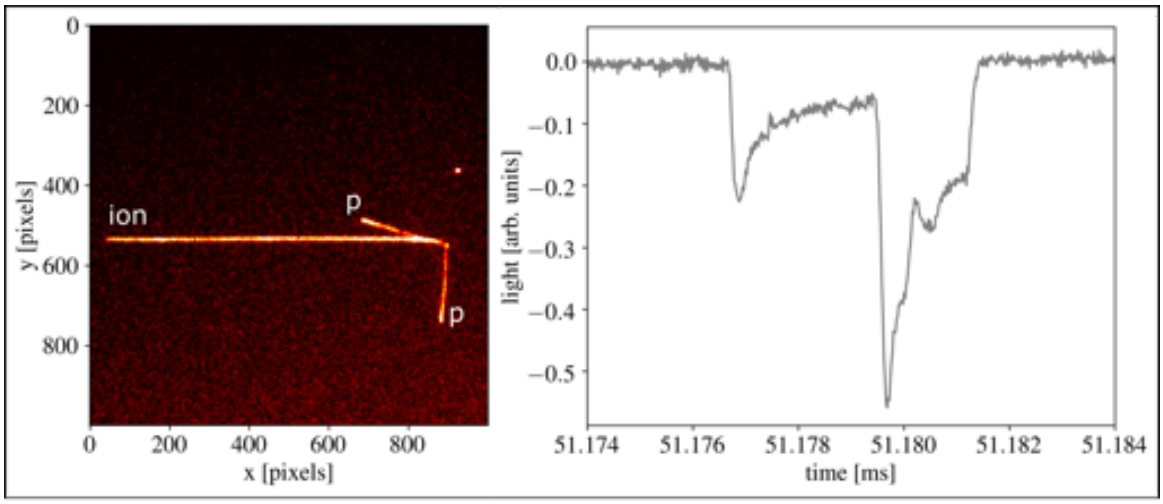

(c)

Figure 4.15: Example data from CCD (left) and PMT (right) for events with βp emission ((a) and (b)), and β2p emission (c) from ^{23}Si. The PMT data are shown around the time of the proton signal. Subfigure (a) shows a proton with energy 0.34(6) keV originating from the lowest-energy proton group in Figure 4.13. The proton visible in subfigure (b) has energy 1.24(4) keV and therefore belongs to the third group of protons in Table 4.3. Both protons visible in (c) were completely stopped inside the detector: two Bragg curve shapes ending with Bragg peaks are visible in the PMT and CCD data.

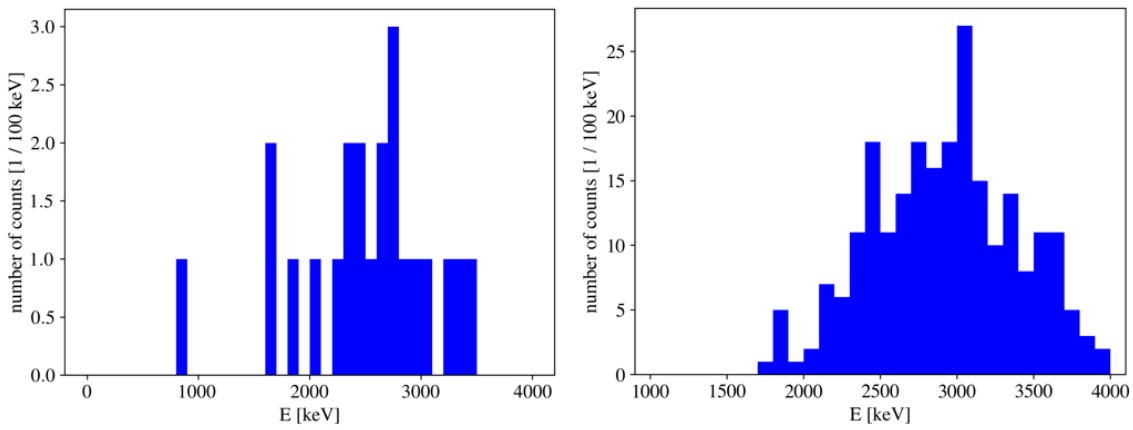

(a) (b)

Figure 4.16: Sum-energy spectra of β2p emission events in which (a) both protons stopped in the active volume of the OTPC detector and (b) at least one proton left the chamber. See text for details.

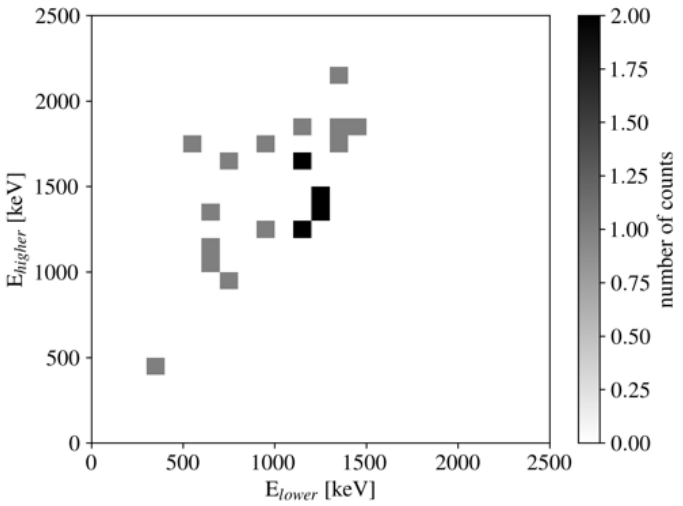

Figure 4.17: Single proton energies from β2p events in which both particles were stopped, thus corresponding to the E_{sum} spectrum in Figure 4.16(a). The energy of the higher-energy proton (E_{higher}) is plotted as a function of that of the lower-energy proton (E_{lower}).

to roughly double the energy of the most intense peak in energy deposit simulated for single escaping protons (see Figure 4.7(b)). These are protons leaving the chamber through side walls.

The distribution of opening angles between the two protons are shown in Figure 4.18. Due to limited statistics it is not possible to establish the exact decay path and hence the decay mechanism. Nevertheless the opening angle distribution presented in Figure 4.18(a), i.e. for events in which both protons stopped, seems to be centered symmetricaly around 90°, which indicates uncorrelated sequential two-proton emission rather than simultaneous/diproton. The opening angle distribution of the group of events in which at least one of the protons escaped, see Figure 4.18(b), shows compliance with sinusoidal shape characteristic for uncorrelated sequential two-proton emission, indicating that this is most likely the main decay mechanism at play.

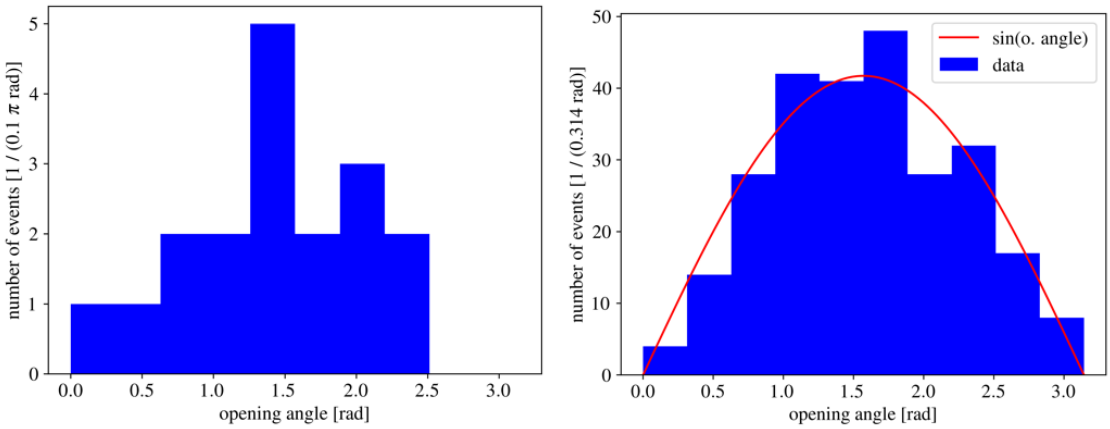

(a) (b)

Figure 4.18: Opening angle distribution in group of events in which (a) both protons were stopped and (b) at least one particle escaped the chamber. Even though at least one particle escaped the chamber, it was possible to determine the angle between them. The distribution (a) appears to be centred symmetrically and suggests that the decay occurs via uncorrelated sequential two-proton emission. The second distribution shape is well described by a sine distribution, which is characteristic for the same decay mechanism.

4.3.3 β-delayed 3p emission

The first newly discovered decay channel involves the emission of three β-delayed protons. This decay mode was identified on the basis of only two events, highlighting the sensitivity of the OTPC detector in detecting exotic decay channels even with very limited statistics. The CCD images that clearly show the presence of three emitted protons, as well as respective PMT signals, for both events, are shown in Figure 4.19.

In the first event (Figure 4.19(a)) all protons were stopped within the active volume of the detector. Consequently, both the CCD image and the PMT signal show three distinct Bragg peaks. All three trajectories start at ≈ 7.5 μs. One proton is emitted downwards, which is indicated by the position of its Bragg peak at $t = 7.1$ μs, while the other two particles are emitted upwards, with their trajectory endpoints at $t = 7.9$ μs and $t = 8.1$ μs, respectively. Although it is not possible to assign unambiguously the PMT signals to the tracks visible in the CCD image, calculations of the energies for potential pairs of CCD and PMT trajectories allowed for the determination of the average total energy of the three emitted protons to be $E_{sum} = 3.65(35)$ MeV, for all 6 combinations.

In the second event (Figure 4.19b), all protons escaped from the chamber – one through the wall opposite to the entrance window and the other two (two short tracks visible on CCD image in Figure 4.19(b)) through the upper/bottom walls. As a result, the PMT signal does not show any Bragg peak. The portion of the signal at later times corresponds to the proton emitted forward and almost horizontally. Since the protons escape, only a lower limit on their total energy could be calculated. Depending on the assignment of trajectory pairs, the energy E_{sum} ranges from

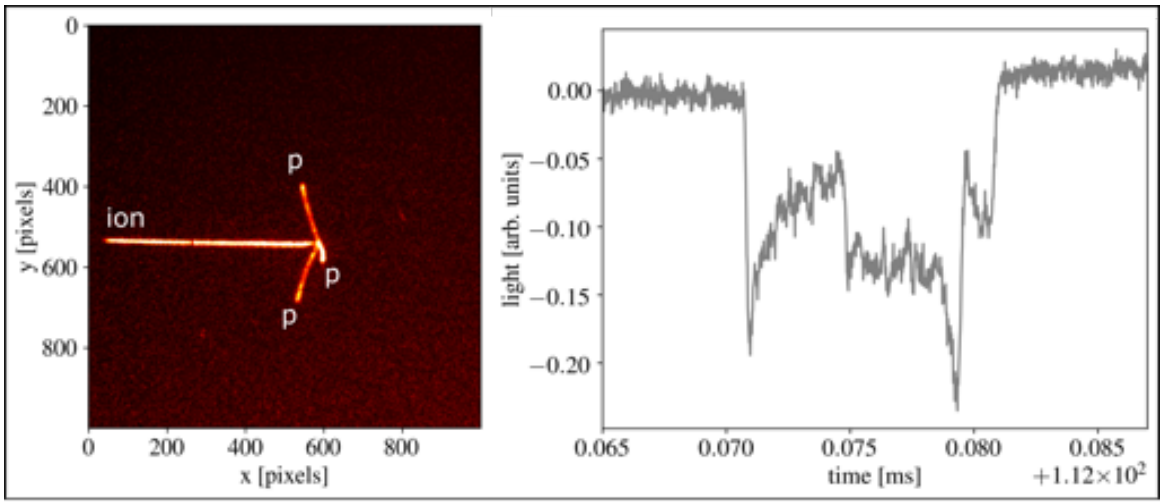

(a)

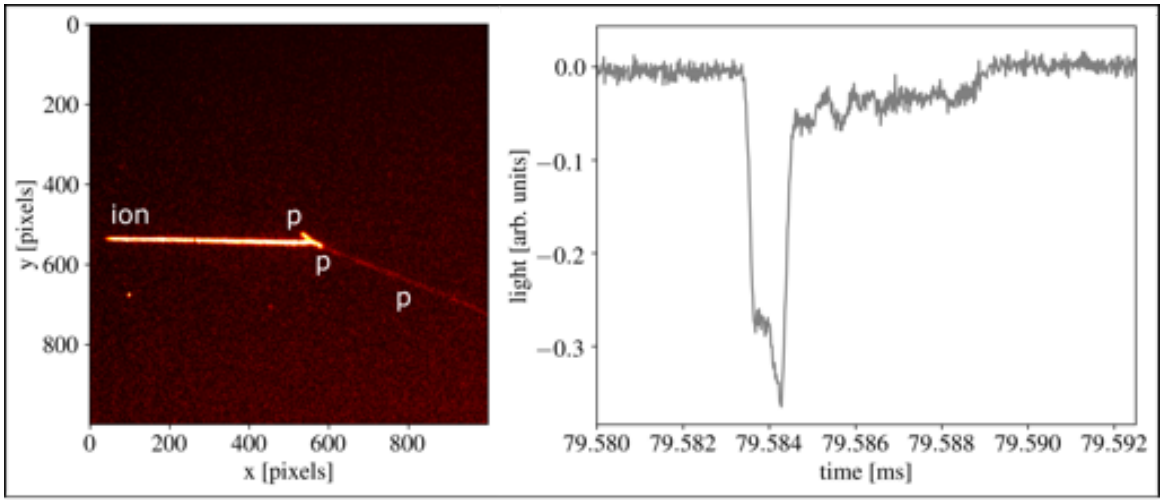

(b)

Figure 4.19: The two events with β3p emission from ^{23}Si recorded on CCD images (left) and PMT signals (right). On the CCD images both the implanted ion as well as three emitted protons are visible, whereas the PMT signal is zoomed around the proton trajectories. All protons in the first event (a) were stopped inside the chamber while in the second event (b) all particles left the detector. See text for details.

2.7(7) MeV to 3.3(6) MeV. The former event is consistent with the decay of the isomeric state in ^{23}Al, while the latter event might also originate from the IAS, although it remains uncertain.

The calculated branching ratio, $b_{\beta 3p} = 2.9(^{+38}_{-19}) \times 10^{-4}$ may be compared with values for others $T_z = -5/2$ isotopes, among which two, ^{31}Ar and ^{43}Cr, were observed to decay via this channel [45,54] and for the missing member of the $T_z = -5/2$ sequence, ^{27}S, an upper limit was established [55]. The value obtained for ^{23}Si is close to those for ^{31}Ar and ^{43}Cr, as shown in Table 4.4. The only other remaining β3p emitter known to date is ^{45}Fe [41], more exotic and hence characterized by larger branching ratio.

Table 4.4: Comparison of the branching ratio $b_{\beta 3p}$ determined for ^{23}Si with values from literature for all other known β3p emitters. The values for the isotopes with $T_z = -5/2$ (^{27}S [55], ^{31}Ar [45] and ^{43}Cr [54]) are all of order of 10^{-4} and the value obtained for ^{23}Si fits this trend. The only other known case of β3p, ^{45}Fe, has $T_z = -7/2$ and larger $b_{\beta 3p} = 3.3(16) \times 10^{-2}$ [41].

isotope	T_z	branching ratio $b_{\beta 3p}$
^{23}Si	$-5/2$	$2.9(^{+38}_{-19}) \times 10^{-4}$ (this work)
^{27}S	$-5/2$	$\leq 1 \times 10^{-3}$ [55]
^{31}Ar	$-5/2$	$7(2) \times 10^{-4}$ [45]
^{43}Cr	$-5/2$	$13(^{+18}_{-8}) \times 10^{-4}$ [54]
^{45}Fe	$-7/2$	$3.3(16) \times 10^{-2}$ [41]

4.3.4 β-delayed αp/pα emission

As the energy window open for $\beta\alpha$p/βpα in ^{23}Si is of similar size as the one for β3p emission, it was reasonable to consider if also such a decay can be identified. Due to differences in energy losses along the trajectory of α particles and protons (see Figure 4.20) and the α particles' shorter range (for the same energy), the search was restricted to events containing two particles among which one was brighter and shorter in both CCD and PMT. The assignment was made on basis of the ratio of total light of both components of the trajectories $light_{CCD}/light_{PMT}$.

The analysis yielded the selection of one candidate event (shown in Figure 4.21) to which PMT signal fitting was performed, assuming two possible scenarios: that both tracks are due to protons and that the shorter and brighter one comes from an α particle. The results of the fitting are shown in Figure 4.22. Due to the limitations described in Section 4.1, in particular with respect to the signal/noise ratio, the difference in residual r^2 values for both scenarios is not big ($r^2 = 0.4$ and $r^2 = 0.6$ for $\alpha+p$ and $p+p$ cases, respectively), but the curve for the $\alpha+p$ scenario reproduces better the shape of the signal. The event was therefore tentatively recognized as the emission of β-delayed proton and α particle. The energies of the two particles resulting from fit are $E_p = 1.6(1)$ MeV and $E_\alpha = 1.2(4)$ MeV, which is compatible with possible emission from the IAS in ^{23}Al. For comparison, the energies for $p + p$ scenario are $E_{p1} = 1.6(1)$ MeV and $E_{p2} = 0.4(2)$ MeV.

It still remains to be considered, in which order the two particles are emitted, under the assumption of the sequential emission. Two scenarios are possible, as shown in Figure 4.23 and described in the following.

1. Assuming the α particle to be emitted first with $\ell = 0$ to the ground-state of ^{19}Na, which is proton-unbound, followed promptly by the emission of an $\ell = 2$ proton, these particles would have energies of 3.1 and 0.3 MeV, respectively [4]. Another option would be the decay via an excited state in ^{19}Na. Nevertheless, the only candidates known for $5/2^+$ states in ^{19}Na have energy of $\approx 2.5\ MeV$ [2] and this would implicate an energy for the α particle of only 0.6 MeV, which is incompatible with the result obtained here and means that its emission would be suppressed by the Coulomb barrier. Consideration of higher-ℓ α transition seems unjustified

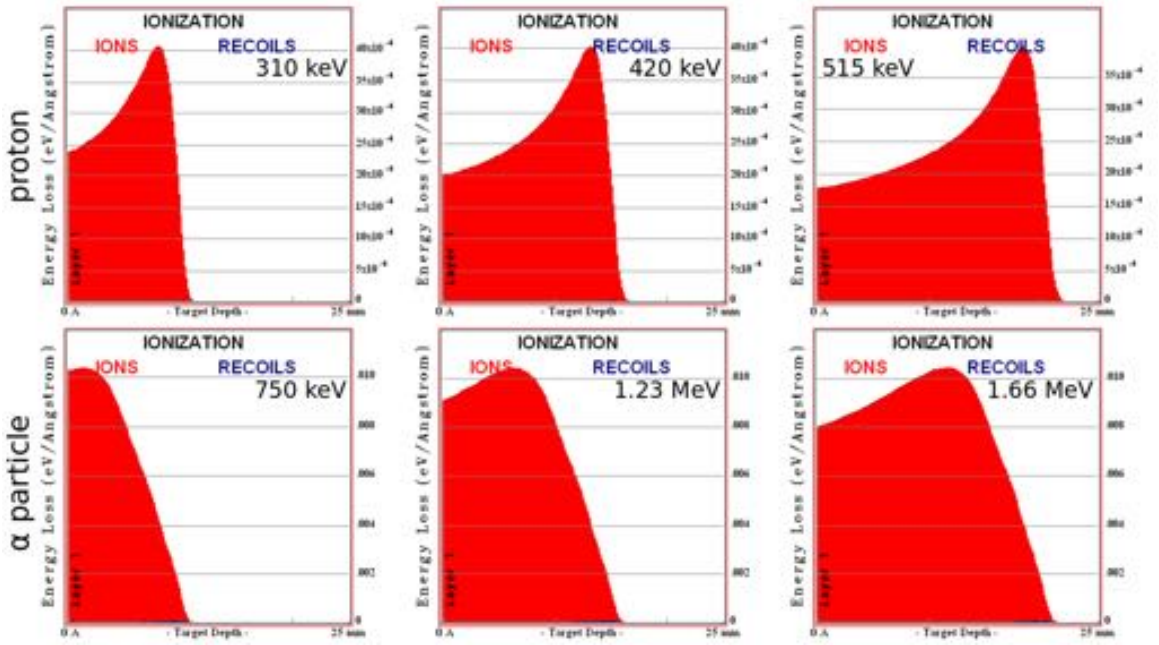

Figure 4.20: Energy losses dE/dx for protons (upper subfigures) and α particles (bottom subfigures) with approximate ranges of 10 cm (left), 15 cm (middle) and 20 cm (right) in the gas mixture used in experiment, simulated with SRIM software [40]. The corresponding energies of particles are reported on the respective subfigures. As expected, α particles are characterized by higher energy losses (1×10^{-2} eV/Å versus 4×10^{-3} eV/Å for proton in the Bragg peak) as well as different shape along the trajectory, with less prominent Bragg peak and more gradual decline at the end of the trajectory. These differences enable the distinction between protons and α particles.

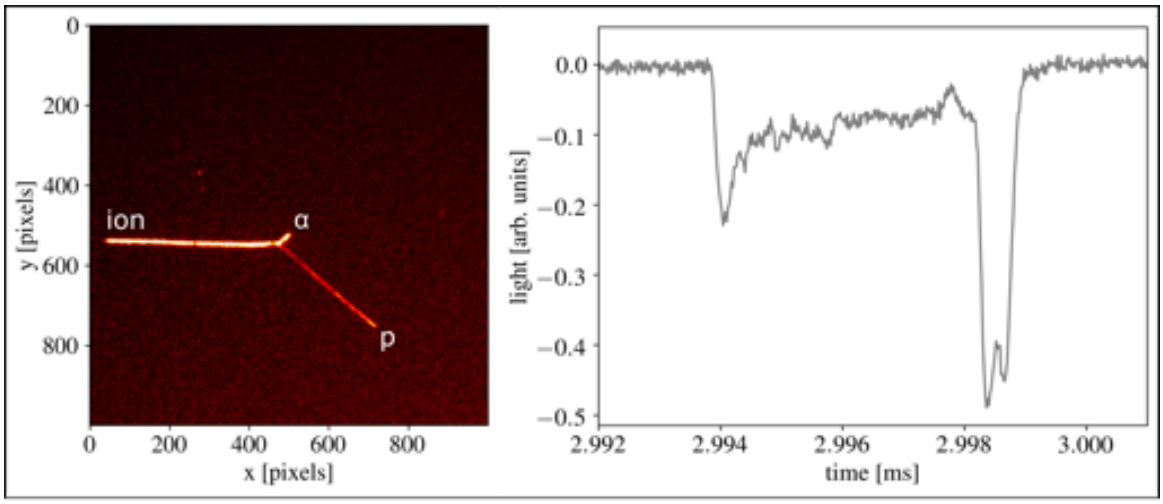

Figure 4.21: The image recorded by the CCD camera (left) and the corresponding PMT signal around the time of the decay (right) for the event tentatively assigned to the $\beta\alpha$p/βpα decay channel. It was determined on basis of the integrals of light of CCD and PMT components, that the shorter and brighter trajectory in the CCD picture matches the left (shorter and more intense) part of the PMT signal and both particles were emitted downwards. See text for details.

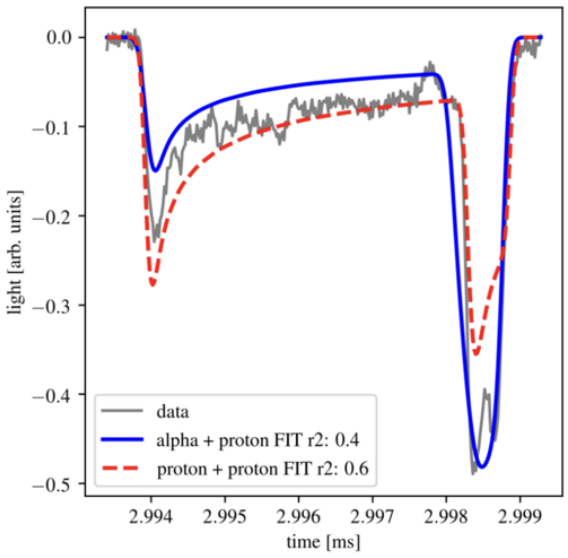

Figure 4.22: PMT signal recorded for the event tentatively assigned to the $\beta\alpha$p/βpα decay channel with fit results assuming two scenarios: $\beta\alpha$p/βpα (blue) and $\beta 2p$ emission (red). See text for details.

because of the much lower barrier penetrability due to both larger angular momentum and lower energy.

2. Supposing the opposite scenario, a proton emitted from the IAS in ^{23}Al could feed a highly excited ($\approx$ 10.4 MeV) state in ^{22}Mg followed by the α emission to the g.s. in ^{18}Ne. This should involve particles with minimum angular momentum, due to the barrier-penetrability dependence on ℓ and energy. There are indeed several excited low-spin levels known in ^{22}Mg at $E_x = 10 - 11$ MeV known from transfer reaction studies [2] – including ^{18}Ne(α,p)^{21}Na, the indirect process to βp emission to the same level in ^{22}Mg [56]) – that could participate in the β-delayed $\ell = 1$ p and $\ell = 0$ α emission with energies consistent with the results obtained here.

These considerations show that the recorded event occured most probably according to the latter scenario, while the first one is still possible, but less likely, and therefore might require higher statistics to be detected.

In the previously known cases of $\beta\alpha$p/βpα emission, i.e. ^{9}C [57], ^{17}Ne [58], and ^{21}Mg [59], the mother nuclei had $T_z = -3/2$, and the decay proceeded through an α-conjugate nucleus, ^{8}Be, ^{16}O, and ^{20}Ne, respectively. Both decay sequences were observed in ^{17}Ne, with $b_{\beta\alpha p+\beta p\alpha} = 1.6(4) \times 10^{-4}$ and in ^{9}C. The latter is a special case, since all states populated in β decay in its daughter ^{9}B break up into a proton and two α particles [57], which might be interpreted as $b_{\beta\alpha p+\beta p\alpha} = 100\%$, but is not a typical case of this decay mode [36, 37]. In the case of ^{21}Mg, only βpα emission was observed, with a branching ratio of $b_{\beta p\alpha} = 1.6(3)10 \times 10^{-4}$ [59]. ^{13}O, the missing member of the $T_z = -3/2$ sequence, was predicted to decay via this mode with branching ratio $b_{\beta p\alpha} = 0.9(3) \times 10^{-4}$ [59]. It was recently reported to be the first known $\beta 3\alpha$p emitter, with a branching ratio of $7.8(6) \times 10^{-4}$ [60]. The result of $b_{\beta p\alpha} = 1.4(^{+33}_{-12}) \times 10^{-4}$ for ^{23}Si closely aligns with the previously reported branching ratios. Figure 4.24 presents the branching ratios for both exotic decay channels, $\beta p\alpha/\beta\alpha p$ and $\beta 3p$, for all known emitters with different T_z values.

The systematics of $\beta\alpha$p/βpα decays from $T_z \leq -3/2$ was discussed by Lund *et al.* in Ref. [59]. They concluded that the presence of these exotic decay modes is most of all influenced by odd-even effects on the decay energy, rather than the structural effects like α-clustering, despite the final-state nuclei being α-conjugate. They proposed that the observation of this exotic decay mode in heavier nuclei with lower T_z, such as ^{23}Si, ^{27}S, and ^{31}Ar would provide an opportunity to test their interpretation. The discovery of this branch in ^{23}Si with $T_z = -5/2$, with a comparable branching ratio as for nuclei with $T_z = -3/2$, supports their conclusions regarding the influence of odd-even effects on the occurrence of this exotic decay mode.

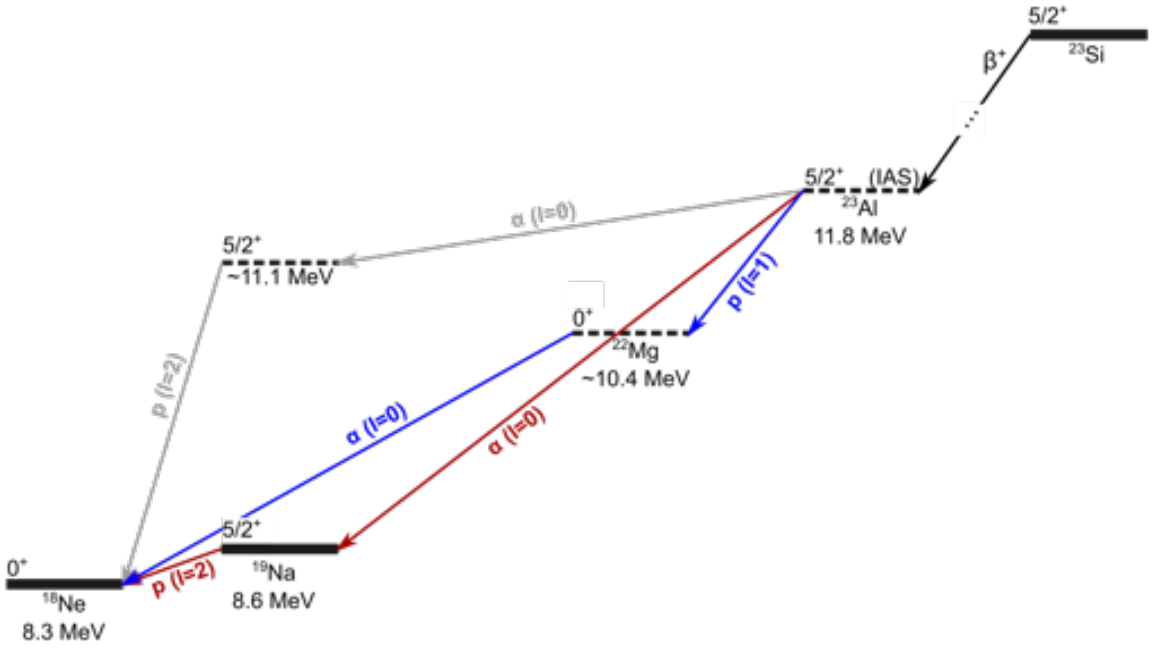

Figure 4.23: Schematic illustration of the two scenarios for $\beta\alpha$p/βpα emission. In the first scenario an α particle is emitted from the IAS in ^{23}Al to the ground state (or to an excited state, which is less probable as no suitable states are known) in ^{19}Na, followed by the proton emission to g.s. in ^{18}Ne (red and gray arrows, for decay via g.s. and excited state in ^{19}Na, respectively). In the second scenario (blue arrows), a proton is emitted from IAS in ^{23}Al to an excited state with $E_x \approx 10.4$ MeV in ^{22}Mg, and sequentially an α particle is emitted to the g.s. in ^{18}Ne. See text for details.

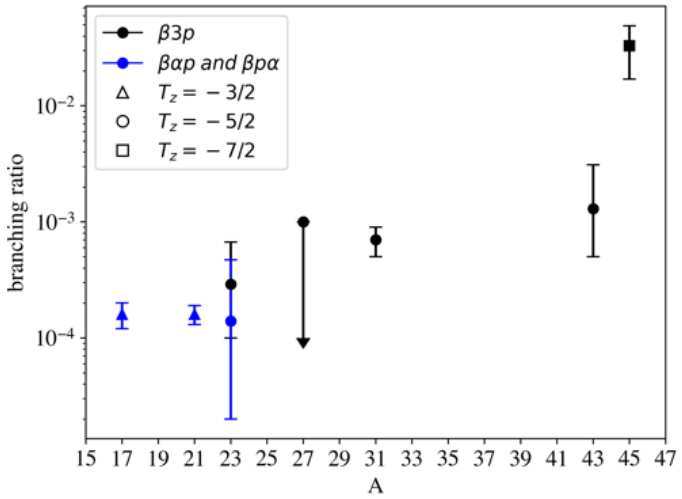

Figure 4.24: Branching ratio values for all known $\beta\alpha$p/βpα (blue) and $\beta 3p$ (black) emitters with $T_z = -3/2$ (triangles): ^{17}Ne [58] and ^{21}Mg [59]; $T_z = -5/2$ (circles): ^{23}Si (this work), ^{31}Ar [45], ^{43}Cr [54], as well as upper limit for ^{27}S [55]; and $T_z = -7/2$ (square): ^{45}Fe [41]. The special case of ^{9}C is not included here, as well as ^{13}O, see text. The branching ratio for βpα decay mode in ^{23}Si with $T_z = -5/2$ is comparable to the results for nuclei with $T_z = -3/2$. The plot shows also a clear increasing trend in branching ratios for exotic decay channels probabilities with decreasing negative T_z values.

4.4 Validation of theoretical calculations

Previous studies have already investigated the β decay of ^{23}Si using the state-of-the-art shell-model (SM) approach, which demonstrated to accurately describe the low-energy spectrum of ^{23}Al [19]. In the present study, an alternative approach was chosen, employing multi-reference density-functional-rooted No-Core Configuration-Interaction Model (DFT-NCCI) calculations performed by prof. Wojciech Satuła [61]. DFT-NCCI is a post-Hartree-Fock (HF) configuration-interaction. It restores symmetries violated by HF solutions (angular momentum and isospin symmetry) by mixing good symmetry states projected from different mean-field configurations. For the purpose of these studies, two variants of the model were used. First, the more advanced variant, treats properly the isospin symmetry and restores angular momentum. The configuration space chosen consisted of the g.s. and the two lowest particle-hole configurations in ^{23}Si as well as the g.s. and 13 excited configurations in ^{23}Al space. It was selected to allow for obtaining relatively well-converged solutions for the g.s. of ^{23}Si and ^{23}Al, the low-lying (below 3.5 MeV) excited states in ^{23}Al and the IAS in ^{23}Al. In the second variant, only the angular momentum projection is performed, which makes this variant less computationally demanding and thus allows to include more configurations.

The DFT-NCCI model belongs to a class of so-called global models. As such, it cannot compete with SM, which is fine-tuned to the valence space, but it is applicable to predicting the properties of a broad range of nuclei. Thus, the purpose of performing the DFT-NCCI calculations was not to improve the theoretical description of ^{23}Al, but rather to validate the new approach in a nucleus where benchmark SM results already exist. Additionally, it allowed to test the properties of the underlying functional in this mass region without any local fine-tuning of functional's parameters.

The calculated binding energies for the ground states of ^{23}Si and ^{23}Al are 158.2 MeV and 172.7 MeV, respectively, slightly larger than the experimental values [4]. The calculations yielded also the energies of the excited states, the spectrum of which is presented in Figure 4.25 and which compares relatively well with the shell-model (SM) results at low energies [19]. The calculated excitation energy of 9.27 MeV for the IAS in ^{23}Al is lower than the experimental value of 11.78 MeV [19].

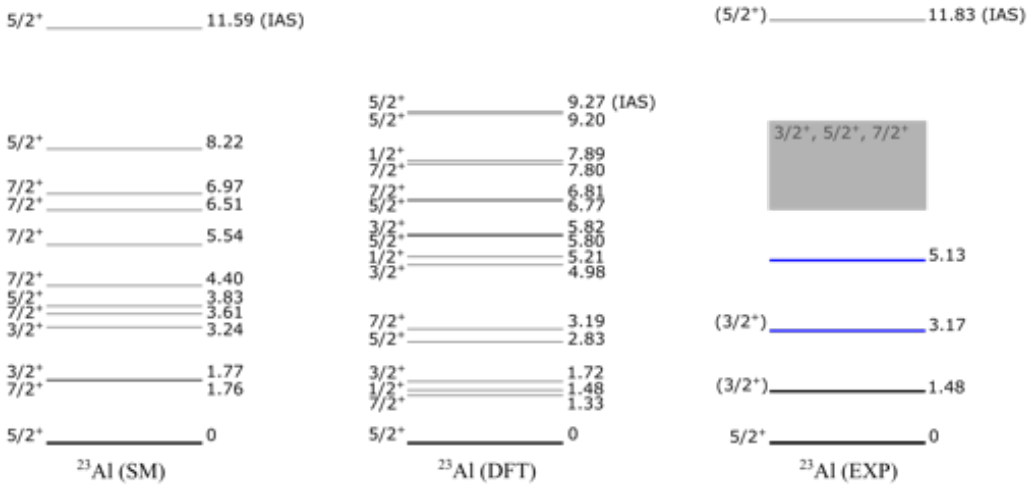

Figure 4.25: Level energies resulting from SM [19] and DFT-NCCI [62] calculations, as well as experimentally known levels in ^{23}Si, which involvement in the β decay of ^{23}Si was observed within this study: the 1475 keV level corresponding to the transition observed at 1250 keV (black), and 3166 keV and 5134 keV levels that may correspond to the peak observed at 1550 keV (blue), see also Figure 4.14. The proton transitions involving IAS were not observed due high energy of the proton emitted combined with the stopping-efficiency limitation. The fact that around 90% of the detected protons were not stopped inside the chamber due to their high energy is consistent with the theoretical predictions of IAS feeding dominating the decay. The gray rectangle marks the possible levels participating in β-delayed 2p emission (see Section 4.3.2) that could correspond to the calculated levels, especially 6.77 MeV $5/2^+$, 6.81 MeV $7/2^+$ and 7.80 MeV $7/2^+$.

The level that is most fed in ^{23}Si β decay is the IAS, with matrix elements $|M_F| \approx \sqrt{4.9}$ and $|M_{GT}| \approx 1.5$ for Fermi and Gamow-Teller decays, respectively. Decay to lower states is expected to be hindered due to the shape difference between weakly deformed oblate ^{23}Si, with calculated mean quadrupole deformation parameters $\beta_2 = 0.090$ and $\gamma = 60°$, and well-deformed prolate ^{23}Al ($\beta_2 = 0.345$ and $\gamma = 0°$). The lowest particle-hole excitations in ^{23}Al were also found to be well-deformed. The largest GT matrix elements within the selected configuration space are to the $I^\pi = 5/2^+$ and $7/2^+$ states at excitation energies of 5.8 MeV and 7.8 MeV, respectively. The matrix elements to other (especially lower) states, are significantly below unity. The IAS excitation energy is underestimated, which suggests a need for improved calibration of the symmetry energy strength in the used functional.

The stability of the low-energy spectra calculations was verified by angular-momentum-projected calculations, i.e. the second variant of the model. The details of the calculations performed with both variants and the results are given in Ref. [62] and its supplemental material.

Chapter 5

Neutron-deficient Ge and Zn isotopes

5.1 Data analysis

5.1.1 Selection of the ions of interest

The identification of the ions of interest was performed online on the basis of ΔE and two independent ToF measurements, as described in Section 3.2. Id-plots containing all ions entering the detection setup and only the triggering ones were presented in Figure 3.7. Hardware gates were imposed to allow only triggering of the DAQ2 by germanium and a limited amount of zinc ions. Offline, software gates were imposed to select those events that were considered in further stages of the analysis, especially while looking for the decay events. Figure 5.1 shows the selection of the ions of interest in the ^{60}Ge setting. The corresponding plot for ^{59}Ge setting will be presented in Section 5.2.1.

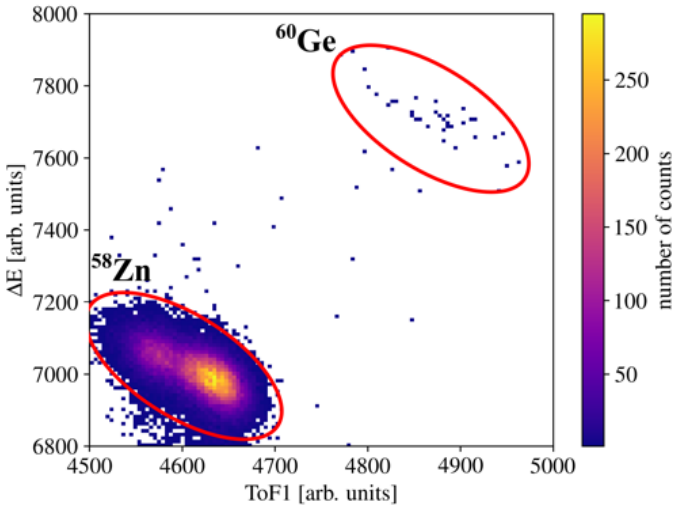

Figure 5.1: Identification plot with ions triggering the DAQ2 in the ^{60}Ge setting of ion optics. Red ellipses mark the regions of the software gates set for ^{60}Ge and ^{58}Zn ions, see text.

5.1.2 Drift velocity

During the whole experiment, a drift velocity detector (described in detail in Section 2.2.3) was used to monitor the v_{drift} of electrons in the gas mixture measurements every 1-2 hours. The meteorological conditions throughout the experiment were also monitored and found to be stable with pressure $P = 986(8)$ hPa and temperature $T = 25.5(2)$°C. Therefore it was possible to use one drift velocity value for the analysis of whole data set, which was determined to be 10.5(2) mm/μs.

5.1.3 Drift of the ions in the gas and its influence on the observation probability and stopping efficiency

The ions implanted into the active volume of the detector did not fully neutralize and therefore drifted in the gas in the opposite direction than the electrons, towards the cathode. This phenomenon was evidenced by two facts:

1. Analysis of the observed decay events clearly showed that most of the protons were emitted downwards as detailed later.
2. Just after the detection of each ion a period of about 20 ms during which significantly increased noise in the PMT signals could be observed (see Figure 5.2).

The origin of the larger noise resulted to be the electrons emitted in the gas ionisation caused by ion drifting through it before stopping at the cathode [1] The duration of these signals allowed to estimate the time of drift to be $t_{drift} = 20(5)$ ms. During this time, the OTPC detector was sensitive to protons emitted in the full solid angle. Afterwards, for the rest of the observation window, this sensitivity dropped by 50%, since only protons emitted downwards could be detected.

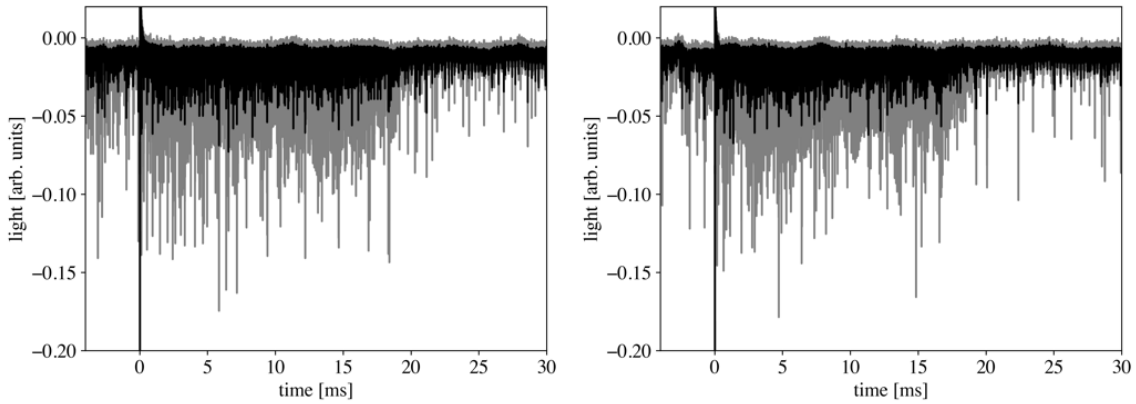

Figure 5.2: Two examples of portions of PMT signals just after the ion implantation at t = 0 ms. The data for t between 0 and around 20 ms show increased noise level, which is caused by the electrons emitted in the gas while the non fully-neutralized ion drifts towards the cathode. The gray line corresponds to the raw data, while the black line to data with a median filter applied with a window of 5 samples.

The ions drift affected the total probability of recording an emitted proton during the observation window. This probability is therefore given by the sum of two integrals

$$\frac{1}{\tau}\left(\int_{t_i}^{t_{drift}} e^{-t/\tau}dt + \frac{1}{2}\int_{t_{drift}}^{t_f} e^{-t/\tau}dt\right) \tag{5.1}$$

where t_i and t_f are the beginning and the end of the observation window, respectively, t_{drift} corresponds to the time of the ions drift towards the cathode and τ is the lifetime of the isotope the decay of which has to be recorded. The resulting probabilities were found to be around 60% for ^{60}Ge, with the exact value depending on the half-life taken into account, e.g. 60(4)% for $t_{1/2} = 34.6$ ms [63], 64(4)% for $t_{1/2} = 29$ ms [64,65], see Section 5.3 for details, and 35(2)% for ^{58}Zn ($t_{1/2} = 86(2)$ ms [33]).

The ions drift was taken into account while performing the proton stopping efficiency simulations. Apart from this, the procedure consisted of the same steps as those described in Section 4.1.2. The only difference was the time dependence of the proton emission point. For this reason, the simulation in this case already included the proton observation probability given by Equation 5.1. The implantation profile along the beam axis for ^{58}Zn in shown in Figure 5.3, whereas the expected distributions resulting from LISE++ simulations [50] are reported in Figure 5.4.

[1] Ion-drifting times are typically 3-4 orders of magnitude slower than electron-drifting time.

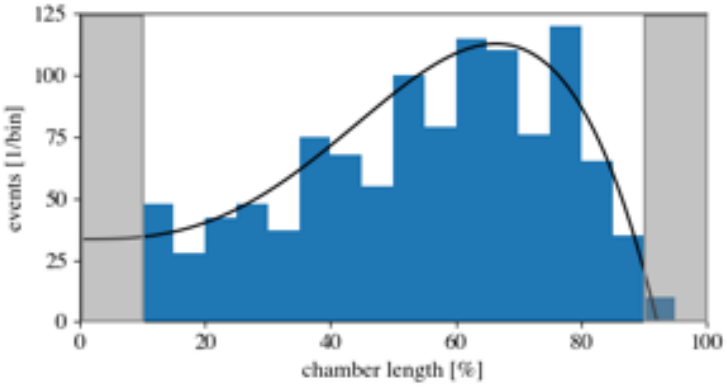

Figure 5.3: Implantation profile of ^{58}Zn ions for the partial statistics of the events (1111 events $\approx$ 3%) together with fit distribution used for stopping efficiency simulation. Only ions stopped between 10% and 90% of the chamber length were considered as correctly implanted inside the detector. Gray rectangles show the parts of chamber length outside this range.

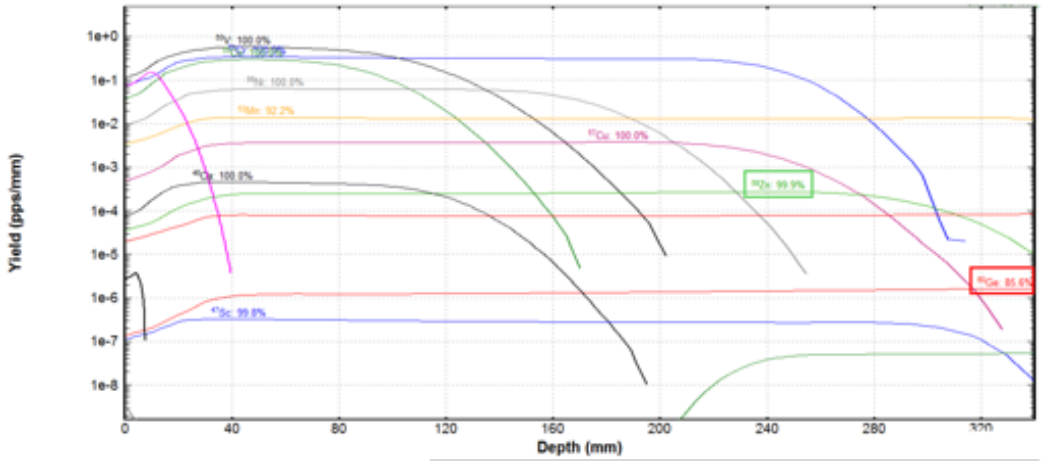

(a)

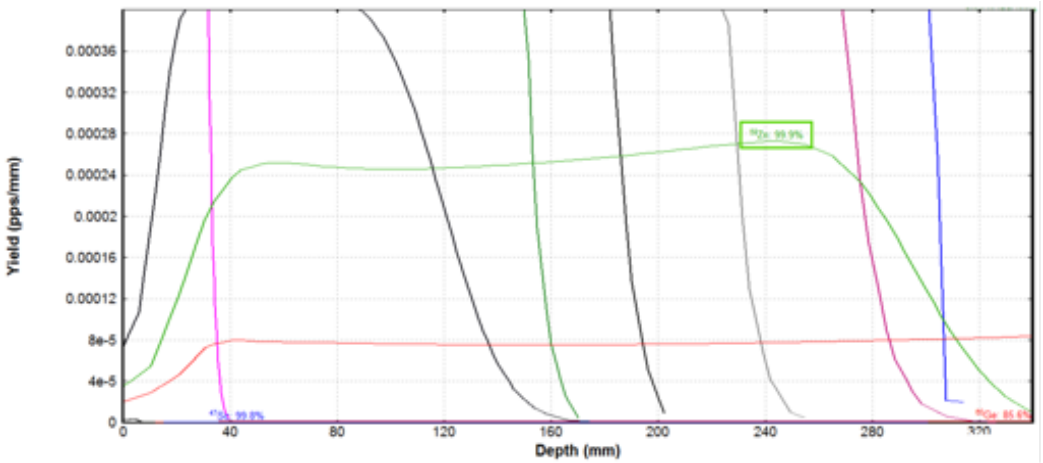

(b)

Figure 5.4: (a) Results of the LISE++ simulations [50] for the ion implantation distributions for all isotopes present in the cocktail beam in log scale with A1900 spectrometer optimized for ^{60}Ge. (b) Zoom on the ^{58}Zn ions distribution in the detector. The majority of the ions is expected to be implanted correctly, which was indeed the case during the experiment.

The simulated stopping efficiency for ^{58}Zn is shown in Figure 5.5. This efficiency differs from the previously presented efficiencies for ^{22}Si and ^{23}Si (see Figure 4.6 in Section 4.1.2). While the plateau region in low energies is similar to that observed in the previous cases, the tail of the efficiency extends much further, to almost 3.5 MeV. In comparison, the efficiencies for the silicon isotopes tended to approach zero between 2.5 and 3.0 MeV. It should be noted, that due to the differences in gas mixture used, the protons in the TAMU experiment had slightly larger ranges for the same energies than particles in the MSU experiment. Nevertheless, this is only partially responsible for the extension of the efficiency's tail. For example, in the TAMU experiment protons with energies 2.5 and 3.0 MeV had ranges of 22.7 and 30.1 cm, respectively, whereas in the MSU experiment protons with energies 3.0 and 3.5 MeV had ranges of 25.4 and 32.8 cm, respectively. Another reason of this discrepancy is the fact that if the proton is emitted from the proximity of the cathode, it has a larger volume inside the chamber to be stopped, especially if it is emitted diagonally towards one of the chamber corners.

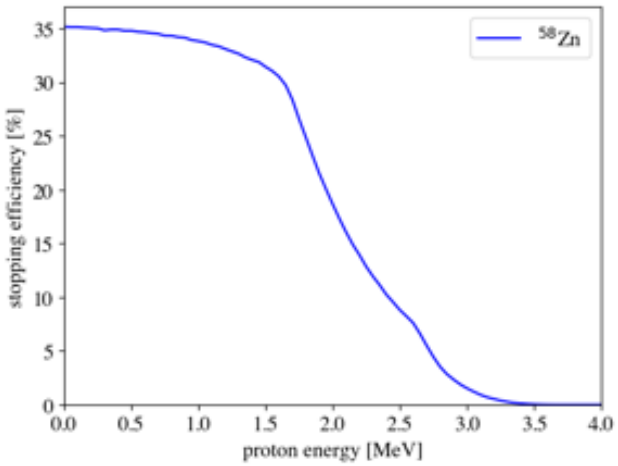

Figure 5.5: Stopping efficiency as a function of the proton energy simulated for ^{58}Zn. The efficiency includes the time-dependence characteristic due to the ion drifting in the gas. For this reason, it is around 35 % at its maximum. The ions drift towards the cathode, decreasing the total efficiency, but contribute to the extension of the energy range in which the protons might get implanted inside the chamber to almost 3.5 MeV. See text for details.

5.2 Most exotic germanium isotopes

5.2.1 First identification of ^{59}Ge

The experimental data collected in the ^{59}Ge setting allowed for the first identification of this isotope. Among all events recorded, four were identified as ^{59}Ge on the basis of DAQ1 (see Section 3.2). Three of these events were recorded also by DAQ2, whereas one unfortunately happened during dead-time in DAQ2. In Figure 5.6 identification-plots ΔE - ToF2 based on data from both DAQs are displayed. All ^{59}Ge events are clearly separated from the rest of the ions in the plots, taking also into account the expected gap corresponding to the unbound isotope ^{58}Ga. The plots are based on only triggering ions, nevertheless it is important to mention that there was no ^{59}Ge ion among those non-triggering, hence none was missed by the trigger.

In order to avoid the misidentification of the ^{59}Ge ions due to the pileup of the signals from lighter contaminants, the ΔE and ToF2 signal shapes were inspected and are shown in Figure 5.7. It is evident that both ΔE and ToF signals for each event show no sign of pile-up and the shapes are as expected for a single ion. Therefore these events were identified as belonging to the new isotope ^{59}Ge. Further experimental studies performed after this work confirmed the identification of ^{59}Ge [25]. Despite higher statistics, its 2p decay was not observed [66].

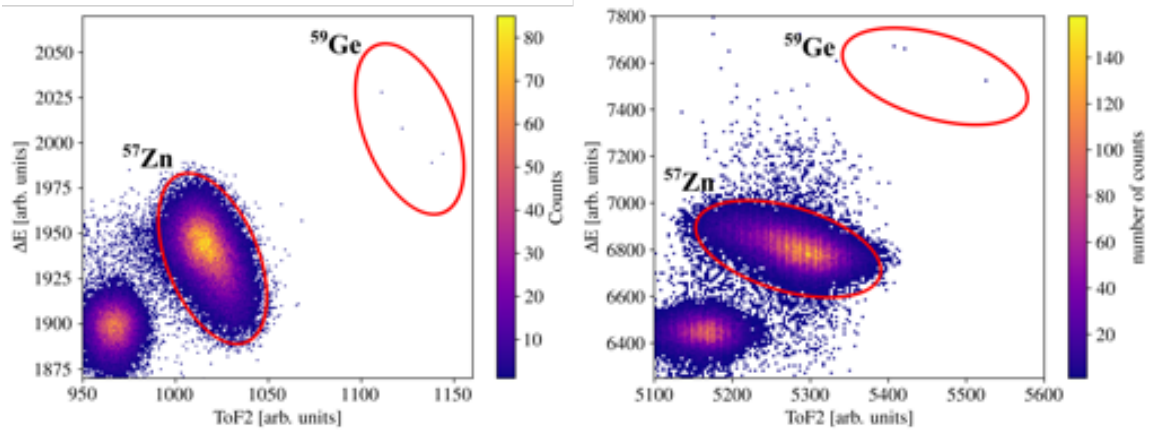

Figure 5.6: Identification plots based on ΔE and ToF2 measurements performed with DAQ1 (left) and DAQ2 (right). Both plots show events assigned to ^{59}Ge being very clearly separated from the other ions. The hole in the ID plot corresponds to the unbound nucleus ^{58}Ga. DAQ1 contains all 4 recorded events, while in DAQ2 those 3 events that did not happen during the dead time are visible.

5.2.2 Cross sections for production of germanium isotopes

Events collected in the A1900 $^{59-62}$Ge settings allowed for calculation of cross sections for production of these exotic isotopes. The cross sections were determined according to the formula

$$\sigma = \frac{N_{ions}}{N_{beam}} \frac{\mu}{d \cdot N_A \cdot T_1 \cdot T_2} \tag{5.2}$$

where N_{ions} and N_{beam} are the number of ions of interest and of all ions in beam, respectively, during the whole run with the given setting, μ is the atomic weight of the target, d is the areal thickness of the target, N_A is the Avogadro number, and T_1 and T_2 are transmissions from the target to the focal plane and from the focal plane to the ΔE detector, respectively. The beam intensity was periodically monitored by a Faraday cup and corrected to account for the beam-off time due to the triggers. The transmission T_1 was determined by means of the LISE++ ion-optics simulations [50], whereas T_2 was determined from the ratio of the particle numbers observed at the FP and the ΔE detector. All the measured values for each setting (N_{ion}, N_{beam} and the transmissions), as well as the calculated cross sections, are summarised in Table 5.1. The table also contains values obtained in the previous A1900 experiment [26] for $^{60-62}$Ge and the predictions from EPAX3 parametrization [39] for the primary beam and target used in our experiment.

Table 5.1: For each of the $^{59-62}$Ge isotopes, the table summarises the numbers of ion N_{ions} and of beam particles N_{beam} measured, the transmissions T_1 and T_2, the cross section σ (± stat. ± syst. uncertainties), as well as σ measured in the previous A1900 experiment (for isotopes $^{60-62}$Ge, 140 A·MeV ^{78}Kr beam on a Be target) and the EPAX3 parametrization predictions.

			T [%]		cross sections [barn]		
Z	N_{ions}	N_{beam}	T_1	T_2	σ_{exp}	σ_{lit} [26]	σ_{EPAX3} [39]
59	4	1.1×10^{17}	24(5)	70(10)	$(17^{+13}_{-9} \pm 5) \times 10^{-15}$	–	1.56×10^{-12}
60	73	2.3×10^{16}	24(5)	60(10)	$(1.6 \pm 0.2 \pm 0.5) \times 10^{-12}$	$(0.38^{+0.27}_{-0.31}) \times 10^{-12}$	4.12×10^{-11}
61	1230	6.2×10^{15}	26(5)	70(10)	$(8.2 \pm 0.2 \pm 2.0) \times 10^{-11}$	$10(5) \times 10^{-11}$	1.13×10^{-9}
62	1237	5.8×10^{14}	28(5)	70(10)	$(8.2 \pm 0.2 \pm 2.0) \times 10^{-10}$	$4.8(20) \times 10^{-9}$	3.25×10^{-8}

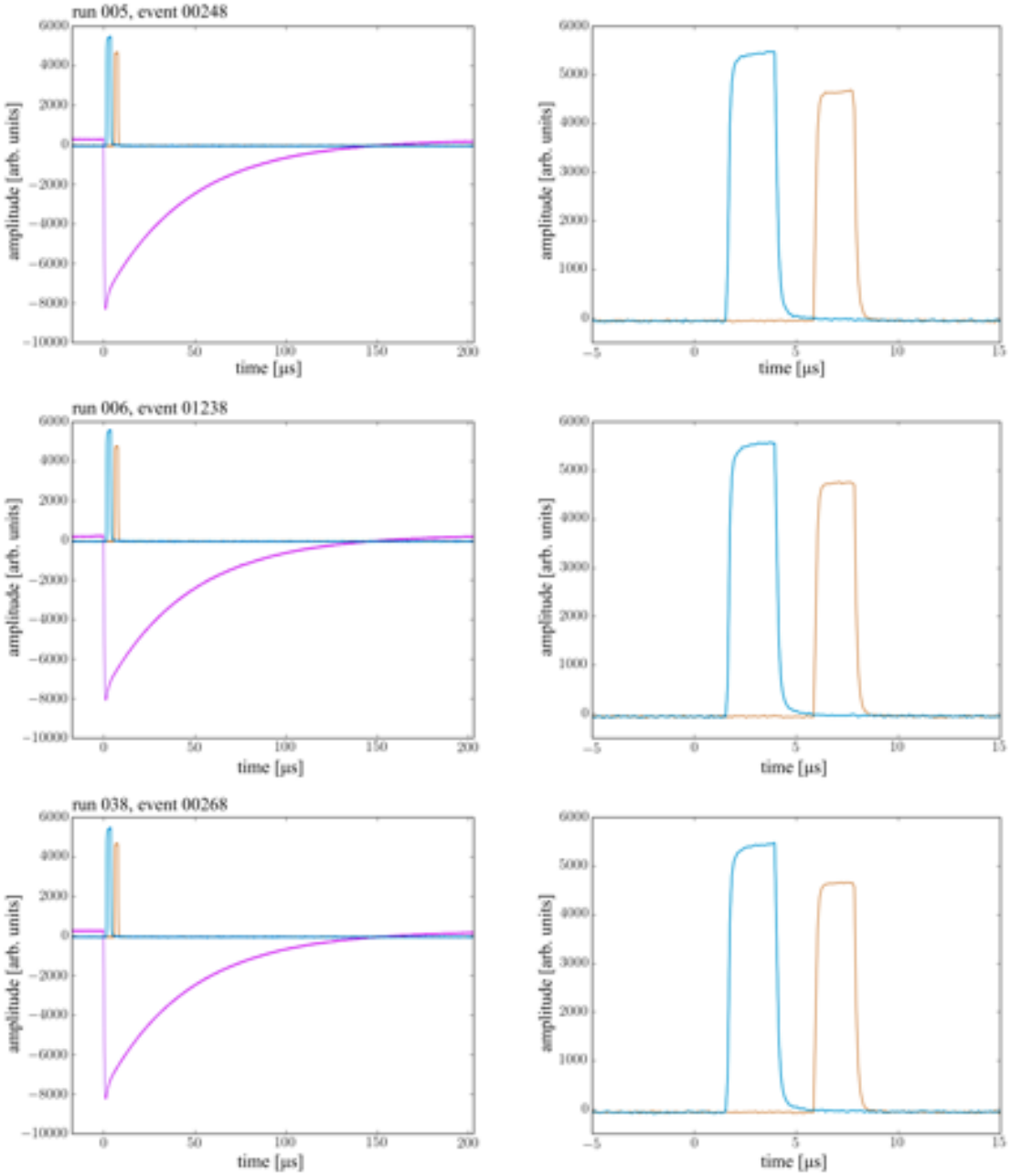

Figure 5.7: (left) Waveforms of signals giving the ΔE (magenta, negative), ToF1 (blue, positive) and ToF2 (yellow, positive) ion-identification signals for the three ^{59}Ge events acquired by the DAQ2 oscilloscope. (right) ToF1 and ToF2 signals, expanded. See text for details.

The results of this study, along with those of two previous experiments (A1900 [26] and GANIL [29]) and EPAX3 predictions for primary beams and targets used in both cases are shown also in Figure 5.8. The values of the germanium isotopes production cross sections show a smooth trend as a function of mass, with no noticeable kink at mass 60, which could indicate in-flight losses of ^{60}Ge due to 2p decay with very short half-life, as was suggested in Ref. [26]. The cross-section value found in this work for this isotope is four times larger than the one obtained in the previous A1900 experiment using the same target and primary beam. Nevertheless, it is still approximately two times lower compared to the value obtained in the GANIL experiment [29]. This difference could be attributed to the use of a ^{70}Ge beam on a Ni target in GANIL, instead of ^{78}Kr on Be, indicating that the first combination of beam and target might be a better choice when it comes to production of the most exotic germanium isotopes. One might also expect that the cross section for the production of ^{59}Ge would be higher in the fragmentation reaction of a ^{70}Ge beam on a Ni target. However, the higher intensity available for a ^{78}Kr beam and the better thermal properties of a Be target could make the alternative choice more advantageous. Nonetheless, subsequent studies were conducted using the latter beam and target configuration [25]. The cross section obtained for the production of ^{60}Ge aligns with the value found in this work. Although the value of σ for ^{59}Ge, was slightly larger, the values are compatible within error bars (see Figure 5.8). The EPAX3 parametrization overestimates the production cross sections calculated in all experiments by one to two orders of magnitude, regardless of the beam and target combination, and this discrepancy increases with decreasing A, i.e. for more exotic nuclei. The limited prediction capabilities of models when looking at the productions of nuclei so far from stability makes the measurement of production cross sections of vital importance for planning future experiments.

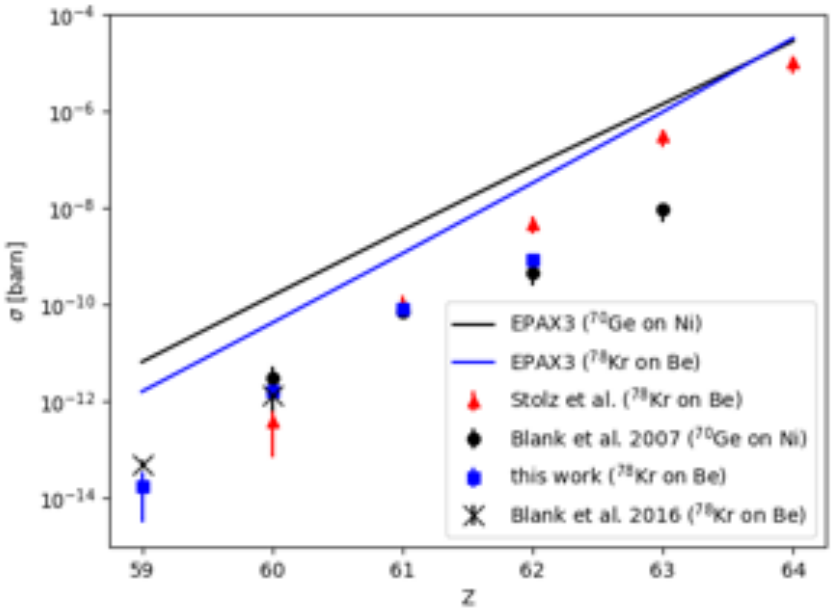

Figure 5.8: Cross sections for neutron-deficient germanium isotopes calculated within this study (blue squares), values obtained in previous A1900 experiment [26] (red triangles), GANIL experiment [29] (black circles) and an experiment performed after these studies in RIKEN [25] (black crosses), as well as EPAX3 predictions (blue and black solid lines). For all experimental results and predictions, the respective combinations of beam and target are listed.

5.3 β-delayed charged-particle decay of ^{60}Ge

Among all triggering ions, 41 events were found to meet the requirements set by the ^{60}Ge gate. 28 of them were implanted within the active volume of the OTPC. The rest of the ions stopped either close to the wall or outside the detector, as expected on the basis of the shape of the implantation

profile predicted by LISE++ [50]. The implanted ions were investigated for emission of β-delayed protons and such a decay was found in 19 cases. An example event is shown in Figure 5.9.

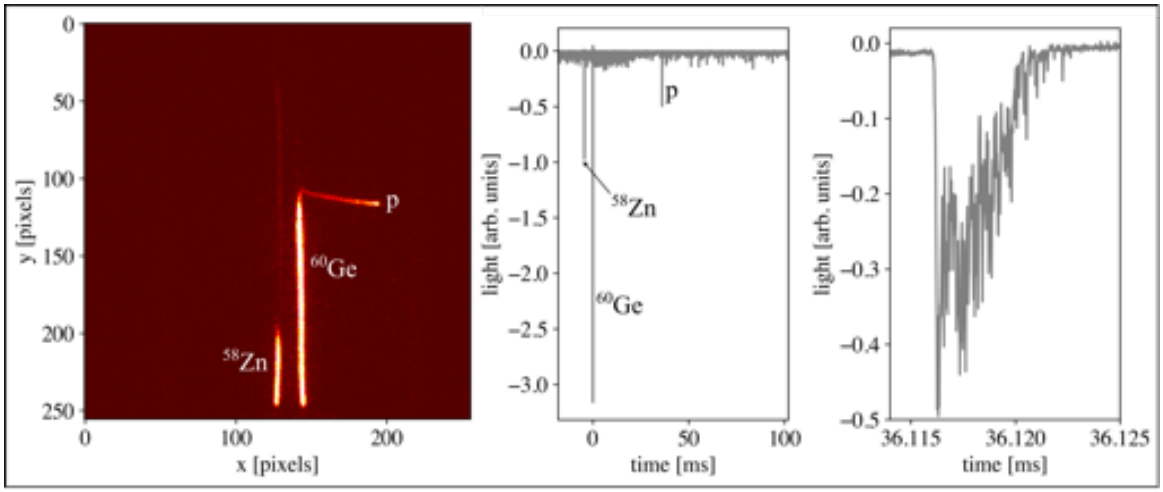

Figure 5.9: Decay event with β-delayed proton emission from ^{60}Ge recorded by the CCD (left) and the PMT (middle: whole implantation window and right: zoom on proton signal). The CCD shows the presence of two ions, identified as ^{58}Zn and ^{60}Ge. The assignment of the ions to the trajectories was performed on basis of light in PMT and CCD, and identification-signals timing. Therefore it was possible to assign the longer trajectory on the CCD picture to the more intense signal (ion) in the PMT, which was the triggering ion, as ^{60}Ge, which subsequently emitted a proton. The less intense signal in CCD and PMT, which arrived before the trigger, was identified as ^{58}Zn. The zoomed part of the PMT signal shows the quality of the data on the decay, which was not sufficient to recognise precisely the Bragg peak shape, but good enough to decide whether the proton was moving upwards or downwards, as in this example.

For each decay event, the time between the arrival of an ion and the proton emission was measured. Fitting of an exponential decay distribution with a finite-time observation window with maximum likelihood method yielded the half-life of ^{60}Ge $t_{1/2} = 20^{+7}_{-5}$ ms. The decay-time distribution of the analysed events is shown in Figure 5.10.

The half-life for Fermi decay to the IAS in the daughter ^{60}Ga was determined from Equation 1.9 assuming a pure Fermi transition:

$$t^F_{1/2} = \frac{C}{f \cdot |M_F|^2} \tag{5.3}$$

where $|M_F|^2 = 4$ for $^{60}_{32}\mathrm{Ge}_{28}$ and f is the phase-space factor for the transition to the IAS. To determine the phase-space factor, the IAS energy was determined on basis of Coulomb displacement energy systematic for $T = 2$ [7] to be 2516(280) keV, giving a decay energy to the IAS of 9664(6) keV, and f determined with the logft calculator [67]. The resulting partial F-decay half-life of ^{60}Ge is 44 ms [64]. The theoretically predicted GT-decay half-life is 82 ms (from finite-range droplet model and the folded-Yukawa single-particle potential combined with the quasi-particle random phase approximation (QRPA) calculations [65]). The predicted half-life of F+GT decay is therefore $t_{1/2} = ((t^F_{1/2})^{-1} + (t^{GT}_{1/2})^{-1})^{-1} = 29$ ms, which is within two σ from the experimental value. Other theoretical calculations using the proton-neutron QRPA, including particle-hole and particle-particle residual interactions, yielded a F+GT-decay half-life value between 31.3 and 34.6 ms [63], depending on mass model used – also in agreement with the experimental value.

Among the 19 observed protons, 11 were classified as emitted downwards. This was decided on the basis of shape of the signal, the amplitude of which increases along the trajectory, towards its end. In the remaining 8 cases, the assignment of the trajectory direction was not possible. This may have been caused by the nearly horizontal emission of a proton or its energy being so large, that the Bragg peak structure by the end of the trajectory is not visible at all, because the protons escape the chamber. There was no proton observed emitted clearly upwards. This can be explained by the

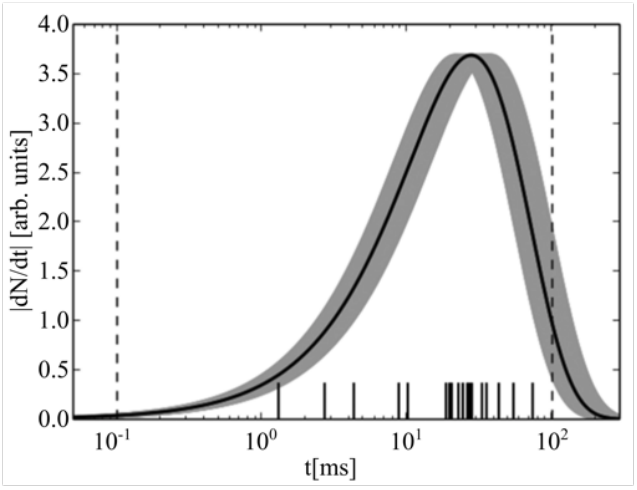

Figure 5.10: Logarithmic distribution of decay times for the 19 identified ^{60}Ge decays (black vertical bars). The bell-shaped curve corresponds to the distribution resulting from $t_{1/2} = 20^{+7}_{-5}$ ms obtained with maximum-likelihood method, with uncertainties shown as gray areas. The dashed vertical lines show the edges of the observation window, resulting from the dead time after the trigger (100 μs) and the end of the decay gate (around 100 ms, see Table 3.1).

drift of the not fully neutralised ions towards the cathode, as described in Section 5.1.3. Therefore, for an estimate of the branching ratio, 11 clearly downwards-emitted protons as well as 4 out of the 8 with unassigned direction were considered. Assuming 50% detection probability and taking into account the number of ions (28), a branching ratio for βp emission of $\approx 100\%$ is found.

The analysis of trajectory lengths of the protons, where approximate measurement of PMT signal was possible (13 events in total), yielded energies between 2 and 3 MeV. In this energy range the proton stopping efficiency drops rapidly, hence most of the protons would not stop inside the OTPC detector. Since the Bragg peak was not clearly observed in any of these events, none of them was classified as fully stopped inside the active volume of the detector.

Since for the overwhelming majority of the ions only half of the solid angle was observable, it is reasonable to consider the possibility of unobserved β2p emission from ^{60}Ge during the experiment. Assuming no correlation between the two particles, the probability of observing both of them when emitted from the vicinity of the upper wall is $\approx$25%. The fact that β2p was not observed in any of the 28 events, sets an upper limit for the branching ratio, $b_{\beta 2p} < 14\%$. Such small value is not totally unexpected: the IAS in ^{60}Ga has energy of only 2520(280) keV, which is the same as S_{2p} within the uncertainties. Moreover, in the mirror nucleus of its β-daughter ^{60}Ga, ^{60}Cu, there are several 1^+ states below the IAS. Being a similar structure expected in ^{60}Ga, such 1^+ states would draw GT strength from the 0^+ ^{60}Ge g.s. decay. Therefore, for β2p emission to happen with significant probability, a remarkable β strength at energies above the IAS would be required.

5.4 β decay of ^{58}Zn

5.4.1 First observation of βp emission

The ion optics setting of the A1900 were optimized for germanium isotopes, with hardware gates set to allow triggering the DAQ2 by some zinc ions as well. Therefore, while looking for ^{60}Ge decay, it was also possible to investigate the less exotic, though still very interesting, ^{58}Zn. Almost 36000 ions of ^{58}Zn triggered the DAQ2 and were implanted correctly into the detection setup, with the implantation profile shown in Figure 5.3 and the identification plot in Figure 5.1.

The analysis of the decay events of ^{58}Zn ions yielded the identification of 88 decays by β-delayed proton emission, being this the first observation of this decay channel of ^{58}Zn. Due to the beam intensity events with more than one ion implanted were registered. In order to avoid ambiguities, only

those with all ions stopped inside the chamber were considered in the analysis. With the exception of the ^{60}Ge ions, the number of which was negligible in comparison to ^{58}Zn (see Section 5.3), the only other isotope present in the cocktail beam which has the βp decay channel open, although not observed, yet, was ^{57}Cu. It has half-life longer than ^{58}Zn, 196 ms [2], giving a probability of around 30% to observe a possible decay event within the decay gate. Moreover, the statistics for it was almost 7 times lower than for ^{58}Zn. Therefore, for each ^{58}Zn event there was an average of 0.05 of ^{57}Cu ions present. The Q-value for βp emission of ^{57}Cu (1443 keV [68]) is 4 times lower than the one of ^{58}Zn. All these considerations render the possible influence of unobserved ^{57}Cu βp on the results obtained for ^{58}Zn negligible.

As detailed in Section 5.1, the probability of proton detection within the observation window when the ions drift is taken into account is 35(2)%. The resulting branching ratio is 0.7(1)%, which is compatible with the previously given upper limit of 3% [31]. Example events with βp of ^{58}Zn are shown in Figure 5.11.

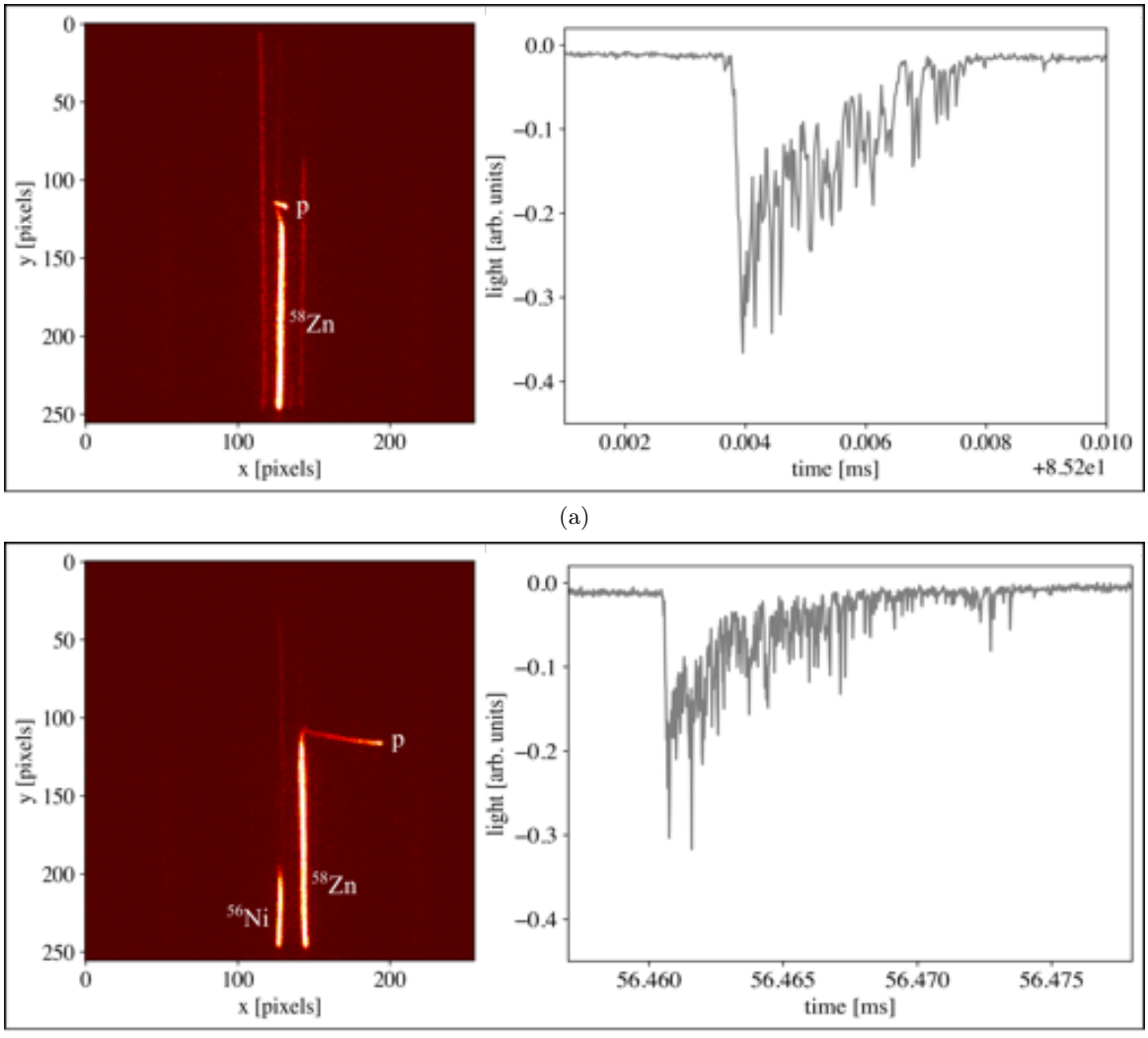

Figure 5.11: Example events with β-delayed proton emission from ^{58}Zn recorded by CCD (left) and PMT (right). In both cases the protons were stopped inside the chamber. Subfigure (a) contains a low-energy proton with $E_p = 0.79(13)$ MeV, whereas (b) contains a proton with $E_p = 1.85(8)$ MeV. The other ion present in the CCD picture in (b) was identified to belong to the less exotic, non-triggering ^{56}Ni ion. The faint traces visible in both CCD pictures are caused by light ions passing through the chamber before the beginning of the observation window.

Among the observed protons, 55 clearly escaped the OTPC detector and were not considered further in the analysis. The energies of the stopped protons were established on the basis of the lengths of

their trajectories and the appropriate range-energy dependence resulting from simulations [40]. The energy spectrum is shown in Figure 5.12.

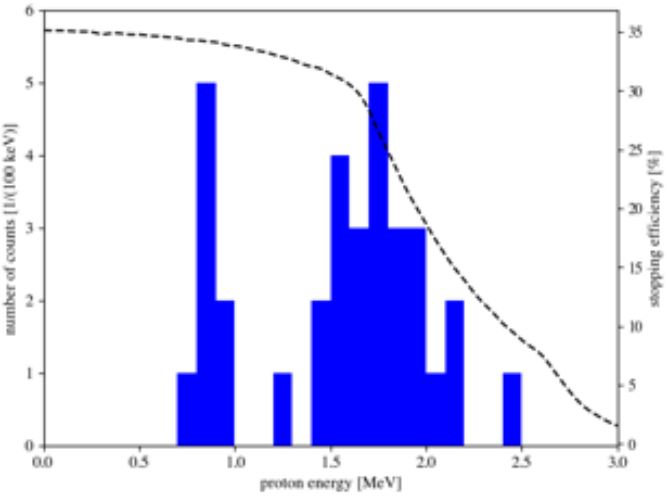

Figure 5.12: Energy spectrum of the 33 ^{58}Zn protons for which the energy could be calculated. The dashed black line shows the proton stopping efficiency as function of energy. The spectrum contains two main proton groups. See text for details.

The gas mixture density allows for the observation of protons with lowest energies around 200-400 keV. However, all the measured protons energies exceed 700 keV. The upper proton energy spectrum limit is determined by the energy at which the protons escape from the chamber. As it depends on the emission point, angle and the timing of the decay respective to the ion's drift, this boundary is broader and is situated between 1.7 and almost 3.5 MeV (see Section 5.1.3).

Two main groups of protons are visible in Figure 5.12. The lower energy group of protons centers around 0.85 MeV, corresponding to an excitation energy in ^{58}Cu of approximately 3.75 MeV, assuming decay to the g.s. of ^{57}Ni. It suggests a presence of one, or more, peaks located close to each other. The example event presented in Figure 5.11(a) belongs to this group. Another cluster of proton energies extends between 1.4 and 2.2 MeV, corresponding to the excitation energy between 4.3 and 5.1 MeV. The energy resolution combined with the level density does not allow for disentangling of individual proton transitions contributing to this group, however a division into a main group centered around 1.75 MeV and another, smaller group around 2.1 MeV, will be adopted for further discussion.

5.4.2 B(GT) strengths

The structure of the ^{58}Zn β-decay daughter, ^{58}Cu, was previously studied in the ^{58}Ni(^{3}He, t)^{58}Cu charge-exchange reaction by Fujita *et al.* [69] and Hara *et al.* [70], with focus on proton and γ decay of populated levels, respectively. The first study yielded a detailed mapping of the B(GT) distribution in the first few MeV of the proton-emitting energy region [69]. The second experiment addressed also the γ-decay branch of the same levels and established partial branching ratios values for these two competing decay modes up to $E_x = 3.7$ MeV by means of proton-γ coincidences [70]. Above this energy no γ-decay competition was observed. The results of these studies show that there are several states in ^{58}Cu above S_p fed with B(GT) comparable to that for the first excited, proton-bound, 1^+ state. The data obtained in this study allow for further investigation of GT strength distribution above the levels for which B(GT) was already reported [33] and for comparison with the results of CE reactions. Levels in ^{58}Cu identified in CE reactions at excitation energies between 3.4 and 5.2 MeV, corresponding to the range that can be explored within this study, as well as information for the g.s. and the first excited state in ^{58}Cu obtained in both CE and β-decay studies, are listed in Table 5.2.

Despite significant B(GT) observed in the CE reaction, the 3.460 MeV level does not seem to participate in βp emission, since it is not visible in the energy spectrum, although being within the

Table 5.2: Energies, partial branching ratios and B(GT) values for 1^+ states in ^{58}Cu lying in energy-range of interest obtained in ^{58}Zn β decay from this and previous research [33], and CE studies [69,70].

^{58}Zn β decay			^{58}Ni(^{3}He, t)^{58}Cu CE reaction		
E_x [MeV]	$b_{\beta p}$ [%]	B(GT)	E_x [MeV]	$b_{\beta p}$ [%]	B(GT)
0	0	0.30(13) [33]	0		0.155(1) [69]
1.051	0	0.17(3) [33]	1.051		0.265(13) [69]
			3.460	62(11) [70]	0.173(11) [69]
≈3.75	0.06(2)	≥ 0.015(8)	3.678	15(17) [70]	0.155(10) [69]
			3.717	100 [70]	0.050(5) [69]
≈4.65	0.20(6)	0.13(6)	4.720	100 [70]	0.042(4) [69]
			5.065	100 [70]	0.040(4) [69]
≈5.0	0.05(3)	0.05(4)	5.160	100 [70]	0.250(14) [69]

detectable energy range. The lowest-energy observed group of protons most likely corresponds to the decay of the 3.678 MeV and 3.717 MeV 1^+ states in ^{58}Cu. It is worth noting that the 3.678 MeV state decays mostly by γ decay. Its decay via γ emission, as well as that of the 3.460 MeV level, was observed also in the $\beta\gamma$ decay study of ^{58}Zn a few years ago [71]. The main part of the higher-energy proton cluster centered around 1.75 MeV possibly corresponds to the decay of 4.720 MeV 1^+ state, while its higher-energy part around 2.1 MeV probably matches to the unresolved 5.065 MeV and 5.160 MeV 1^+ levels in ^{58}Cu.

The calculated partial branching ratios and B(GT) values for the three proton groups observed in this work are listed in Table 5.2. The results take into account the proton stopping efficiency at different energies. Despite the small $b_{\beta p}$, the Gamow-Teller strength for the main observed proton group is comparable in intensity to the value for proton-bound 1.052 MeV state obtained in a previous β-decay study [33]. It is important to emphasize that even when the probability of βp emission is very small, it should not be neglected when looking at B(GT) distribution. The level at 3.460 MeV observed with significant B(GT) strength in CE studies does not appear to decay by βp emission. The two levels around 3.7 MeV draw a much smaller strength than obtained in the CE reaction studies.

The experimental results are first compared with the B(GT) distribution obtained within the QRPA approach based on self-consistent deformed Hartree-Fock mean field with Skyrme forces [72, 73]. The calculations use a spherical solution for ^{58}Zn and Skyrme SLy4 interaction. The spherical approximation seems justified as it lies only two protons above the doubly magic ^{56}Ni nucleus. The energy distribution of the GT strength can therefore be understood in terms of transitions between spherical shells. This distribution exhibits pronounced peaks below 2.5 MeV and above 7 MeV, but no sizeable GT strength was found between 4 and 6 MeV. Deformation and pairing effects in ^{58}Zn are expected to introduce fragmentation in the Gamow-Teller (GT) strength due to energy splitting of spherical levels and partial occupation of states. By reducing the pairing interaction, the equilibrium configuration deformation might be increased to $\beta \approx -0.1$. Although such a deformation is relatively small, it leads to an enhancement of GT strength around 5 MeV, which aligns with the experimental findings, and is therefore included in the calculations performed by P. Sarriguren [73]. The resulting B(GT) distribution is shown in Figure 5.13.

The main transitions were found to occur from highly occupied proton states to nearly empty neutron states. Significant strength is still predicted for transitions with excitation energies below 3 MeV and above 7 MeV, i. e. transitions between states with the same orbital angular momentum L. The strength between 4 MeV and 7 MeV is relatively smaller due to the influence of different dominant L values, but it remains sizeable since it arises from transitions between deformed states involving

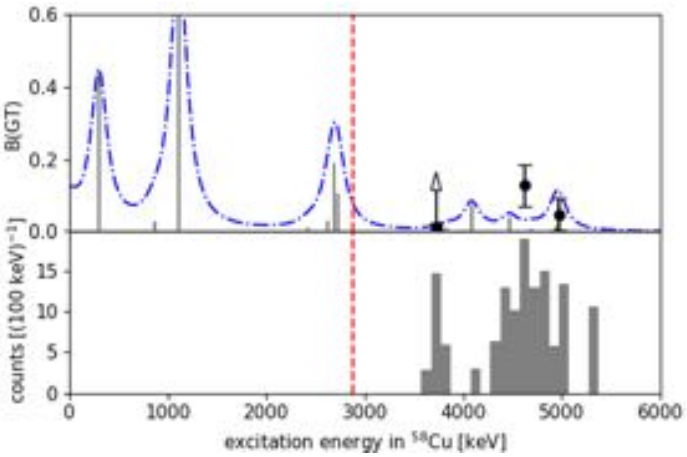

Figure 5.13: The upper subfigure shows the B(GT) values calculated for three observed proton groups (full circles with errorbars) and from QRPA calculations up to $E_x = 6$ MeV, with gray bars showing the calculations results and the dash-dotted blue line shows the calculated values folded with the 200 keV-wide Breit-Wigner distribution to account for the limited energy resolution. The bottom subfigure shows the energy spectrum of βp from ^{58}Zn corrected for the efficiency (see Figure 5.12), as a function of the excitation energy in ^{58}Cu. The dashed vertical line in both subfigures shows the S_p value in ^{58}Cu. Figure from Ref. [73].

many different L values. Therefore, within this approach, the effects induced by deformation were found to be responsible for the strength between 3 and 7 MeV observed in the experiment.

5.4.3 Impact on the rp-process

As it was mentioned in Section 1.2.2, ^{58}Zn is situated on the predicted path of the rp process. The impact of the β-delayed proton emission of ^{58}Zn on it using a one-zone X-ray burst model [74,75] was investigated in collaboration with H. Schatz [73]. The influence of βp emission on energy generation and burst light curve resulted to be negligible because the β- and βp daughters, ^{58}Cu and ^{57}Ni, remain in (p, γ)-(γ, p) equilibrium with each other, at least for most of the conditions in which the rp process occurs in this mass region. Nevertheless, the βp decay of ^{58}Zn may affect the final $A = 57$ abundance in the burst ashes, which has influence on Urca cooling in the neutron star crust [76]. A branch of 100% would increase it by a factor of 3-4, with final abundances up to 2×10^{-5}, depending on the burst model. However, both the 0.7% branch measured here and the previous upper limit of 3% only change the final abundance up to a few percent.

Chapter 6

Summary

When approaching the limits of stability, the binding energy difference between neighboring nuclei increases, leading to opening of new decay channels and the appearance of exotic radioactivities. The β-delayed γ decay, which is the most common decay mode for radioactive nuclei closer to stability, loses to β-delayed particle emission near to the proton drip line, since the available energy for the β^+/EC decay increases while the particle emission threshold decreases. At the edge of stability on the proton-rich side of the nuclide chart, a variety of β-delayed multi-particle emission modes are therefore emerging and can dominate the decay of such nuclei.

Two groups of neutron-deficient isotopes showing open energy windows for a diversity of exotic decay channels were investigated within this study. β-delayed charged particle emission from ^{22}Si and ^{22}Si was studied at the Cyclotron Institute of Texas A&M University. ^{59,60}Ge and ^{58}Zn were investigated at the National Superconducting Cyclotron Laboratory at Michigan State University. In each of these experiments, radioactive beams composed of the ions of interest were produced in fragmentation reactions of ^{28}Si and ^{78}Kr beams, respectively, and selected among the reaction products by the electromagnetic fields of the MARS and A1900 separators, respectively. The ions of interest were then implanted into the OTPC detector and their decays were investigated. Within this work the complete analysis of the data collected was performed. The obtained results were discussed in the context of previously known experimental results, theoretical calculations, and supported with Monte Carlo simulations. A summary of the region of the chart of nuclei studied in this work, with the isotopes of interest highlighted, is shown in Figure 6.1.

Among the results of the first of the experiments are the confirmation of the previously known β-delayed one and two-proton emission (βp and β2p) from ^{22}Si and ^{23}Si. The study of the former isotope allowed to establish the absolute branching ratio for β2p emission. Further studies with larger statistics are needed in order to investigate in detail the mechanism of β2p emission. For ^{23}Si, the absolute branching ratios were determined for both decay branches and a new low-energy βp transition was identified. β2p emission through levels below the IAS was observed. The opening angle between the two protons in the observed β2p events suggests sequential emission mechanism. Moreover, two new decay modes were discovered in ^{23}Si: β3p and βpα emission. For the latter, two possibilities, namely β-delayed proton + α and α + proton were discussed. It was concluded, that the identified decay event most likely corresponds to the decay via proton emission from IAS in ^{23}Al to an excited 0^+ state in ^{22}Mg, followed by α emission to the g.s. in ^{18}Ne. A reconstructed β3p event was also found to be corresponding to the emission from the IAS in ^{23}Al. The branching ratios for these two channels are discussed in the context of the properties of other known emitters with T_z ranging from $-3/2$ to $-7/2$, see Figure 4.24. They are also marked in Figure 6.1. The fact, that the $b_{\beta p\alpha}$ of $T_z = -5/2$ ^{23}Si is comparable to the values obtained for $T_z = -3/2$ nuclei indicates the influence of odd-even effects on the occurrence of this decay mode rather than of the presence of the α-conjugate nucleus in the final state [59].

In an experiment at the National Superconducting Cyclotron Laboratory the new isotope ^{59}Ge was identified on the basis of 4 events. In addition, the production cross sections for the neutron-deficient $^{59-62}$Ge nuclei were measured. The dependence of the cross section on the atomic number was found to show a smooth behaviour, see Figure 5.8: no sudden drop indicating in-flight losses

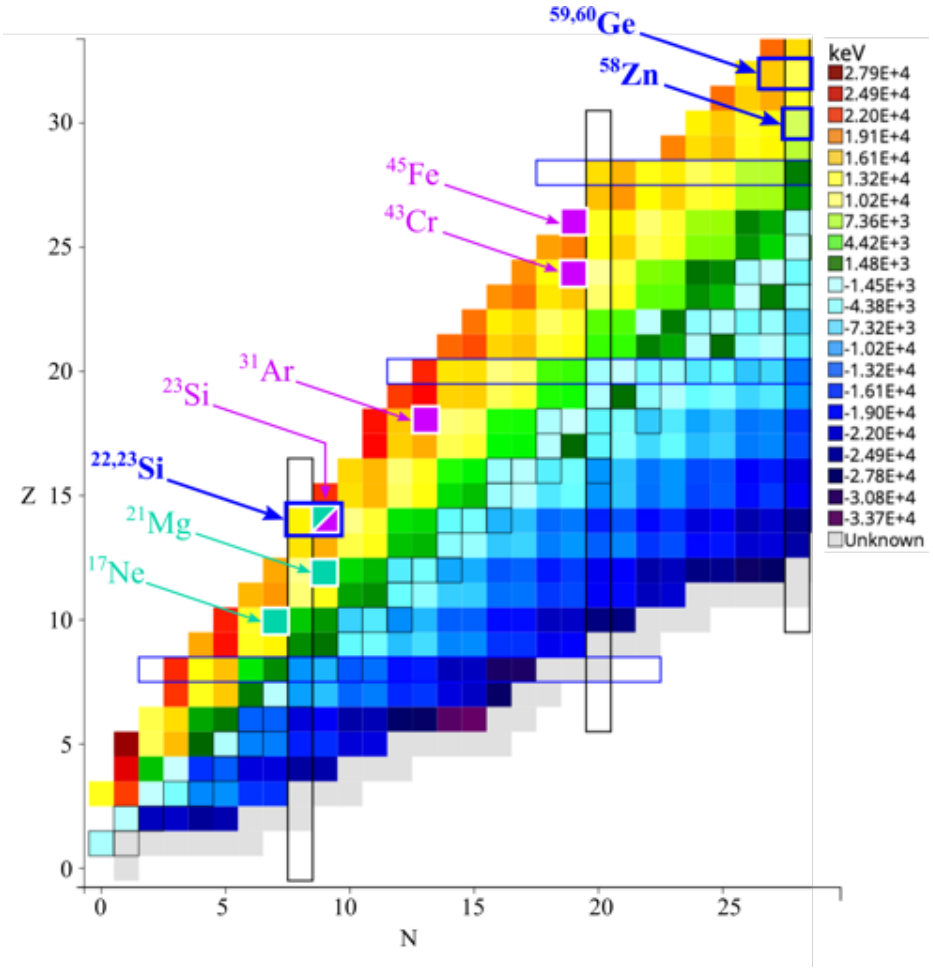

Figure 6.1: Nuclide chart up to N = 28 [2]. The colour scale on the chart depict the Q_{EC} value. The nuclei investigated within this thesis are marked with blue arrows and rectangles. All known β3p and βpα/$\beta\alpha$p emitters (with the exception of the special cases of ^{9}C and ^{13}O, see Section 4.3.4) are marked with purple and turquise squares and arrows, respectively. The region of these exotic decay modes extends from ^{17}Ne, little below the silicon isotopes, up to ^{45}Fe. A broad variety of open decay channels in these nuclei and the continuous development of experimental techniques encourages planning further research.

of ^{60}Ge was observed at A = 60, nevertheless, a steeper decrease in the cross sections with respect to the EPAX3 parametrization was observed and the measured ^{59}Ge cross section was found to be two orders of magnitude lower than the EPAX3 predictions. The observation of ^{59}Ge opened a path for further investigation of this nucleus, which was performed after the current study by Blank and collaborators at RIKEN and, despite larger statistics, the 2p decay of this isotope was not observed [66]. The cross sections were found to be compatible with values from this study [25]. The fact that the production cross section predictions are not reliable so far from stability emphasizes the necessity of measurements such as those performed within this and other experiments. The continuous development of experimental nuclear physics instrumentation and techniques, that began more than 100 years ago, cannot proceed without increasing our expertise on designing efficient experiments.

β decay of ^{60}Ge was measured here for the first time. βp emission from this isotope was observed and the β-decay half-life established as $t_{1/2} = 20^{+7}_{-5}$ ms. This value agrees with theoretical predictions accounting for allowed F and GT β transitions. ^{60}Ge has Q_{EC} lower than ^{23}Si (12.1(4) MeV and 17.2(5) MeV, respectively), but presents a similarly rich collection of open decay channels. Nevertheless, the well below zero value of S_p in ^{60}Ga makes it unsurprising that the ^{60}Ge β decay was found to proceed via βp emission with a branching ratio compatible with 100%. A limit for β2p emission was established as $b_{\beta 2p} < 14\%$. As the IAS in ^{60}Ga does not exceed the S_{2p}, this value may in fact

be much lower. However, further investigations with higher statistics are required to study in detail the less-probable decay modes in this nucleus. β decay of ^{58}Zn was also investigated and the βp emission from this nucleus was observed for the first time, with a branching ratio of 0.7(1)%. Despite $b_{\beta p}$ being small, the obtained proton energy spectrum allowed to study the B(GT) distribution to states just above the proton separation energy in the ^{58}Cu daughter. The results were compared with QRPA calculations performed with the assumption of both spherical and deformed shape of ^{58}Zn and it was concluded that the β decay strength feeding proton-unbound states in the daughter nucleus is generated by effects induced by deformation. The impact of the obtained branching ratio on the rp-process was also investigated: its influence on the abundance of A = 57 nuclei was found to be of the order of up to a few percent. Further measurements with complementary techniques and larger statistics are needed to study the full range of the proton spectrum with good resolution, in order to fully establish the B(GT) distribution above the S_p.

The results obtained within this dissertation cover a broad variety of exotic phenomena, from identification of new decay channels in nuclei with A $\approx$ 20, up to measuring the low, yet important-to-be-considered, branching ratios at A $\approx$ 60. The identification of such decay modes is a rewarding and satisfying task by itself, but also provides an input to theoretical calculations in fields of astrophysics and nuclear structure. The aspiration of an holistic explanation of the laws governing our Universe requires both brilliant ideas and constant accumulation of tiny building blocks of experimental knowledge. The study of phenomena at the very edges of nuclear stability contributes to the latter by allowing us to test the limits of applicability of the theories that have been proven to work excellently in stable systems.

List of Figures

List of Tables

Bibliography

[1] Discovery of Nuclides Project, www.people.nscl.msu.edu/∼thoennes/isotopes/ (01.12.2022).

[2] NNDC NuDat3.0, www.nndc.bnl.gov/nudat3/ (01.12.2022).

[3] K. S. Krane. *Introductory Nuclear Physics*. John Wiley and Sons, 1988.

[4] Meng Wang, W J Huang, F G Kondev, G Audi, and S Naimi. The AME2020 atomic mass evaluation (II). Tables, graphs and references. *Chinese Physics C*, 45(3):030003, 2021.

[5] P. R. Chowdhury, C. Samanta, and D. N. Basu. Modified Bethe-Weizsäcker mass formula with isotonic shift and new driplines. *Modern Physics Letters A*, 04.01.2005.

[6] I. S. Towner and J. C. Hardy. The evaluation of Vud and its impact on the unitarity of the Cabibbo-Kobayashi-Maskawa quark-mixing matrix. *Reports on Progress in Physics*, 73(4):046301, 2010.

[7] M.S. Antony, A. Pape, and J. Britz. Coulomb displacement energies between analog levels for $3 \leq A \leq 239$. *Atomic Data and Nuclear Data Tables*, 66(1):1–63, 1997.

[8] M. Saxena, W. J Ong, Z. Meisel, D.E.M. Hoff, N. Smirnova, P.C. Bender, S.P. Burcher, M.P. Carpenter, J.J. Carroll, A. Chester, C.J. Chiara, R. Conaway, P.A. Copp, B.P. Crider, J. Derkin, A. Estradé, G. Hamad, J.T. Harke, R. Jain, H. Jayatissa, S.N. Liddick, B. Longfellow, M. Mogannam, F. Montes, N. Nepal, T.H. Ogunbeku, A.L. Richard, H. Schatz, D. Soltesz, S.K. Subedi, I. Sultana, A.S. Tamashiro, V. Tripathi, Y. Xiao, and R. Zink. ^{57}Zn β-delayed proton emission establishes the ^{56}Ni rp-process waiting point bypass. *Physics Letters B*, 829:137059, 2022.

[9] C. Mazzocchi, Z. Janas, J. Döring, M. Axiotis, L. Batist, R. Borcea, D. Cano-Ott, E. Caurier, G. de Angelis, E. Farnea, A. Faßbender, A. Gadea, H. Grawe, A. Jungclaus, M. Kapica, R. Kirchner, J. Kurcewicz, S.M. Lenzi, T. Martínez, I. Mukha, E. Nácher, D.R. Napoli, E. Roeckl, B. Rubio, R. Schwengner, J.L. Tain, and C.A. Ur. First measurement of β-decay properties of the proton drip-line nucleus ^{60}Ga. *The European Physical Journal A - Hadrons and Nuclei*, 12(3):269–277, 2001.

[10] R. Barton, R. McPherson, R. E. Bell, W. R. Frisken, W. T. Link, and R. B. Moore. Observation of delayed proton radioactivity. *Canadian Journal of Physics*, December 1963.

[11] M. D. Cable, J. Honkanen, R. F. Parry, S. H. Zhou, Z. Y. Zhou, and Joseph Cerny. Discovery of Beta-Delayed Two-Proton Radioactivity: ^{22}Al. *Physical Review Letters*, 50(6):404–406, 1983.

[12] Marek Pfützner and Chiara Mazzocchi. *Handbook of Nuclear Physics - Nuclei Near and at the Proton Dripline*. Springer-Verlag, 2022.

[13] M. G. Saint-Laurent, J. P. Dufour, R. Anne, D. Bazin, V. Borrel, H. Delagrange, C. Détraz, D. Guillemaud-Mueller, F. Hubert, J. C. Jacmart, A. C. Mueller, F. Pougheon, M. S. Pravikoff, and E. Roeckl. Observation of a bound T_z=-3 nucleus: ^{22}Si. *Physical Review Letters*, 59(1):33–35, 1987.

[14] B. Blank, S. Andriamonje, F. Boué, S. Czajkowski, R. Del Moral, J. P. Dufour, A. Fleury, P. Pourre, M. S. Pravikoff, K.-H. Schmidt, E. Hanelt, and N. A. Orr. First spectroscopic study of ^{22}Si. *Physical Review C*, 54(2):572–575, 1996.

[15] S. Czajkowski, S. Andriamonje, B. Blank, F. Boué, R. Del Moral, J.P. Dufour, A. Fleury, E. Hanelt, N.A. Orr, P. Pourre, M.S. Pravikoff, and K.-H. Schmidt. Beta-p,-2p,-alpha spectroscopy of ^{22,23,24}Si and ^{22}Al. *Nuclear Physics A*, 616(1-2):278–285, 1997.

[16] X.X. Xu, C.J. Lin, L.J. Sun, J.S. Wang, Y.H. Lam, J. Lee, D.Q. Fang, Z.H. Li, N.A. Smirnova, C.X. Yuan, L. Yang, Y.T. Wang, J. Li, N.R. Ma, K. Wang, H.L. Zang, H.W. Wang, C. Li, M.L. Liu, J.G. Wang, C.Z. Shi, M.W. Nie, X.F. Li, H. Li, J.B. Ma, P. Ma, S.L. Jin, M.R. Huang, Z. Bai, F. Yang, H.M. Jia, Z.H. Liu, D.X. Wang, Y.Y. Yang, Y.J. Zhou, W.H. Ma, J. Chen, Z.G. Hu, M. Wang, Y.H. Zhang, X.W. Ma, X.H. Zhou, Y.G. Ma, H.S. Xu, G.Q. Xiao, and H.Q. Zhang. Observation of β-delayed two-proton emission in the decay of ^{22}Si. *Physics Letters B*, 766:312–316, 2017.

[17] J. Lee, X. X. Xu, K. Kaneko, Y. Sun, C. J. Lin, L. J. Sun, P. F. Liang, Z. H. Li, J. Li, H. Y. Wu, D. Q. Fang, J. S. Wang, Y. Y. Yang, C. X. Yuan, Y. H. Lam, Y. T. Wang, K. Wang, J. G. Wang, J. B. Ma, J. J. Liu, P. J. Li, Q. Q. Zhao, L. Yang, N. R. Ma, D. X. Wang, F. P. Zhong, S. H. Zhong, F. Yang, H. M. Jia, P. W. Wen, M. Pan, H. L. Zang, X. Wang, C. G. Wu, D. W. Luo, H. W. Wang, C. Li, C. Z. Shi, M. W. Nie, X. F. Li, H. Li, P. Ma, Q. Hu, G. Z. Shi, S. L. Jin, M. R. Huang, Z. Bai, Y. J. Zhou, W. H. Ma, F. F. Duan, S. Y. Jin, Q. R. Gao, X. H. Zhou, Z. G. Hu, M. Wang, M. L. Liu, R. F. Chen, and X. W. Ma. Large Isospin Asymmetry in Si22/O22 Mirror Gamow-Teller Transitions Reveals the Halo Structure of ^{22}Al. *Physical Review Letters*, 125(19):192503, 2020.

[18] M. Langevin, A.C. Mueller, D. Guillemaud-Mueller, M.G. Saint-Laurent, R. Anne, M. Bernas, J. Galin, D. Guerreau, J.C. Jacmart, S.D. Hoath, F. Naulin, F. Pougheon, E. Quiniou, and C. Détraz. Mapping of the proton drip-line up to Z = 20: Observation of the T_Z = -5/2 series ^{23}Si, ^{27}S, ^{31}Ar and ^{35}Ca. *Nuclear Physics A*, 455(1):149–157, 1986.

[19] B. Blank, F. Boué, S. Andriamonje, S. Czajkowski, R. Del Moral, J. P. Dufour, A. Fleury, P. Pourre, M. S. Pravikoff, E. Hanelt, N. A. Orr, and K. H. Schmidt. Spectroscopic studies of the βp and β2p decay of ^{23}Si. *Zeitschrift für Physik A Hadrons and Nuclei*, 357(3):247–254, 1997.

[20] K. Wang, D. Q. Fang, Y. T. Wang, X. X. Xu, L. J. Sun, Z. Bai, M. R. Huang, S. L. Jin, C. Li, H. Li, J. Li, X. F. Li, C. J. Lin, J. B. Ma, P. Ma, W. H. Ma, M. W. Nie, C. Z. Shi, H. W. Wang, J. G. Wang, J. S. Wang, L. Yang, Y. Y. Yang, H. Q. Zhang, Y. J. Zhou, Y. G. Ma, and W. Q. Shen. Spectroscopic study of β-delayed particle emission from proton-rich nucleus ^{23}Si. *International Journal of Modern Physics E*, 27(02):1850014, 2018.

[21] J. A. Caggiano, D. Bazin, W. Benenson, B. Davids, R. Ibbotson, H. Scheit, B. M. Sherrill, M. Steiner, J. Yurkon, A. F. Zeller, B. Blank, M. Chartier, J. Greene, J. A. Nolen, A. H. Wuosmaa, M. Bhattacharya, A. Garcia, and M. Wiescher. Spectroscopy of ^{23}Al and ^{27}P using the (^{7}Li,^{8}He) reaction and the implications for ^{22}Na and ^{26}Al nucleosynthesis in explosive hydrogen burning. *Physical Review C*, 64(2):025802, 2001.

[22] T. Gomi, T. Motobayashi, Y. Ando, N. Aoi, H. Baba, K. Demichi, Z. Elekes, N. Fukuda, Zs. Fülöp, U. Futakami, H. Hasegawa, Y. Higurashi, K. Ieki, N. Imai, M. Ishihara, K. Ishikawa, N. Iwasa, H. Iwasaki, S. Kanno, Y. Kondo, T. Kubo, S. Kubono, M. Kunibu, K. Kurita, Y.U. Matsuyama, S. Michimasa, T. Minemura, M. Miura, H. Murakami, T. Nakamura, M. Notani, S. Ota, A. Saito, H. Sakurai, M. Serata, S. Shimoura, T. Sugimoto, E. Takeshita, S. Takeuchi, Y. Togano, K. Ue, K. Yamada, Y. Yanagisawa, and K. Yoneda. Coulomb Dissociation of ^{23}Al for the stellar ^{22}Mg(p,γ)^{23}Al reaction. *Nuclear Physics A*, 758:761–764, 2005.

[23] J. J. He, S. Kubono, T. Teranishi, M. Notani, H. Baba, S. Nishimura, J. Y. Moon, M. Nishimura, H. Iwasaki, Y. Yanagisawa, N. Hokoiwa, M. Kibe, J. H. Lee, S. Kato, Y. Gono, and C. S. Lee. Investigation of structure in ^{23}Al via resonant proton scattering of ^{22}Mg+p and the ^{22}Mg(p,γ)^{23}Al astrophysical reaction rate. *Physical Review C*, 76(5):055802, 2007.

[24] B. A. Brown, R. R. C. Clement, H. Schatz, A. Volya, and W. A. Richter. Proton drip-line calculations and the rp process. *Physical Review C*, 65(4):045802, 2002.

[25] B. Blank, T. Goigoux, P. Ascher, M. Gerbaux, J. Giovinazzo, S. Grévy, T. Kurtukian Nieto, C. Magron, J. Agramunt, A. Algora, V. Guadilla, A. Montaner-Piza, A. I. Morales, S. E. A.

Orrigo, B. Rubio, D. S. Ahn, P. Doornenbal, N. Fukuda, N. Inabe, G. Kiss, T. Kubo, S. Kubono, S. Nishimura, V. H. Phong, H. Sakurai, Y. Shimizu, P.-A. Söderström, T. Sumikama, H. Suzuki, H. Takeda, J. Wu, Y. Fujita, M. Tanaka, W. Gelletly, P. Aguilera, F. Molina, F. Diel, D. Lubos, G. de Angelis, D. Napoli, C. Borcea, A. Boso, R. B. Cakirli, E. Ganioglu, J. Chiba, D. Nishimura, H. Oikawa, Y. Takei, S. Yagi, K. Wimmer, G. de France, and S. Go. New neutron-deficient isotopes from ^{78}Kr fragmentation. *Physical Review C*, 93(6):061301, 2016.

[26] A. Stolz, T. Baumann, N.H. Frank, T.N. Ginter, G.W. Hitt, E. Kwan, M. Mocko, W. Peters, A. Schiller, C.S. Sumithrarachchi, and M. Thoennessen. First observation of ^{60}Ge and ^{64}Se. *Physics Letters B*, 627(1-4):32–37, 2005.

[27] J.-J. Gaimard and K.-H. Schmidt. A reexamination of the abrasion-ablation model for the description of the nuclear fragmentation reaction. *Nuclear Physics A*, 531(3):709–745, 1991.

[28] K. Sümmerer and B. Blank. Modified empirical parametrization of fragmentation cross sections. *Physical Review C*, 61(3):034607, 2000.

[29] B. Blank, C. Borcea, G. Canchel, C. E. Demonchy, F. de Oliveira Santos, C. Dossat, J. Giovinazzo, S. Grévy, L. Hay, P. Hellmuth, S. Leblanc, I. Matea, J. L. Pedroza, L. Perrot, J. Pibernat, A. Rebii, L. Serani, and J. C. Thomas. Production cross-sections of proton-rich ^{70}Ge fragments and the decay of ^{57}Zn and ^{61}Ge. *The European Physical Journal A*, 31(3):267–272, 2007.

[30] Kamal K Seth, S Iversen, M Kaletka, D Barlow, A Saha, and R Soundranayagam. Mass of proton-rich ^{58}Zn by pion double charge exchange. *Physics Letters B*, 173(4):397–399, 1986.

[31] A Jokinen, M Oinonen, J Äystö, P Baumann, P Dendooven, F Didierjean, V Fedoseyev, A Huck, Y Jading, A Knipper, M Koizumi, U Köster, J Lettry, P O Lipas, W Liu, V Mishin, M Ramdhane, H Ravn, E Roeckl, V Sebastian, and G Walter. Beta decay of the M_T=-1 nucleus ^{58}Zn studied by selective laser ionization. *The European Physical Journal A*, 3(3):271–276, 1998.

[32] M. J. López Jiménez, B. Blank, M. Chartier, S. Czajkowski, P. Dessagne, G. de France, J. Giovinazzo, D. Karamanis, M. Lewitowicz, V. Maslov, C. Miehé, P. H. Regan, M. Stanoiu, and M. Wiescher. Half-life measurements of proton-rich ^{78}Kr fragments. *Physical Review C*, 66(2):025803, 2002.

[33] L. Kucuk, S. E. A. Orrigo, A. Montaner-Pizá, B. Rubio, Y. Fujita, W. Gelletly, B. Blank, Y. Oktem, T. Adachi, A. Algora, P. Ascher, R. B. Cakirli, G. de France, H. Fujita, E. Ganioğlu, J. Giovinazzo, S. Grévy, F. M. Marqués, F. Molina, F. de Oliveira Santos, L. Perrot, R. Raabe, P. C. Srivastava, G. Susoy, A. Tamii, and J. C. Thomas. Half-life determination of T_z = -1 and T_z = - 1/2 proton-rich nuclei and the β decay of ^{58}Zn. *The European Physical Journal A*, 53(6):134, 2017.

[34] Walter H. G. Lewin, Jan Van Paradijs, and Ronald E. Taam. X-ray bursts. *Space Science Reviews*, 62(3-4):223–389, 1993.

[35] G. Lorusso, A. Becerril, A. Amthor, T. Baumann, D. Bazin, J. S. Berryman, B. A. Brown, R. H. Cyburt, H. L. Crawford, A. Estrade, A. Gade, T. Ginter, C. J. Guess, M. Hausmann, G. W. Hitt, P. F. Mantica, M. Matos, R. Meharchand, K. Minamisono, F. Montes, G. Perdikakis, J. Pereira, M. Portillo, H. Schatz, K. Smith, J. Stoker, A. Stolz, and R. G. T. Zegers. β-delayed proton emission in the ^{100}Sn region. *Physical Review C*, 86(1):014313, 2012.

[36] M. Pfützner, M. Karny, L. V. Grigorenko, and K. Riisager. Radioactive decays at limits of nuclear stability. *Reviews of Modern Physics*, 84(2):567–619, 2012.

[37] B. Blank and M.J.G. Borge. Nuclear structure at the proton drip line: Advances with nuclear decay studies. *Progress in Particle and Nuclear Physics*, 60(2):403–483, 2008.

[38] S. Kox, A. Gamp, C. Perrin, J. Arvieux, R. Bertholet, J. F. Bruandet, M. Buenerd, R. Cherkaoui, A. J. Cole, Y. El-Masri, N. Longequeue, J. Menet, F. Merchez, and J. B. Viano. Trends of total reaction cross sections for heavy ion collisions in the intermediate energy range. *Physical Review C*, 35(5):1678–1691, 1987.

[39] K. Sümmerer. Improved empirical parametrization of fragmentation cross sections. *Physical Review C*, 86(1):014601, 2012.

[40] SRIM - The Stopping and Range of Ions in Matter, www.srim.org (01.12.2022).

[41] K. Miernik, W. Dominik, Z. Janas, M. Pfützner, L. Grigorenko, C. R. Bingham, H. Czyrkowski, M. Ćwiok, I. G. Darby, R. Dąbrowski, T. Ginter, R. Grzywacz, M. Karny, A. Korgul, W. Kuśmierz, S. N. Liddick, M. Rajabali, K. Rykaczewski, and A. Stolz. Two-Proton Correlations in the Decay of ^{45}Fe. *Physical Review Letters*, 99(19):192501, 2007.

[42] F. Sauli. GEM: A new concept for electron amplification in gas detectors. *Nuclear Instruments and Methods in Physics Research Section A: Accelerators, Spectrometers, Detectors and Associated Equipment*, 386(2-3):531–534, 1997.

[43] A. A. Lis. Badanie emisji światła w detektorze OTPC. Bachelor thesis, University of Warsaw, Faculty of Physics, 2013.

[44] M. Kuich. Badanie naładowanych kanałów rozpadu ^{8}He za pomocą detektora OTPC. Master thesis, Warsaw University of Technology, Faculty of Physics, 2013.

[45] A. A. Lis, C. Mazzocchi, W. Dominik, Z. Janas, M. Pfützner, M. Pomorski, L. Acosta, S. Baraeva, E. Casarejos, J. Duénas-Díaz, V. Dunin, J. M. Espino, A. Estrade, F. Farinon, A. Fomichev, H. Geissel, A. Gorshkov, G. Kamiński, O. Kiselev, R. Knöbel, S. Krupko, M. Kuich, Yu. A. Litvinov, G. Marquinez-Durán, I. Martel, I. Mukha, C. Nociforo, A. K. Ordúz, S. Pietri, A. Prochazka, A. M. Sánchez-Benítez, H. Simon, B. Sitar, R. Slepnev, M. Stanoiu, P. Strmen, I. Szarka, M. Takechi, Y. Tanaka, H. Weick, and J. S. Winfield. β-delayed three-proton decay of ^{31}Ar. *Physical Review C*, 91(6):064309, 2015.

[46] Magboltz - transport of electrons in gas mixtures, www.magboltz.web.cern.ch/magboltz/ (01.04.2023).

[47] R.E. Tribble, R.H. Burch, and C.A. Gagliardi. MARS: A momentum achromat recoil spectrometer. *Nuclear Instruments and Methods in Physics Research Section A: Accelerators, Spectrometers, Detectors and Associated Equipment*, 285(3):441–446, 1989.

[48] D.J. Morrissey, B.M. Sherrill, M. Steiner, A. Stolz, and I. Wiedenhoever. Commissioning the A1900 projectile fragment separator. *Nuclear Instruments and Methods in Physics Research Section B: Beam Interactions with Materials and Atoms*, 204:90–96, 2003.

[49] PIXIE-16, www.xia.com/products/pixie-16/ (01.12.2022).

[50] LISE ++, www.lise.nscl.msu.edu/lise.html (01.04.2023).

[51] K Miernik. Mean Lifetime Measurements in Low-statistics Experiments. *Acta Physica Polonica B*, 46(3):725, 2015.

[52] K. H. Schmidt. A new test for random events of an exponential distribution. *The European Physical Journal A*, 8(1):141–145, 2000.

[53] M. Shamsuzzoha Basunia and Anagha Chakraborty. Nuclear Data Sheets for A = 23. *Nuclear Data Sheets*, 171:1–252, 2021.

[54] M. Pomorski, K. Miernik, W. Dominik, Z. Janas, M. Pfützner, C. R. Bingham, H. Czyrkowski, M. Ćwiok, I. G. Darby, R. Dąbrowski, T. Ginter, R. Grzywacz, M. Karny, A. Korgul, W. Kuśmierz, S. N. Liddick, M. Rajabali, K. Rykaczewski, and A. Stolz. β-delayed proton emission branches in ^{43}Cr. *Physical Review C*, 83(1):014306, 2011.

[55] Ł. Janiak, N. Sokołowska, A. A. Bezbakh, A. A. Ciemny, H. Czyrkowski, R. Dąbrowski, W. Dominik, A. S. Fomichev, M. S. Golovkov, A. V. Gorshkov, Z. Janas, G. Kamiński, A. G. Knyazev, S. A. Krupko, M. Kuich, C. Mazzocchi, M. Mentel, M. Pfützner, P. Pluciński, M. Pomorski, R. S. Slepniev, and B. Zalewski. β-delayed proton emission from ^{26}P and ^{27}S. *Physical Review C*, 95(3):034315, 2017.

[56] M. Shamsuzzoha Basunia. Nuclear Data Sheets for A = 22. *Nuclear Data Sheets*, 127:69–190, 2015.

[57] E. Gete, L. Buchmann, R. E. Azuma, D. Anthony, N. Bateman, J. C. Chow, J. M. D'Auria, M. Dombsky, U. Giesen, C. Iliadis, K. P. Jackson, J. D. King, D. F. Measday, and A. C. Morton. β-delayed particle decay of ^{9}C and the A=9, T=1/2 nuclear system: Experiment, data, and phenomenological analysis. *Physical Review C*, 61(6):064310, 2000.

[58] J. C. Chow, J. D. King, N. P. T. Bateman, R. N. Boyd, L. Buchmann, J. M. D'Auria, T. Davinson, M. Dombsky, E. Gete, U. Giesen, C. Iliadis, K. P. Jackson, A. C. Morton, J. Powell, and A. Shotter. β-delayed particle decay of ^{17}Ne into p+α+^{12}C through the isobaric analog state in ^{17}F. *Physical Review C*, 66(6):064316, 2002.

[59] M.V. Lund, M.J.G. Borge, J.A. Briz, J. Cederkäll, H.O.U. Fynbo, J.H. Jensen, B. Jonson, K.L. Laursen, T. Nilsson, A. Perea, V. Pesudo, K. Riisager, and O. Tengblad. Systematic trends in beta-delayed particle emitting nuclei: The case of βpα emission from ^{21}Mg. *Physics Letters B*, 750:356–359, 2015.

[60] Jack Bishop, G V Rogachev, S Ahn, M Barbui, S M Cha, E Harris, C Hunt, C H Kim, D Kim, S H Kim, E Koshchiy, Z Luo, C Park, C E Parker, E C Pollacco, B T Roeder, M Roosa, A Saastamoinen, and D P Scriven. First observation of the $\beta 3\alpha$p decay of ^{13}O via β-delayed charged-particle spectroscopy. *Physical Review Letters*, 130:222501, 2023.

[61] W. Satuła, P. Bączyk, J. Dobaczewski, and M. Konieczka. No-core configuration-interaction model for the isospin- and angular-momentum-projected states. *Physical Review C*, 94(2):024306, 2016.

[62] A. A. Ciemny, C. Mazzocchi, W. Dominik, A. Fijałkowska, J. Hooker, C. Hunt, H. Jayatissa, Ł. Janiak, G. Kamiński, E. Koshchiy, M. Pfützner, M. Pomorski, B. Roeder, G. V. Rogachev, A. Saastamoinen, S. Sharma, N. Sokołowska, W. Satuła, and Jagjit Singh. β-delayed charged-particle decay of ^{22,23}Si. *Physical Review C*, 106(1):014317, 2022.

[63] M. Hirsch, A. Staudt, K. Muto, and H.V. Klapdorkleingrothaus. Microscopic Predictions of β+/EC-Decay Half-Lives. *Atomic Data and Nuclear Data Tables*, 53(2):165–193, 1993.

[64] K Grotz, H V Klapdor, and Richard Madey. The Weak Interaction in Nuclear, Particle and Astrophysics. *Physics Today*, 45(3):66–66, 1992.

[65] P. Möller, J.R. Nix, and K.-L. Kratz. Nuclear properties for astrophysical and radioactive-ion-beam applications. *Atomic Data and Nuclear Data Tables*, 66(2):131–343, 1997.

[66] T. Goigoux, P. Ascher, B. Blank, M. Gerbaux, J. Giovinazzo, S. Grévy, T. Kurtukian Nieto, C. Magron, P. Doornenbal, G. G. Kiss, S. Nishimura, P.-A. Söderström, V. H. Phong, J. Wu, D. S. Ahn, N. Fukuda, N. Inabe, T. Kubo, S. Kubono, H. Sakurai, Y. Shimizu, T. Sumikama, H. Suzuki, H. Takeda, J. Agramunt, A. Algora, V. Guadilla, A. Montaner-Piza, A. I. Morales, S. E. A. Orrigo, B. Rubio, Y. Fujita, M. Tanaka, W. Gelletly, P. Aguilera, F. Molina, F. Diel, D. Lubos, G. de Angelis, D. Napoli, C. Borcea, A. Boso, R. B. Cakirli, E. Ganioglu, J. Chiba, D. Nishimura, H. Oikawa, Y. Takei, S. Yagi, K. Wimmer, G. de France, S. Go, and B. A. Brown. Two-Proton Radioactivity of ^{67}Kr. *Physical Review Letters*, 117(16):162501, 2016. T1/2 of 59Ge, no 2p decay.

[67] NNDC Logft, www.nndc.bnl.gov/nudat3/ (01.12.2022).

[68] Meng Wang, G. Audi, F. G. Kondev, W.J. Huang, S. Naimi, and Xing Xu. The AME2016 atomic mass evaluation (II). Tables, graphs and references. *Chinese Physics C*, 41(3):030003, 2017.

[69] Y. Fujita, H. Fujita, T. Adachi, G.P.A. Berg, E. Caurier, H. Fujimura, K. Hara, K. Hatanaka, Z. Janas, J. Kamiya, T. Kawabata, K. Langanke, G. Martınez-Pinedo, T. Noro, E. Roeckl, Y. Shimbara, T. Shinada, S.Y. van der Werf, M. Yoshifuku, M. Yosoi, and R.G.T. Zegers. Gamow-Teller transitions from ^{58}Ni to discrete states of ^{58}Cu. *The European Physical Journal A - Hadrons and Nuclei*, 13(4):411–418, 2002.

[70] K. Hara, T. Adachi, H. Akimune, I. Daito, H. Fujimura, Y. Fujita, M. Fujiwara, K. Fushimi, K. Y. Hara, M. N. Harakeh, K. Ichihara, T. Ishikawa, J. Jänecke, J. Kamiya, T. Kawabata, K. Kawase, K. Nakanishi, Y. Sakemi, Y. Shimbara, Y. Shimizu, M. Uchida, H. P. Yoshida,

M. Yosoi, and R. G. T. Zegers. Microscopic structure of the Gamow-Teller resonance in ^{58}Cu. *Physical Review C*, 68(6):064612, 2003.

[71] D. Nishimura, H. Oikawa, Y. Fujita, B. Rubio, W. Gelletly, J. Agramunt, A. Algora, V. Guadilla, A. Montaner-Piza, A. I. Morales, S. E. A. Orrigo, G. G. Kiss, S. Nishimura, P. A. Söderström, P. Doornenbal, V. H. Phong, J. Wu, B. Blank, T. Goigoux, J. Chiba, Y. Takei, M. Tanaka, S. Yagi, Zs. Dombrádi, D. S. Ahn, H. Baba, N. Fukuda, S. Go, N. Inabe, T. Isobe, T. Kubo, S. Kubono, H. Sakurai, Y. Shimizu, C. Sidong, T. Sumikama, H. Suzuki, H. Takeda, P. Ascher, M. Gerbaux, J. Giovinazzo, S. Grévy, T. Kurtukian Nieto, C. Magron, K. Wimmer, P. Aguilera, F. Molina, F. Diel, J. Eberth, D. Lubos, G. de Angelis, D. Napoli, C. Borcea, A. Boso, R. B. Cakirli, E. Ganioglu, and G. de France. Isospin symmetry in the A = 58 isobars studied by the β-γ spectroscopy of ^{58}Zn. *Meeting Abstracts of the Physical Society of Japan*, 72.2:253–253, 2017.

[72] P. Sarriguren. Stellar weak decay rates in neutron-deficient medium-mass nuclei. *Phys. Rev. C*, 83:025801, Feb 2011.

[73] A. A. Ciemny, W. Dominik, T. Ginter, R. Grzywacz, Z. Janas, M. Kuich, C. Mazzocchi, M. Pfützner, M. Pomorski, D. Bazin, T. Baumann, A. Bezbakh, B. P. Crider, M. Ćwiok, S. Go, G. Kamiński, K. Kolos, A. Korgul, E. Kwan, S. Liddick, K. Miernik, S. V. Paulauskas, J. Pereira, T. Rogiński, K. Rykaczewski, C. Sumithrarachchi, Y. Xiao, H. Schatz, and P. Sarriguren. First identification of ^{58}Zn β-delayed proton emission. *Physical Review C*, 101(3):034305, 2020.

[74] H. Schatz, A. Aprahamian, V. Barnard, L. Bildsten, A. Cumming, M. Ouellette, T. Rauscher, F.-K. Thielemann, and M. Wiescher. End point of the *rp* process on accreting neutron stars. *Phys. Rev. Lett.*, 86:3471–3474, Apr 2001.

[75] R. H. Cyburt, A. M. Amthor, A. Heger, E. Johnson, L. Keek, Z. Meisel, H. Schatz, and K. Smith. Dependence of X-ray burst models on nuclear reaction rates. *The Astrophysical Journal*, 830(2):55, 2016.

[76] H. Schatz, S. Gupta, P. Möller, M. Beard, E. F. Brown, A. T. Deibel, L. R. Gasques, W. R. Hix, L. Keek, R. Lau, A. W. Steiner, and M. Wiescher. Strong neutrino cooling by cycles of electron capture and β-decay in neutron star crusts. *Nature*, 505(7481):62–65, 2014.